

Durham E-Theses

Electrical properties and vapour sensing characteristics of a novel metal-polymer composite

Graham, Adam

How to cite:

Graham, Adam (2008) *Electrical properties and vapour sensing characteristics of a novel metal-polymer composite*, Durham theses, Durham University. Available at Durham E-Theses Online:
<http://etheses.dur.ac.uk/2376/>

Use policy

The full-text may be used and/or reproduced, and given to third parties in any format or medium, without prior permission or charge, for personal research or study, educational, or not-for-profit purposes provided that:

- a full bibliographic reference is made to the original source
- a [link](#) is made to the metadata record in Durham E-Theses
- the full-text is not changed in any way

The full-text must not be sold in any format or medium without the formal permission of the copyright holders.

Please consult the [full Durham E-Theses policy](#) for further details.

Electrical properties and vapour sensing characteristics of a novel metal-polymer composite

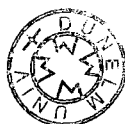
The copyright of this thesis rests with the author or the university to which it was submitted. No quotation from it, or information derived from it may be published without the prior written consent of the author or university, and any information derived from it should be acknowledged.

Adam Graham

03 MAR 2009

Ph.D Thesis

2008



Declaration

I confirm that no part of the material offered has previously been submitted by me for a degree in this or any other University. If material has been generated through joint work, my independent contribution has been clearly indicated. In all other cases, material from the work of others has been acknowledged and quotations and paraphrases suitably indicated.

Signed 

Candidate

The work reported in this thesis was carried out by the candidate. Any work not carried out by the candidate is acknowledged in the main text.

Signed 

Ph.D. supervisor

Statement of copyright

The copyright of this thesis rests with the author. No quotation from it should be published without prior written consent, and information derived from it should be acknowledged.

Abstract

Quantum Tunnelling Composite (QTC) is a metal polymer composite, commercialised and produced using a patented manufacture process. This process ensures that the metal particles within an elastomeric polymer matrix maintain a highly fractal surface morphology where nano-scale point features are retained on the particles and are coated in polymer. This structure provides unique electronic behaviour including very high resistivity, of order $10\text{ M}\Omega$, above the expected percolation threshold and an exponential increase in conductivity under all types of mechanical deformation.

Increase in sample compression leads to a lower electrical resistance through the material. Current-voltage characteristics show a hysteresis effect due to current storage in the QTC material as a current is passed. The hysteresis is shown to be reduced as the applied compression on the material is increased until an Ohmic regime is reached at very high compressions, above 70% linear compression. At these high compressions Joule heating is also proven to occur as a result of the power dissipated in the sample by I-V cycling. The Joule heating is sufficient to influence the physical characteristics of the sample and expand it, creating a current limiting device.

QTC samples loaded with acicular electro-conductive particles in small fractions, less than 10% by weight, showed less sensitivity to applied compression in terms of electrical response. These samples appear to exhibit less white noise characteristics and indicate a combination of field assisted quantum tunnelling and percolation mechanism.

Intrinsically conductive QTC samples were developed. These were made using QTC granules mixed into a polymer solvent solution. Upon depositing onto electrodes the solvent was allowed to evaporate leaving the constituent polymer binding the QTC granules together, compressing them into a conductive state. Samples were exposed to volatile organic compound (VOC) vapours in the concentration range 10 ppm to 100,000 ppm, causing swelling and void filling

in the binding polymer. Combinations of these processes caused an increase in sample resistance, from $\sim 50 \Omega$ to excess of $10 \text{ M}\Omega$.

Sample composition and physical parameters have significant effect upon the response characteristics of the sensors. A system of experiments was undertaken and optimum sample composition was determined.

Response to environmental changes were investigated, namely temperature response and response to varying concentration of exposed solvent. It was found that samples produced using Polyphenylene Oxide (PPO) and Polyvinyl Chloride (PVC) based binding polymer were more resistant to temperature change from $30 \text{ }^\circ\text{C}$ to $80 \text{ }^\circ\text{C}$ due to their molecular structures.

Sensor response to different vapour concentrations was found to exhibit two distinct response regimes. High concentration exposures were found to exhibit a swelling mechanism with a CASE-II diffusion model fitting the data well. Whereas at low concentrations a void-filling based change in sample dielectric constant was attributed to the electronic response to vapour exposure. These predictions were also confirmed using a Quartz Crystal Microbalance (QCM) to measure mass uptake of vapour molecules and polymer density under similar test conditions.

Contents

Abstract	i
Contents	iii
List of Figures and Tables	vi
Chapter 1 - Introduction	
1.1 What is QTC?	1
1.2 Applications	2
1.3 Previous Research	3
1.4 Aims and Objectives	6
Chapter 2 - Models and Theory of Conduction in QTC	
2.1 Introduction	7
2.2 Percolation Theory	8
2.3 Effective Medium Theory	11
2.4 Links-Nodes-Blobs Model	13
2.5 Simple Quantum Tunnelling	18
2.6 Charge Injection	22
2.7 The Image Field Potential and the Schottky Effect	24
2.8 Charge Transport in Insulators	27
2.9 De-Trapping and the Poole-Frenkel Effect	31
2.10 Charge Hopping	32
2.11 Fowler-Nordheim Tunnelling	34

Chapter 3 – Electronic Properties of QTC

3.1	Experimental Introduction	37
3.2	Sample Composition and Preparation	38
3.3	Experimental Setup	40
3.4	Methodology	42
3.5	Results and Analysis	45
3.5.1	High Compression Responses	45
3.5.2	Addition of Acicular Filler	60
3.6	Conclusions to Electronic Properties	67

Chapter 4 – Models and Theory of Vapour Absorption and Diffusion

4.1	Vapour Sensing Technologies	71
4.2	Thermodynamics of Absorption	75
4.3	Fickian Diffusion	77
4.4	Flory-Higgins Parameter	79
4.5	Solubility Parameters	81
4.6	Case-II Diffusion	83

Chapter 5 – QTC Vapour Sensors

5.1	Experimental Setup	87
5.2	Sample manufacture and Preparation	95
5.3	Methodology	96
5.4	Preliminary Experiments	98
5.5	Vapour Sensing Experiments	112
5.6	Results and Analysis	122
5.6.1	Physical Parameters	124
5.6.2	Sample Composition	131
5.6.3	Environmental Response	143
5.7	Conclusions	156

Chapter 6 – QCM Measurements

6.1	QCM Theory	158
6.2	Experimental Setup	163
6.3	Methodology	165
6.4	Results and Analysis	167
6.5	Conclusions	173

Chapter 7 – Concluding Remarks

7.1	Overall Conclusions	174
7.2	Acknowledgements	177
7.3	References	178

Appendix A	186
Appendix B	189
Appendix C	190
Appendix D	193
Appendix E	194
Appendix F	196
Appendix G	198

List of Figures and Tables

<i>Figure 1.1:</i>	<i>SEM image of a nickel particle found in QTC.....</i>	<i>1</i>
<i>Figure 2.1:</i>	<i>Percolation behaviour.....</i>	<i>9</i>
<i>Figure 2.2:</i>	<i>Three stages of filler concentration (a) below, (b) at and (c) above the percolation threshold.....</i>	<i>10</i>
<i>Figure 2.3:</i>	<i>EMT curve compared to Percolation Theory, \square = Percolation Theory and \circ = EMT.....</i>	<i>11</i>
<i>Figure 2.4:</i>	<i>(a) Conductive chains in a percolative composite above threshold, (b) schematic of the links-nodes-blobs model, (c) contacts between aggregates through primary particles.....</i>	<i>14</i>
<i>Figure 2.5:</i>	<i>Tunnelling through a One-Dimensional Potential barrier.....</i>	<i>18</i>
<i>Figure 2.6:</i>	<i>Mirrored charge theorem.....</i>	<i>24</i>
<i>Figure 2.7:</i>	<i>Image Field Potential, applied field potential and resultant potential.....</i>	<i>25</i>
<i>Figure 2.8:</i>	<i>Potential with E-Field and Schottky Effect (dotted line).....</i>	<i>26</i>
<i>Figure 2.9:</i>	<i>Energy band diagrams showing (a) metal-vacuum, (b) metal-insulator and (c) metal-insulator-metal, contacts.....</i>	<i>27</i>
<i>Figure 2.10:</i>	<i>Current-Voltage plot of SCLC behaviour, (a) Ohmic region, (b) Child's law due to shallow trapping, (c) Trap-filled limit, (d) Child's law after trap saturation.....</i>	<i>30</i>
<i>Figure 2.11:</i>	<i>Trap potentials with (a) zero applied E-field and (b) High applied E-Filed causing loss of confinement and electron tunnelling.....</i>	<i>31</i>
<i>Figure 2.12:</i>	<i>Thermally assisted hopping of electrons between trapping potentials.....</i>	<i>32</i>
<i>Figure 2.13:</i>	<i>Potential Barrier with Applied Electrical Field.....</i>	<i>34</i>
<i>Figure 2.14:</i>	<i>Fowler-Nordheim Tunnelling potential.....</i>	<i>35</i>
<i>Table 3.1:</i>	<i>Loading ratios of fillers in samples.....</i>	<i>38</i>
<i>Figure 3.1:</i>	<i>Schematic of experimental setup.....</i>	<i>40</i>
<i>Figure 3.2:</i>	<i>Setup to measure Resistance as a function of Force.....</i>	<i>41</i>

Figure 3.3:	<i>Fixed Jaws to measure Resistance as a function of Compression.....</i>	41
Figure 3.4:	<i>Compression responses of 3 sample types. Compression ranges: $\blacklozenge = 0.5 > 24\%$, $\blacksquare = 22 > 40\%$, $\bullet = 27 > 47\%$.....</i>	43
Figure 3.5:	<i>Response of a Pill Sample to an external uniaxial Force.....</i>	45
Figure 3.6:	<i>Deformation of Samples at higher compressions.....</i>	46
Figure 3.7:	<i>Measured compression as a function of applied force for QTC.....</i>	47
Figure 3.8:	<i>SEM image of standard QTC illustrating heterogeneous Nature.....</i>	48
Figure 3.9:	<i>SEM image of an aggregate of nickel particles.....</i>	49
Figure 3.10:	<i>Pill Sample response to compression as a function of Resistance.....</i>	50
Figure 3.11:	<i>I-V sweep at 20% sample compression, start resistance 440 ohms.....</i>	51
Figure 3.12:	<i>Charge storage and pinching of pathways.....</i>	52
Figure 3.13:	<i>Low field sweep on pill sample.....</i>	54
Figure 3.14:	<i>Initial resistances plotted as a function of the ratio with final resistances.....</i>	55
Figure 3.15:	<i>I-V repeat sweeps, at different start resistances, compressions: $\blacklozenge = 15\%$, $\square = 20\%$, $\circ = 50\%$, $- = 70\%$.</i>	56
Figure 3.16:	<i>All 11 I-V cycles superimposed at 70% compression.....</i>	57
Figure 3.17:	<i>Resistances as a function of cycle number for 70% compression pill sample, $\blacksquare = R$ up, $\bullet = R$ down, $\blacklozenge = R @ V_{max}$.....</i>	58
Figure 3.18:	<i>Model of Joule heating compared to observed data, $\blacklozenge =$ data, $\blacksquare =$ model fit.....</i>	59
Figure 3.19:	<i>I-V characteristics at start resistances 100 Ω for a sample loaded with 4g of acicular filler.....</i>	61
Figure 3.20:	<i>Ratios of initial to final resistances for all samples, with: $\blacklozenge =$ Standard QTC, $\blacksquare =$ 2 g Acicular, $\bullet =$ 4 g Acicular, QTC fit (dotted line) and acicular fit (dashed line).....</i>	62
Figure 3.21:	<i>SEM image showing a cross section image of sample 6.....</i>	64
Figure 3.22:	<i>SEM image of acicular loaded QTC.....</i>	66

<i>Figure 4.1:</i>	<i>Dual slab waveguide interferometer.....</i>	<i>72</i>
<i>Figure 5.1:</i>	<i>Five sample chambers with vapour lines connected.....</i>	<i>87</i>
<i>Figure 5.2:</i>	<i>Sample mounted onto holder with wires connection to Electrodes.....</i>	<i>88</i>
<i>Figure 5.3:</i>	<i>Sample boards and positive displacement dropper.....</i>	<i>89</i>
<i>Figure 5.4:</i>	<i>Schematic of dilution section of vapour kit.....</i>	<i>90</i>
<i>Figure 5.5:</i>	<i>Schematic of venturi flow and pressure directions.....</i>	<i>91</i>
<i>Figure 5.6:</i>	<i>A bubbler chamber and additional liquid trap.....</i>	<i>92</i>
<i>Table 5.1:</i>	<i>Concentration values for various kit setups.....</i>	<i>93</i>
<i>Figure 5.7:</i>	<i>Schematic of electronic solenoid valve flow routes.....</i>	<i>94</i>
<i>Figure 5.8:</i>	<i>Response characteristics of; a) PS #1, b) PS #2, c) PS #3, d) PS #4, e) PC #5, to 113000 ppm of THF for 1 minute exposures with 10 minute purge times.....</i>	<i>101</i>
<i>Figure 5.9:</i>	<i>Response of Nickel powder based vapour sensor to 11300 ppm of THF vapour.....</i>	<i>102</i>
<i>Figure 5.10:</i>	<i>Response of PS #1 based samples exposed to 113000 ppm of THF vapour for droplet sizes of a) 5 μl, b) 10 μl and c) 20 μl.....</i>	<i>104</i>
<i>Figure 5.11:</i>	<i>Response of PS #1 based samples exposed to 113000 ppm of THF vapour for Polymer to Solvent ratios of, a) 1 g : 20 g , b) 2 g : 20 g and c) 3 g : 20 g.....</i>	<i>105</i>
<i>Figure 5.12:</i>	<i>Response of PS #1 based samples exposed to 113000 ppm of THF vapour for Granule to Solution ratios of, a) 2 g : 4 g, b) 1g : 4 g and c) 4 g : 4 g.....</i>	<i>107</i>
<i>Figure 5.13:</i>	<i>PS #1 based samples tested against four solvent types; a) Hexane, b) THF, c) Toluene and d) Acetone, all at 113000 PPM.....</i>	<i>108</i>
<i>Figure 5.14:</i>	<i>Response characteristics of QTC vapour sensors to THF vapour at: a) 56500 ppm, b) 113000 ppm and c) 169500 ppm.....</i>	<i>110</i>
<i>Table 5.2:</i>	<i>Mixing ratios of Polymer to Solvent.....</i>	<i>114</i>
<i>Table 5.3:</i>	<i>Quantities used to create Granule to Solution mixing ratios..</i>	<i>115</i>
<i>Table 5.4:</i>	<i>Polymer types and relative solvent mixing ratios.....</i>	<i>117</i>
<i>Table 5.5:</i>	<i>Mixing ratio of Polyurethane QTC granules in Toluene</i>	

	<i>Solution.....</i>	<i>118</i>
<i>Table 5.6:</i>	<i>Binding polymers and host solvents used for samples measuring temperature dependence.....</i>	<i>120</i>
<i>Figure 5.15:</i>	<i>Response characteristics of a PS #2 based sample exposed to 16950 ppm of THF solvent vapour.....</i>	<i>122</i>
<i>Figure 5.16:</i>	<i>Response time to peak magnitude for copper and tin coated electrodes upon exposure to 16950 ppm of THF vapour, \diamond = Copper, \square = Tin.....</i>	<i>124</i>
<i>Figure 5.17:</i>	<i>Optical microscope images at 182x for (a) a section of copper electrode surface and (b) a section of tin coated electrode Surface.....</i>	<i>125</i>
<i>Figure 5.18:</i>	<i>Typical response of PVC based QTC to 9000 ppm of THF vapour on (Top) ITO and (Bottom) copper and acrylic sample boards.....</i>	<i>126</i>
<i>Figure 5.19:</i>	<i>Start resistance as a function of droplet size.....</i>	<i>128</i>
<i>Figure 5.20:</i>	<i>Response magnitude as a function of droplet size.....</i>	<i>129</i>
<i>Figure 5.21:</i>	<i>Start resistance of QTC vapour samples shown as a function of Polymer to Solvent ratio.....</i>	<i>132</i>
<i>Figure 5.22:</i>	<i>Response time of QTC samples to THF exposure at 16950 ppm as a function of Polymer to Solvent ratio.....</i>	<i>133</i>
<i>Figure 5.23:</i>	<i>Resistance response to applied compression for bulk QTC....</i>	<i>134</i>
<i>Figure 5.24:</i>	<i>Start resistance measured as a function of Granule to Solvent mixing ratio.....</i>	<i>135</i>
<i>Figure 5.25:</i>	<i>Response times of QTC vapour sensors as a function of Granule to Solution loading ration.....</i>	<i>136</i>
<i>Figure 5.26:</i>	<i>Response time as a function of start resistance for all the above experiments.....</i>	<i>137</i>
<i>Table 5.7:</i>	<i>Solubility parameters for the polymer types used here and the THF test vapour.....</i>	<i>138</i>
<i>Figure 5.27:</i>	<i>Response characteristics of PS #2 and PS #4.....</i>	<i>139</i>
<i>Figure 5.28:</i>	<i>Start resistance of different samples used.....</i>	<i>139</i>
<i>Figure 5.29:</i>	<i>Normalised peak response to THF test vapour.....</i>	<i>140</i>
<i>Figure 5.30:</i>	<i>Solubility match values for the polymers used compared to THF vapour.....</i>	<i>140</i>

<i>Figure 5.31: Response time as a function of start resistance for Polyurethane based granules.....</i>	<i>142</i>
<i>Figure 5.32: Temperature response of a PPO based QTC Vapour Sensor, showing QTC resistance (Solid) and measured temperature (dashed).....</i>	<i>144</i>
<i>Figure 5.33: Thermal Coefficients for different polymer based QTC vapour sensors.....</i>	<i>145</i>
<i>Figure 5.34: Molecular structure of a PVC polymer chain.....</i>	<i>146</i>
<i>Figure 5.35: Molecular structure of PPO.....</i>	<i>146</i>
<i>Figure 5.36: Relative response of PS #2 QTC vapours as a function of THF test vapour concentration.....</i>	<i>148</i>
<i>Figure 5.37: Relative response of PVC QTC vapours as a function of THF test vapour concentration.....</i>	<i>149</i>
<i>Figure 5.38: Sensitivity of compressed silicone QTC granules [12].....</i>	<i>149</i>
<i>Figure 5.39: Temporal response of sample resistance upon exposure to “high concentration” THF vapour, $\diamond = 9631$ ppm, $\square = 19102$ ppm, $\circ = 35561$ ppm and $- = 105239$ ppm.....</i>	<i>151</i>
<i>Figure 5.40: Data extracted from Hui [76] demonstrating Case-II Behaviour.....</i>	<i>152</i>
<i>Figure 5.41: Temporal response of sample resistance upon exposure to “high concentration” THF vapour, $\circ = 22$ ppm, $- = 144$ ppm, $\diamond = 688$ ppm, $\square = 4133$ ppm.....</i>	<i>153</i>
<i>Figure 5.42: Differential resistance change as a function of analyte partial pressure for a carbon black filled polyurethane gas sensor [96].....</i>	<i>154</i>
<i>Figure 6.1: The BVD model of a QC resonator circuit.....</i>	<i>160</i>
<i>Figure 6.2: Photographs of a) QCM sensor unit, b) vapour hood and c) a Quartz Crystal used in the QCM200.....</i>	<i>163</i>
<i>Figure 6.3: QCM200 control unit and sensor unit.....</i>	<i>164</i>
<i>Figure 6.4: Mass uptake of PS #2 upon exposure to THF solvent vapour, $\diamond =$ Data, Solid line = model fit.....</i>	<i>167</i>
<i>Figure 6.5: Density values for PS #2 upon exposure to THF solvent vapour at different concentrations.....</i>	<i>168</i>

<i>Figure 6.6: Mass uptake and series resistance of a PS #2 exposed to 19102 ppm of THF vapour.....</i>	<i>169</i>
<i>Figure 6.7: Series resistance of a PS #2 exposed 19102 ppm of THF vapour.....</i>	<i>170</i>
<i>Figure 6.8: Mass uptake of a PS #2 exposed 466 ppm of THF Vapour.....</i>	<i>170</i>
<i>Figure 6.9: Series resistance of a PS #2 exposed 466 ppm of THF vapour.....</i>	<i>171</i>

Chapter 1, Introduction

1.1 What is QTC?

Quantum Tunnelling Composite (QTC) is a relatively new material, produced by Peratech Ltd [1] and developed since 1996. QTC is a metal polymer composite with unique electrical properties and is produced by Peratech using a patented manufacture process [2]. This process ensures that the metal particles, Nickel in QTC, maintain a highly fractal surface profile which is predominantly spiky in nature (figure 1.1) where nano-scale features are retained.



Figure 1.1: SEM image of a 1 micron diameter nickel particle found in QTC

This is in contrast to most other metal polymer composites made from a variety of materials including copper, silver, zinc [3-6] and more commonly carbon black particles [7-9]. These more typical composites generally have smoother surface profiles and conduct through a mechanism described by percolation theory, where charge is transferred between particles in close proximity, standard QTC does not. Due to the spiky nature of the Nickel particles, high electric fields are produced at the tips of the spikes which allow conduction described by the Fowler-Nordheim tunnelling mechanism. Furthermore the particles are fully wetted in the polymer matrix so at high filler concentrations there is no direct contact of the particles and conduction is primarily through field assisted quantum tunnelling across relatively thick barriers. The structure provides unique electronic behaviour including high resistivity above the expected percolation threshold and an exponential increase in conductivity over several orders of magnitude under all types of mechanical deformation.

1.2 Applications

QTC is currently used in a number of different applications in commercial, industrial and scientific areas. The first and probably most widespread use of QTC is as a switch in wearable electronic systems, utilising transition from high to low resistance under applied pressure. It is also employed as a pressure sensor in electrical devices [1]. The exponential response of QTC to deformation allows for very sensitive touch response in the material. Variation of nickel loading and blending of additional materials can be used to tune the QTC into a specific sensitivity range. A further property of the QTC that lends itself to application is that the field assisted tunnelling conduction mechanism is non-contact. That is to say that when the material is distorted physically the nickel particles do not come into contact with each other. This is due to the wetting of the nickel by the host polymer. This means that there is much less mechanical wear in the materials and so they have a much longer working lifetime. Furthermore the spikes on the nickel particles are found to be very strong and even after significant working lifetime in the material their structures remain intact [11].

The Positive Temperature Coefficient of Resistance (PTCR) effect of QTC when high currents are applied to it lends it to being used as a current surge protector or resettable fuse. Further applications of the QTC so far have also included electromagnetic interference shielding and anti static materials.

One of the potential applications for the QTC presented in the later parts of this study is as a chemical vapour sensor. The intrinsically conductive sensors presented later show a significant electrical response in the presence of chemical vapours. These responses are sensitive to both vapour type and concentration depending on their manufacture. The use of a number of different sensors all tuned slightly differently can be employed to give a fingerprint that can characterise a certain combination of gasses. With some careful calibration and a data bank of known vapour responses this setup could be used as an artificial olfactory system, or a so called Electronic Nose [49].

1.3 Previous Research

QTC has been developed for over 10 years and in that time a significant amount of work and research has been carried out on it. Numerous undergraduate projects and a previous PhD [12] are available to date. In addition two scientific papers [13, 14] have been published to date on QTC. The latter, [14] containing results reported upon in this thesis taken from experiments conducted by the author throughout the course of the PhD, this is reproduced as an appendix.

Response of QTC to a range of mechanical deformations was conducted. It was shown that an exponential response is seen from compression, torsion and to a lesser extent extension of QTC samples. Viscoelastic relaxation has been investigated and characterised by measuring the change in resistance when a constant force is applied to QTC over a period of time [12].

Research by Hands has examined the mechanical properties of QTC and their dependence upon filler type and loading ratio. Manufacture of QTC is shown to retain the spiky surface nature of the nickel particles and the importance of these spikes underlined as the primary facilitation of quantum tunnelling. Analysis of the composition of QTC confirms that percolation conduction is not present and that the surfaces of the nickel particles are all completely wetted allowing nickel loadings far above the predicted loading thresholds [12].

Increased loading of nickel into the composite has been shown to increase conductivity, but only over a limited range. A critical loading ratio of 5:1 (nickel to polymer by weight) was found, with any loadings greater than this being detrimental to conduction as particle damage occurs [12].

Upon increasing the nickel loading significantly and changing the manufacture process it was found that granular QTC could be produced. This occurred at 10:1 (wt) nickel/silicone rubber using a much more gentle mixing process. For granules a significantly reduced amount of energy is used, mixing the particles with the polymer until they are only just wetted using also a larger mixing

container. This is in contrast to the production of bulk QTC where the Nickel particles need to be worked much more to produce a continuum of material. This manufacturing process is also patented by Peratech [10]. These granules are clusters of nickel particles bound together by the silicone rubber matrix. Granules were produced in the range between 50 microns and 1 mm diameter, sieved to separate specific ranges of particle size.

Conduction between nickel particles within the samples was shown to be primarily through Fowler-Nordheim tunnelling [45]. This accounts for the ability of the electrons to tunnel the relatively large distances that is not commonly allowed in regular quantum tunnelling. Fowler Nordheim tunnelling can only occur in very high electric fields and it is shown that these can be produced by the nano-scale spikes on the QTC nickel particle surfaces, outlining the importance of this characteristic [12-13].

Current voltage sweeps of QTC samples show a hysteresis, large non linear peaks and return resistances that are generally lower than the start resistances. These phenomena are a result of charge accumulation within the QTC. A theory of charge trapping and pathway pinching which results in a charge accumulating effect within the QTC was developed. Dead end electrical pathways are shown to act as potential barriers to adjacent pathways so restricting charge movement. A memory effect in consecutive cycles on the same sample is observed. This is caused by the charge remaining in some of the trapping sites and dead ends within the sample as the rate at which charge can escape the sample is much slower than the rate it is accumulated. This trapping mechanism worked in parallel to charge trapped also in the surrounding polymer insulator resulting from charge injection. This stored charge can be released by either the application of a large voltage across the sample or if it is vigorously worked mechanically [12-14].

Radio frequency emissions are found to be emitted from QTC. This occurs when an applied voltage across the sample is increased. The amount of trapped charge increases until the local trapping potentials are overcome resulting in a cascade of charge redistributing to neighbouring trapping sites. Resonance decays can

occur between sites causing an oscillating charge and thus radio emissions. Spark discharging may also occur when discharges reach the surface of the sample. [15]

Work on the positive temperature coefficient effects of QTC has been undertaken. It has been found that Joule heating in the sample is significant enough to cause its expansion and so increase resistance. This positive temperature coefficient can be used to create a current limiting device out of the QTC material [16]

Vapour sensors were created by using QTC material produced in a granular form. The granules were then compressed between two porous electrodes into a conductive regime. These were then exposed to saturated organic solvent vapours. Following exposure it was found that the QTC responded quickly with large amplitude to different vapours, indicating potential for application in electronic nose devices. Response sizes and times varied with a close relation to solubility parameters. This indicated that polymer swelling was taking place in the exposures to saturated vapour [12]

Experiments run at a range of concentrations show that the granular based QTC vapour sensors have a response that is proportional to concentration of vapour down to a specific concentration. Exposures lower than this tend to show very small responses that have a degree of concentration independency. Repeat tests show repeatability and clear trends. [12]

1.4 Aims and objectives

This PhD follows from earlier work on QTC in both the electrical conductivity characteristics of QTC and also the vapour sensing capabilities of it. In addition to the summary given on previous research carried out on QTC the author will draw from previous PhD work, 4th year project results and also the scientific papers written upon QTC to date in order to introduce the research reported here.

The first section of the thesis aims to describe the characterisation of QTC electrical responses to compression. Early work characterised the effects of QTC under compression, but only to a factor of about 20% compression. This thesis will continue from here and investigate the properties further, up to compression ratios of 80%. Investigations will be described on the effects of adding additional filler materials to QTC in order to reduce noise and RF electromagnetic radiation emissions.

The second part of the thesis will describe the application of QTC as a vapour sensor. Development of an intrinsically conductive QTC will be described, designed to be more reliable and produce more repeatable results than the previous compressed granule sensors. Full characterisation of the new QTC sensors will be shown in order to judge the potential for them as quantitative chemical vapour sensors.

Chapter 2, Models and Theory of Conduction in QTC

2.1 Introduction

The first section of this research involved the investigation of QTC materials under higher compressions following from previous work conducted by Hands [12]. Investigation of QTC samples loaded with acicular (needle like) filler particles will be undertaken, characterising and explaining the behaviour of these alternative composites.

Firstly a presentation of the underlying theory relevant to these investigations will be given as both references to the reader and to aid analysis of the collected data. Chapter 3 will then describe the experiments conducted followed by their analysis and relation to the known theory.

An underlying feature of the theories presented in this section is their relation to the random heterogeneous nature of the QTC material in general. That is to say the material can be described as a series of domains of different phases, specifically domains consisting of filler particles and a domain of insulating polymer material. Using this approach the material can be treated as a continuum on the microscopic scale, ascribing macroscopic properties to it that are dependant upon the microscopic continuum. A systematic theory of random heterogeneous materials therefore depends on accurate description of this microstructure that includes properties such as; phase volume fractions, surface areas of interfaces, correlation functions of filler networks and shapes, sizes and special distributions of phase domains consisting of various filler types.

Both the percolation theories and the Links Nodes and Blobs model described later can be used to describe more quantitatively the properties of random heterogeneous materials to good effect. For a full review of random heterogeneous materials and various approaches to their analysis the reader is directed to the following reference [17].

2.2 Percolation Theory

Percolation Theory is a concept that was originally conceived in order to describe the situation of some porous material onto which a liquid is poured. The model describes whether the liquid would be able to make its way from hole to hole to reach the bottom. This is then modeled as a three dimensional array of independent points. Each pair of points may then have a connection between them (through which the liquid may travel) which will have a probability p , or there may be no connection (where no liquid may pass) which has a probability $1-p$. For a given p , there is then an overall probability that the liquid will reach the bottom through the material from the top. This idea was developed as an improvement on existing diffusion theory which existed for describing transport of a fluid through a medium. It was first introduced by Broadbent and Hammersley in 1957 [18].

The theory of a fluid flowing through a material can be used in a range of other situations and environments, from modeling disease traveling through a population to molecules penetrating through cell walls in biological systems. A further application of the theory is to that of the conductivity of an electrical current through a metal-polymer composite. As analogy to the introductory example, the polymer is the host material, the metal particles within it are the porous holes and an electrical current is the liquid that needs to pass through it. The conduction of electrical current through the material is a factor of the number of percolation pathways through the composite. Percolation theory has its advantages over diffusion models in this case as it assumes that metal filler particles are diffused randomly throughout the host material, as opposed to being uniformly distributed on a periodic lattice. Metal-polymer composites tend to show a distinct insulator to conductor transition as the concentration of metal filler particles is increased. This phenomenon requires the metal particles to have arranged into random clusters which eventually link into an overall network. This is clearly not possible with an evenly dispersed periodic lattice.

The conductivity σ of a sample can therefore be modeled using the percolation theory as a function of the volume fraction of metal filler particles p . This is described simply by the following equation.

$$\sigma \propto (p - p_c)^t \quad \text{Eqn 2.1}$$

Where p_c is the percolation threshold volume fraction, which is the volume fraction at which the first conducting pathway is created. The value t is a variable that is specific to the type of percolation model used and is between 1 and 6.27 for three-dimensional systems [29]. Figure 2.1 shows conductivity of an example metal polymer composite where percolation is the conduction mechanism, exhibiting a p_c value of approximately 0.09 filler by volume. The author refers the reader to work previously published in this area by Young [29].

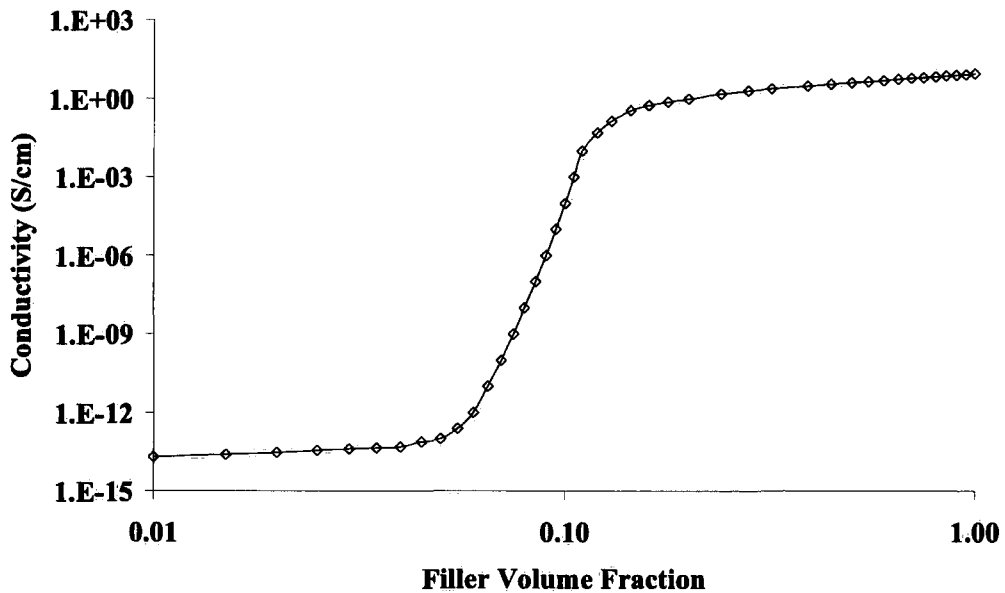


Figure 2.1: Percolation behaviour, $p_c \sim 0.09$.

The three main sections of the graph can be represented in a diagram of the clustering of particles at various concentrations, figure 2.2.

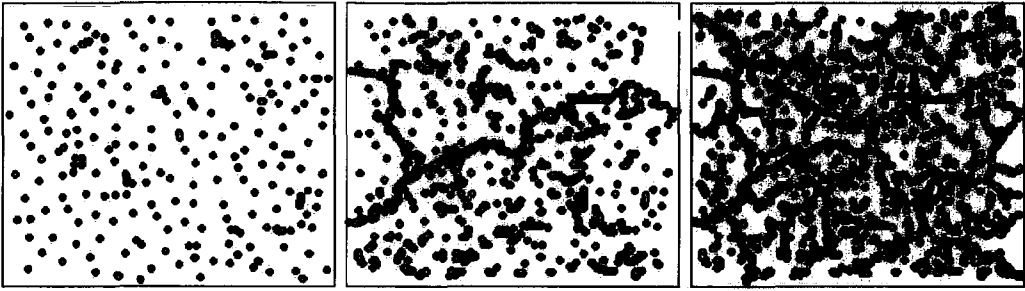


Figure 2.2: Three stages of filler concentration (a) below, (b) at and (c) above the percolation threshold.

Percolation theory can be treated as a statistical process and so has been modelled a number of times using Monte-Carlo computer simulations [19]. The main downfall of these has been the poor correlation between computer generated theoretical values for the variable t and those seen in experiment, the computer values returning between 1 and 2 compared to equivalent experimental data of 2 to 3 [20-22]. This mismatch is attributed to the fact that percolation theory does not account for certain physical variables such as particle size and shape and instead assumes all particles to be spherical and homogeneous.

Further improved models have been developed and published to which the reader is directed a range of works [20-25]. For systems on or near to the percolation threshold experimental data do not match that predicted by the theory [25]. This is a result of there being a very sharp transition at the percolation threshold where $p \sim p_c$, where even slight deviations in filler volume fraction can have relatively large effects upon conductivity. In order to describe systems in this region an improved theory is required which effectively removes the sharp transition region, this is described later. In order to accurately apply percolation theory it is necessary to have a system where $p > p_c$ and the metal filler particles are smooth spherical particles without too much aggregation.

2.3 Effective Medium Theory

Effective Medium Theory (EMT) was developed in order to describe systems that are close to the percolation threshold that cannot be successfully described by standard percolation theory as mentioned above [25].

The EMT starts by taking the basic percolation theory setup. This is to say that each metal particle in the composite is defined as a single site on a three dimensional array. There is then an associated resistance between each pair of nearest neighbour particles. Thus the array represents a network of randomly positioned particles with a random distribution of resistances between them all. EMT then takes this array and replaces all the resistances with an average value. The original randomly distributed array is replaced by a single homogeneous effective medium. The resulting new array is an ordered symmetric lattice that has the same overall macroscopic characteristics of the percolation model.

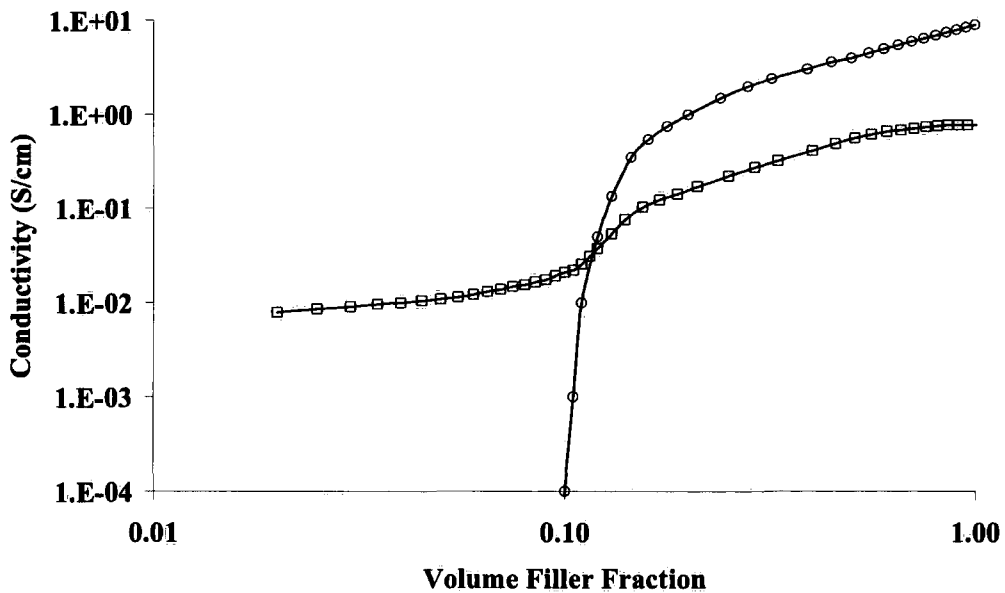


Figure 2.3: EMT curve compared to Percolation Theory, □ = Percolation Theory and ○ = EMT

As a result of this regular array the material properties are smoothed over the whole array and there is no longer a sharp percolation threshold restricting the model at the threshold concentration of filler particles.

From this EMT and the percolation theory previously discussed a General Effective Medium (GEM) equation was developed by McLachlan [26].

$$\frac{f(\Sigma_l - \Sigma_m)}{\Sigma_l + [f_c/(1-f_c)]\Sigma_m} + \frac{(1-f)(\Sigma_h - \Sigma_m)}{\Sigma_h + [f_c/(1-f_c)]\Sigma_m} = 0 \quad \text{Eqn 2.2}$$

$$\Sigma_l = \sigma_l^{1/t} \quad \Sigma_h = \sigma_h^{1/t} \quad \Sigma_m = \sigma_m^{1/t}$$

Where f is the fraction of conductive filler and f_c is the critical fraction at which conduction occurs. The subscripts l and h denote the low and high conductivity components respectively, whilst m represents the effective medium, and t is an exponent. This can be reduced to equation 2.1 when in an infinite conductivity ratio (i.e. $\sigma_l = 0$ and $\sigma_h = \text{finite}$), and considering $p = (1-f)$ and is shown in Appendix F.

For a full discussion on the development and applications of EMT and GEM the author refers to the following work [27-29].

GEM is the most used theory of those discussed in practice as it is easily altered to adapt to slight changes in physical parameters, such as filler particle type shape and surface characteristics. It combines the strengths of the other models into one easily applicable model.

2.4 Links, Nodes and Blobs Model

The Links-Nodes-Blobs model (LNB) was first derived by Lin and Lee in order to explain more fully the Payne effect seen in composite rubber materials [33]. Payne and Medalia [30] had previously found that the mechanical properties of a filler loaded rubber composite did not match those of neat rubber. Furthermore it was shown by Ulmar [31] that as strain on a rubber filled composite exceeded 0.1%; the mechanical properties begin to show evidence of non-linear viscoelasticity. These properties were attributed to the breakdown of a secondary network within the composite made up of the filler particles. Beyond the limit of this breakdown, the mechanical properties of the composite were found to be almost strain independent. Detailed discussion of these experiments and the modelling of the mechanical properties of filled rubbers are given in [30-33]. Lin and Lee progressed from these ideas and theories to produce a model based on a percolative system in order to more fully describe the properties of rubber-filler composites. This model was the LNB model.

The model, as its name suggests, consists of three main factors. The blobs that are aggregates of filler particles, the Links that are chains of primary particles connecting blobs in a network and nodes that are junctions of crossing diverging or splitting links, figure 2.4(b).

The blobs consist of aggregates made up of primary filler particles. A primary particle is defined as the smallest constituent filler particle. Thus in QTC a primary particle would be an individual nickel particle. It should be noted for completeness that a single nickel particle is its self a polycrystalline structure, created in a rapid nucleated growth process at high temperature. However this structure is very strong and in the environment of the QTC material the nickel particles do not break down into individual crystals. For the remainder of this work whole nickel particles will be considered the most fundamental phase of the filler material.

The size of a blob can range from many thousands of aggregate primary particles down to just one single primary particle. Under compression of the

composite, the polymer matrix can deform, along with the filler network. However, the blobs themselves are assumed to be completely rigid and do not deform under compression.

In the percolative LNB model the links between the blobs consist of a continuous chain of single primary particles, creating a network of interconnected blobs. The smallest link length corresponds to the direct connection of two blobs, figure 2.4(c).

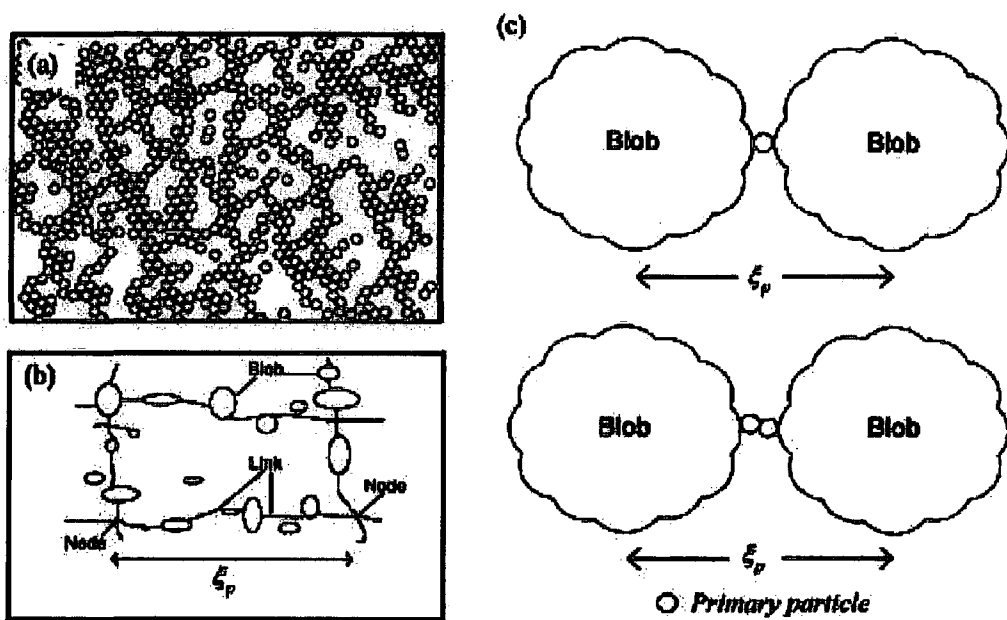


Figure 2.4: (a) Conductive chains in a percolative composite above threshold, (b) schematic of the links-nodes-blobs model, (c) contacts between aggregates through primary particles, [32]

The connections between links are described as nodes. A LNB chain can then be defined as the chain of links and blobs between two adjacent nodes. An average chain length for a composite or part of a composite material can be found and is denoted as ξ_p , this is illustrated in figure 2.4(b).

Now if the sampling scale, or resolution, of the model is less than ξ_p then it is possible to know if there is a continuous chain between every pairing of nodes. If the scaling or resolution is greater than ξ_p then there is a continuum in the

LNB network. The value ξ_p therefore relates to a critical length scale in the percolative system.

A full discussion relating the mechanical properties of a composite material to the LNB model is given in [35]. Specifically it is shown that the strain and failure strength of a material can be modelled accurately through the interaction of filler particles rather than the characteristics of the rubber matrix.

However, in this thesis it is the effects of filler particles on the electronic properties of the composite that are of interest rather than the mechanical effects. A further publication by Lin and Chen [32] developed the LNB model to describe electrical conduction through a filler-rubber composite. The system can be described in a similar way to the LNB model given above to describe the mechanical properties. A further requirement is that the primary filler particles are now required to be conductive and the polymer matrix electrically insulating. The blobs are still described as aggregates of primary filler particles with links single chains of primary particles between them. However instead of being described in terms of their mechanical properties, the links are described in terms of their electrical resistivity.

The overall conductivity of a composite is dependent upon the loading fraction and conductivity of the filler particles that it is partially made up of. It can be assumed that within the blobs that conduction from one side to the opposite side is through a number of parallel pathways giving a low resistivity across the blobs. In contrast the links are made up of a chain of single primary particles and is a number of series linked pathways, leading to a much greater resistivity. The resistivity of the composite on the whole is therefore determined by the number of complete links throughout the material. As the loading fraction of filler ϕ is increased and exceeds a certain critical volume fraction ϕ_c , the filler network become continuous and the electrical state of the material changes from insulator to conductor. As discussed earlier there is a critical chain length ξ_p , which can now be expressed in terms of the critical volume fraction, equation 2.3.

$$\xi_p = \beta(\varphi - \varphi_c)^{-\nu} \quad \text{Eqn. 2.3}$$

Where β is a proportional constant and ν is the fractional dimension. This is essentially the equation to describe a percolative system as described earlier and given in equation 2.2.

Using this relation the LNB model can be used to calculate a number of different parameters. The resistance of a link made of n single bonds between $n+1$ primary particles can be described as;

$$R_\xi(n) = R_1(n+1) \quad \text{Eqn 2.4}$$

Where R_1 is the contact resistance of a single connected bond described by equation 2.5;

$$R_1 = \rho_1 \left(\frac{t}{A_c} \right) \quad \text{Eqn 2.5}$$

ρ_1 is the resistivity across the contact region, t the shortest distance between two contact points and A_c the average contact area. The resistivity $\rho(n)$ of a repeated unit cell can be written as;

$$\rho(n) = \frac{R_\xi(n) \cdot (\xi_p \cdot a)^2}{(\xi \cdot a)} \quad \text{Eqn 2.6}$$

The variable a is the average diameter of a primary filler particle, making the assumption in the model that the particles are all spheres.

The macroscopic resistivity of a composite can therefore be calculated by integration of equation 2.6 over all unit cells across a sample.

In applying this model to QTC specifically modifications are required to the modelling of the conduction mechanism describing the links in the system.

Rather than a conduction system of direct contacts from primary particle to primary particle within each link, charge is instead transferred between blobs via a field assisted quantum tunnelling mechanism. The length of links is now determined by potential barrier thickness and electric field effects caused by the surface morphology of the nickel particles. Detailed discussion of these conduction mechanisms and other related phenomenon are presented in the following sections.

2.5 Simple Elastic Quantum Tunnelling

In this section a review of the quantum tunnelling mechanisms present in QTC will be carried out, building on these with theories of thermionic emission and various electric field effects. The aim will be to provide models of the transport mechanisms of electrons between nickel particles through the composite.

Considering a particle of mass m and energy E_x which is incident on a one-dimensional rectangular potential barrier of height $V_0 > E_x$. The particle will be incident on the barrier from the left, as depicted in figure 2.5. Relating this to the physical system being modelled, regions I and III would represent two adjacent Nickel particles in the composite and Region II would be the insulating dielectric polymer matrix.

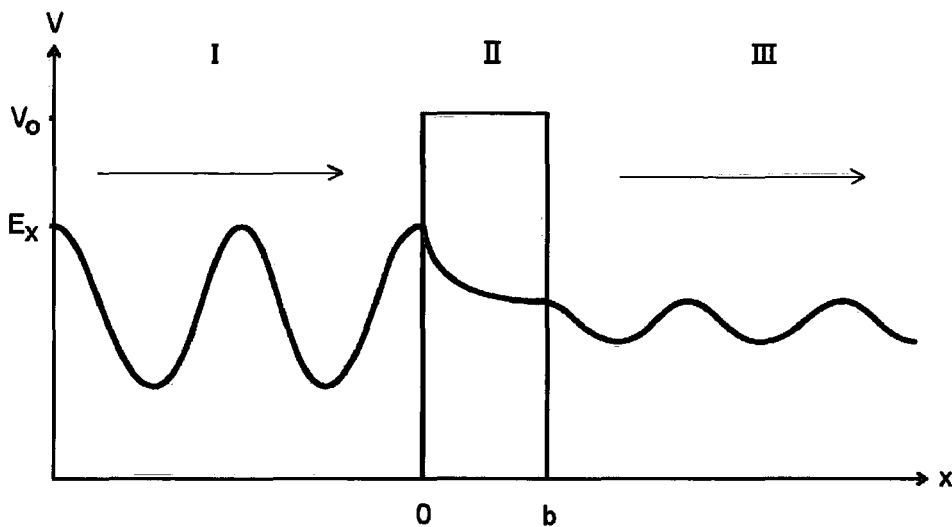


Figure 2.5: Tunnelling through a One-Dimensional Potential barrier

Classically the particle would be certain to be reflected off the potential barrier as it has insufficient energy to carry it over. However quantum mechanically we can model the particle as a wave giving it a wave function Ψ , and say that there is now a finite probability that the particle may be transmitted through the barrier rather than just reflected.

Therefore by considering the wavefunction in all three regions an expression for the transmission coefficient, T , can be obtained. This is a measure of the probability that the particle will be transmitted through the barrier rather than being reflected or carried over it.

The time independent Schrödinger equation will be used to describe the energy characteristics of the wavefunction.

$$-\frac{\hbar^2}{2m} \frac{d^2\Psi(x)}{dx^2} + V(x)\Psi(x) = E\Psi(x) \quad \text{Eqn 2.7}$$

Looking at the three regions indicated in figure 2.5 and at the piecewise solutions to Eqn 2.7 for each region. The two parts to each equation represent the reflected and transmitted parts of the incident waves. Such that the positive exponentials are incident waves and negative ones those that have been reflected, thus travelling in the opposite direction.

$$\text{Region I:} \quad \Psi_I(x) = Ae^{ikx} + Be^{-ikx} \quad \text{Eqn 2.8}$$

$$\text{Region II:} \quad \Psi_{II}(x) = Ce^{\mu x} + De^{-\mu x} \quad \text{Eqn 2.9}$$

$$\text{Region III:} \quad \Psi_{III}(x) = Fe^{ikx} + Ge^{-ikx} \quad \text{Eqn 2.10}$$

$$\text{Where } k = \frac{\sqrt{2mE_x}}{\hbar}, \text{ and } \mu = \frac{\sqrt{2m(V_0 - E_x)}}{\hbar}.$$

Because the barrier is of finite width then the solution to region II, within the barrier, contains exponential terms that both increase and decrease with increasing distance through the barrier. This occurs because waves inside the barrier travelling through it can then be either reflected off or transmitted into the medium on the other side. If the barrier was of infinite depth then there would be no second interface to the barrier for waves to reflect off and so only

waves travelling in one direction would be observed thus no increasing term in the solution and $C = 0$.

Furthermore, since region III will only consist of transmitted particles only then the solution to the wave equation for this region can be limited to that of just the positive exponentials and setting $G = 0$.

From this set of equations quantum tunnelling through a potential barrier can be characterised by the two following parameters, the transmission coefficient T and the reflection coefficient R .

T gives the probability that an electron incident on the barrier will be transmitted through it and so is described by Eqn 2.11.

$$T = \frac{\text{probability flux of transmitted wave in region III}}{\text{probability flux of incident wave in region I}} = \frac{|F|^2}{|A|^2} \quad \text{Eqn 2.11}$$

R in a similar manner gives the probability that an electron incident on the barrier will be reflected back off it and is described by Eqn 2.12.

$$R = \frac{|\text{probability flux of reflected wave in region I}|}{\text{probability flux of incident wave in region I}} = \frac{|B|^2}{|A|^2} \quad \text{Eqn 2.12}$$

As the primary interest is in the current created by electrons that tunnel through the barrier, the transmission coefficient will be examined in more detail.

The transmission coefficient can be determined by imposing wavefunction matching conditions on the solutions given in Eqn 2.8 – 2.10, at the boundaries $x = 0$ and $x = b$.

$$\Psi_I(0) = \Psi_{II}(0) \rightarrow A + B = C + D \quad \text{Eqn 2.13}$$

$$\left. \frac{d\Psi_I}{dx} \right|_{x=0} = \left. \frac{d\Psi_{II}}{dx} \right|_{x=0} \rightarrow ikA - ikB = \mu C - \mu D \quad \text{Eqn 2.14}$$

$$\Psi_{II}(b) = \Psi_{III}(b) \rightarrow C \exp(\mu b) + D \exp(-\mu b) = F \exp(ikb) \quad \text{Eqn 2.15}$$

$$\left. \frac{d\Psi_{II}}{dx} \right|_{x=b} = \left. \frac{d\Psi_{III}}{dx} \right|_{x=b} \rightarrow \mu C \exp(\mu b) - \mu D \exp(-\mu b) = ikF \exp(ikb) \quad \text{Eqn 2.16}$$

Using these matching conditions it is then possible to solve the equations and produce an expression for the transmission coefficient τ . In order to simplify the maths a little only the case of tall wide barriers will be considered, i.e. $\mu b \gg 1$. A full justification of this and mathematical proof of Equation 2.17 is given as Appendix A.

$$\tau = \frac{16\mu^2 k^2 \exp(-2\mu b)}{(k^2 + \mu^2)^2} \quad \text{Eqn 2.17}$$

$$\tau = 16 \left(\frac{E_x}{V_0} \right) \left(1 - \frac{E_x}{V_0} \right) \exp(-2\mu b)$$

From this the reflection coefficient σ can also be obtained, and is related to the transmission coefficient simply by, $\sigma + \tau = 1$

It can be seen that in the limit $\mu b \gg 1$, that τ varies exponentially with μ and increases with increasing energy.

The system can also be described in terms of current density J , which is more useful for comparison with other conduction methods discussed later.

$$J = A_0 \exp(-2\mu b) \quad \text{Eqn 2.18}$$

Where $A_0 = 2emk^2/4\pi^2\hbar^3$, \hbar is the reduced Planck constant, k is the Boltzmann constant and e and m are charge and mass of an electron.

2.6 Charge Injection

The potential barriers in the modelling discussed so far have all been assumed to be fully insulating. However in reality no material is wholly insulating, specifically the polymer matrix used to create QTC is not. Considerable work has been carried out in the area of conduction mechanisms in polymers [37]. In brief provided that there is sufficient surface contact then charge carriers can be injected into a polymer and electrical currents can therefore flow in the polymer. These conduction mechanisms can have an effect on the potential barriers discussed so far in the above tunnelling mechanisms provided that charge injection is present. The most prominent examples of charge injection will now be discussed and their effects on potentials examined.

In order for charge carriers to be injected into a polymer, or other solid, they first need to be emitted from a conductor which is in contact with its surface. For electrons to be emitted from a metal surface they first need to gain a certain amount of energy. Historically this is known as the work function energy and is denoted by ϕ . In the absence of an electrical field the work function energy is generally expressed as the energy required to release an electron from the Fermi level into vacuum. However with the application of an electric field there is a subtle difference in that the work function energy is the energy required for an electron to thermally overcome the potential barrier containing it. This is because the effects of the electric field may distort a potential barrier and allow it to escape without reaching the vacuum level.

V_0 is the actual measured potential height of the barrier and is used to determine tunnelling probabilities, with the associated work function energy of the system describing the minimum energy an electron would need to overcome the barrier thermally.

In a quantum mechanical model a metal at absolute zero will have a range of discrete energy states, each of which will be filled by electrons up to the Fermi level E_f . The work function energy is then the energy required for overcoming

the remaining potential barrier. Thus for an electron to fully escape the metal it must have energy $(E_f + \phi)$. Furthermore this energy needs to be kinetic. Using the free-electron model, where potential energy is neglected, due to electrons not interacting, the electron energies are all in fact kinetic. Electrons can receive energy thermally as the temperature of the metal is raised above absolute zero, and so electrons can overcome the potential barrier and escape, this is known as Thermionic Emission. The emission current density J can then be calculated by energy and density of state considerations, Appendix C and is given by Eqn 2.19.

$$J = A_0(1 - \sigma)(k_B T)^2 \exp\left(\frac{-\phi}{k_B T}\right) \quad \text{Eqn 2.19}$$

Where T is the temperature of the metal, σ is the reflection coefficient from the metal polymer interface and k_B is the Boltzmann constant. This shows that most significant factor in thermionic emission is the temperature of the metal and the actual work function of the metal.

2.7 The Image Field Potential and the Schottky Effect

However there is more to consider when looking at electrons leaving a charged metal surface. The laws of electrostatics state that the forces on a charge in front of an infinitely conducting sheet can be modelled perfectly by replacing the sheet with a mirror charge, i.e. an opposite charge equal distance away from the sheet on the other side. In this case the charge will be that of an electron, e and the system can be visualised simply as shown in figure 2.6.

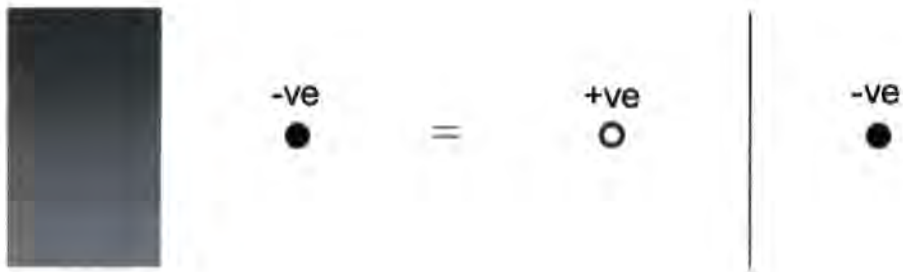


Figure 2.6: Mirrored charge theorem.

There is an associated force that can be calculated between the two mirrored charges which is given simply by equation 2.20. The force is positive by definition as the charges are opposite and are therefore attracted to each other.

$$F = \frac{e^2}{4\pi\epsilon} \frac{1}{(2x)^2} \quad \text{Eqn 2.20}$$

Where x is the distance of the electron from the dividing sheet, e is the charge on an electron and ϵ is the relative permittivity. The potential of the electron can be calculated by simply integrating up Eqn 2.20 from point x to infinity, as given in Eqn 2.21. Assuming that $V(\infty) = 0$, this creates a negative potential due to the location of the zero point.

$$V(x) = \int_x^{\infty} F(x) dx = -\frac{e^2}{16\pi\epsilon x} \quad \text{Eqn 2.21}$$

This represents a potential on the electron as it tries to leave the surface of a metal into a polymer. In order for the electron to fully escape the metal it must escape this image force potential.

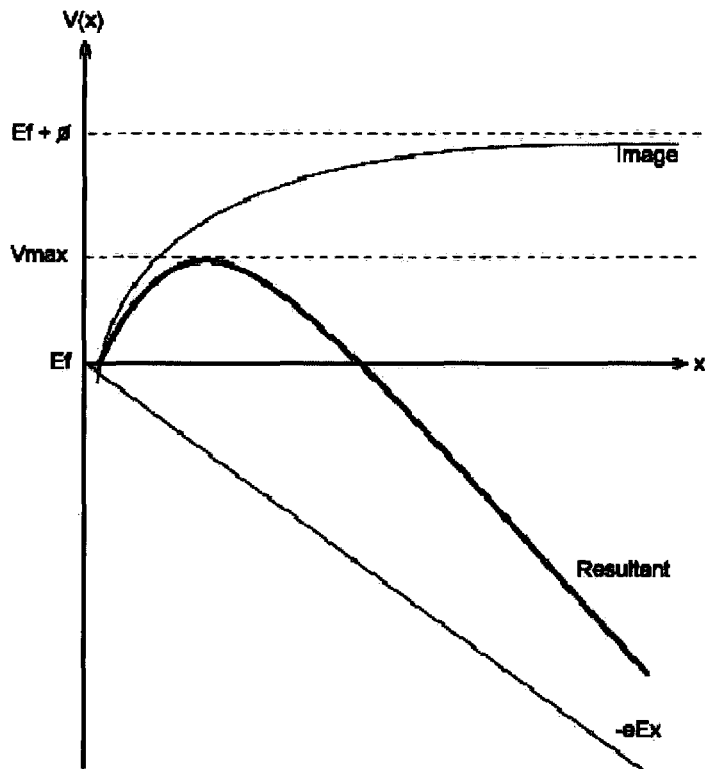


Figure 2.7: Image Field, applied field potential and resultant potential

Now further modifications must be made if an electric field is also present, as was shown previously an electric field E can have significant effects on the potential barrier.

$$V(x) = -eEx \quad \text{Eqn 2.22}$$

The overall potential barrier as a result of image field and electric field can then be calculated by simply adding the two.

$$V(x) = -\frac{e^2}{16\pi\epsilon_0 x} - eEx \quad \text{Eqn 2.23}$$

A maximum permitted potential height can then be found by differentiating Eqn 2.23 and setting it equal to zero, see Appendix D and also [36].

$$V_{MAX} = -e\left(\frac{eE}{4\pi\epsilon_0}\right)^{1/2} \quad \text{Eqn 2.24}$$

The effective work function energy reduction by this amount, V_{MAX} , is known as the Schottky effect. The overall thermionic emission inclusive of the Schottky effect can be now given in terms of the current density J .

$$J = A_0(1 - \sigma)(k_B T)^2 \exp\left(\frac{-\phi - V_{MAX}}{kT}\right) \quad \text{Eqn 2.25}$$

For conduction pathways in QTC, the potential barrier is the polymer matrix separating two nickel aggregates. An image field will therefore be in effect at the interface with each aggregate and the polymer, reducing the barrier at both sides. The resultant barrier shape therefore becomes parabolic in shape as shown in figure 2.8.

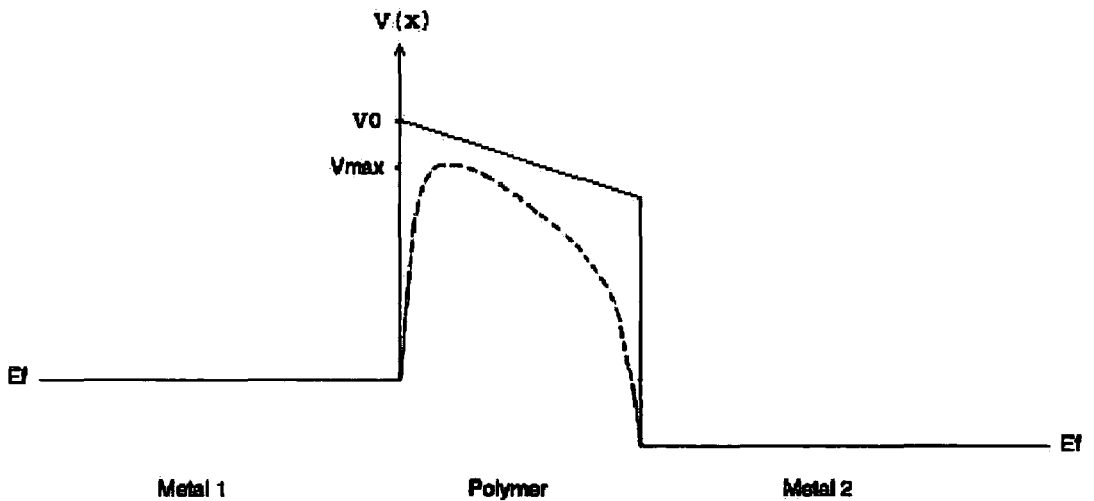


Figure 2.8: Potential barrier with E-Field and Schottky Effect (dotted line)

2.8 Charge Transport in Insulators

Having explored some of the mechanisms of charge injection into insulators it is prudent to now follow with a discussion of the charge transport mechanisms that occur within insulators. The general theory of charge transport in insulators can be approached by first considering the insulator in terms of band theory [38] and discussion of charge injection in these terms.

The energy band theory for charge injection of electrons into an insulator can be simplified and described in terms of energy band diagrams, figure 2.9.

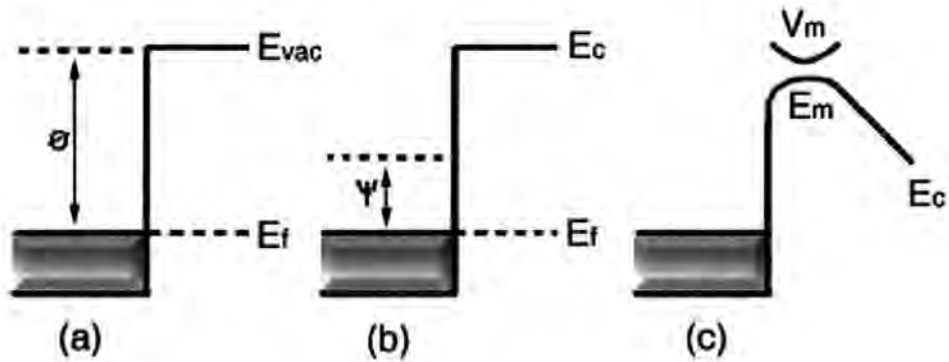


Figure 2.9: Energy band diagrams showing (a) metal-vacuum, (b) metal-insulator and (c) metal-insulator-metal, contacts

Figure 2.9 (a) shows a metal-vacuum contact and (b) a metal-insulator contact, both in thermal equilibrium (no applied voltage). Figure 2.9 (c) represents the band diagram when an applied voltage V_m is applied near to the metal-insulator surface depicted in (b). E_f represents the Fermi level, E_{vac} the lowest vacuum level and E_c the lowest conduction band level of the insulator, with E_m the energy maximum of the insulator conduction band. The first two diagrams are very similar. Electrons will escape the metal into the conduction band of the insulator just as in the case of electrons leaving a heated cathode into vacuum. The electrons available for emission are those thermally excited to energy sufficiently large to overcome the energetic barrier at the emission surface. It was noted by Mott and Gurney [39] that the interface dipole energy barrier ψ at

the metal-insulator contact can be substantially smaller than the corresponding work function barrier ϕ for the metal-vacuum contact. This means that at room temperature and sometimes below, there may be sufficient electrons available with sufficient energy at the contact area to support a space-charge-limited (SCL) electron flow into the insulator. This is in essence the same principal as the image force potential discussed earlier, but specifically in a dielectric. This is further highlighted through comparison of figure 2.9 with figure 2.7 to show the energy potentials involved.

Provided an appropriate charge injection process has occurred then an appreciable electric current can be made to pass through a conventional insulator. Charge injected into a material in this situation is referred to as space-charge. The flow of space-charge through the conduction band of an insulator is limited by frequent collisions with the thermal vibrations of the insulator (phonons) and with the chemical impurities and structural imperfections in the insulator. Electrons may move between such sites by mechanisms including hopping, thermal activation and the Poole-Frenkel effect. A simplified theory of SCL currents was developed in 1955 by Lambert and Rose [37] working on the assumptions developed by Mott and Gurney [39]

In non-perfect crystal structures, defects exist within the lattice matrix. These defects can be in the form of chemical impurities or crystal deformations such as dislocations, Schottky defects and Frenkel pairs. These defects lead to the formation of charge carrier traps within the crystal structure.

Chemical impurities within the host lattice will have differing energy levels, ionising energies and electron affinity compared to neighbouring atoms. If the impurity atom has a greater electron affinity to that of the nearby atoms, then the atom will act as an electron trap. Conversely if the electron affinity is lower then a trap for holes is created. The depth of the traps created is dependent upon the difference in electron affinity between the impurity atom and the surrounding lattice atoms.

Physical deformations in the crystal lattice have the effect of modifying the energy levels surrounding the defect. This occurs due to the regular bonding between adjacent lattice points becoming disturbed. This creates vacant orbitals that lie within the forbidden energy gap between conduction and valence bands of the insulator. Electrons and holes are then able to fall into these vacant orbitals and become trapped.

When an electrical current is passed through an insulator with such trapping sites Ohmic behaviour is seen. However after a certain current is reached, electrons begin to fall into trapping sites and no longer contribute to the conduction. If a constant voltage is maintained across a sample then an increase in the generated current is seen. This is a result of there being more trapping sites filled by electrons that no longer hinder the current flow. Space-Charge is becoming trapped within the sample and the material is said to display a Space-Charge-Limited-Current (SCLC), Child's Law is obeyed. Child's Law states that the SCLC in a plane-parallel diode varies directly as the three halves power of the anode voltage V and inversely as the square of the distance d separating the cathode and the anode, equation 2.26.

$$I = JS = \alpha \frac{SV^{3/2}}{d^2} \quad \text{Eqn 2.26}$$

I is the anode current, J the current density, S the area and α is a numerical constant of proportionality. In practice the Ohmic and SCLC regions often blur into one curve and are indistinguishable.

The observed current continues to rise until the material becomes saturated and all the traps are filled, any further voltage increase would cause more carriers to be introduced that cannot be trapped. This results in a sharp increase in the observed current-voltage characteristics. The material is now said to have exceeded the trap-filled limit. Traps may be seen to exist at many different energy levels which cause the current to pass through a number of distinct sudden rises. Beyond the trap-filled limit the current is then limited by the new intrinsic resistivity of the material and Child's law is again obeyed. This final

region is also seen to blur with the previous gradient when examined in practice. Figure 2.10 displays the above trends and gradients as a current-voltage plot.

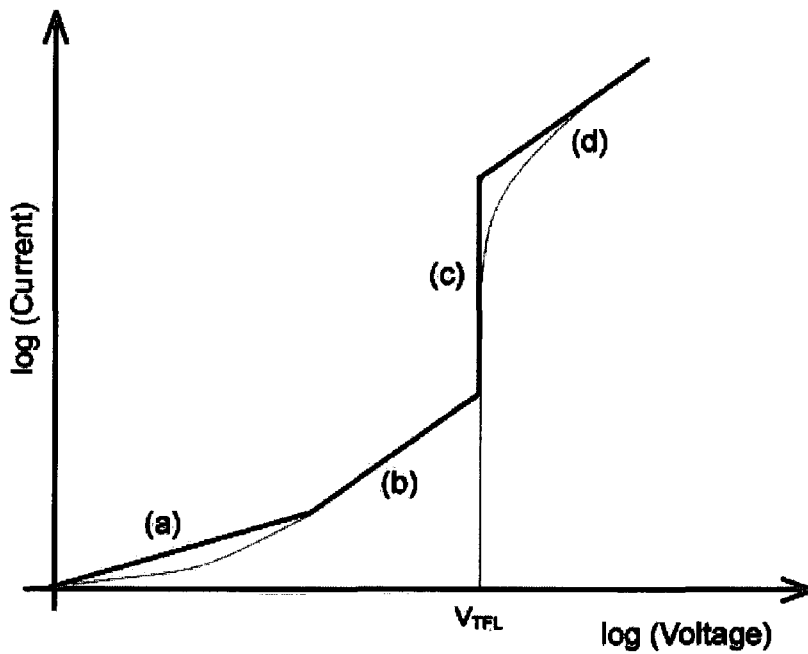


Figure 2.10: Current-Voltage plot of SCLC behaviour, (a) Ohmic region, (b) Child's law due to shallow trapping, (c) Trap-filled limit, (d) Child's law after trap saturation.

In polymers, the amorphous nature of their structure allows for a very high density of defects and impurities, with wide ranging trap depths and energies. The effects of trap filling are therefore smoothed out and often obscured when trying to observe them in practice.

2.9 De-trapping and the Poole Frenkel effect

Sufficient kinetic energy can be applied to trapped electrons, exciting them out of the trapping site and into the conduction band of the insulator. These electrons are now free to drift through the material as charge carriers, being detected as a small current. This thermal de-trapping method can be used to probe trap depth and density throughout a sample material. The mechanisms associated with de-trapping are similar to those seen in thermionic emissions.

Electron de-trapping may also occur when sample materials are subject to very large electric fields. An applied field will create an offset between opposite walls of the trapping potential. With a large enough applied field there may be sufficient lowering of one of the barrier walls to allow electron confinement to be lost. This field induced de-trapping phenomenon is known as the Poole-Frenkel effect. It is also possible for electrons to tunnel out of traps into the conduction band of the insulator. This is aided by the reduction and effective narrowing of the potential barriers by the applied electric field. The effect on the trapping potential has great similarity to the effects seen in Schottky emission discussed earlier. Figure 2.11 below shows the effects on the trap potential before (a) and after (b) the application of an electric field.



Figure 2.11: Trap potentials with (a) zero applied E-field and (b) High applied E-Field causing loss of confinement and electron tunnelling.

2.10 Charge Hopping

In a highly defective material trapping sites can often be in close proximity to each other. This allows electrons to move from one trapping site to an adjacent site through a process known as hopping [40].

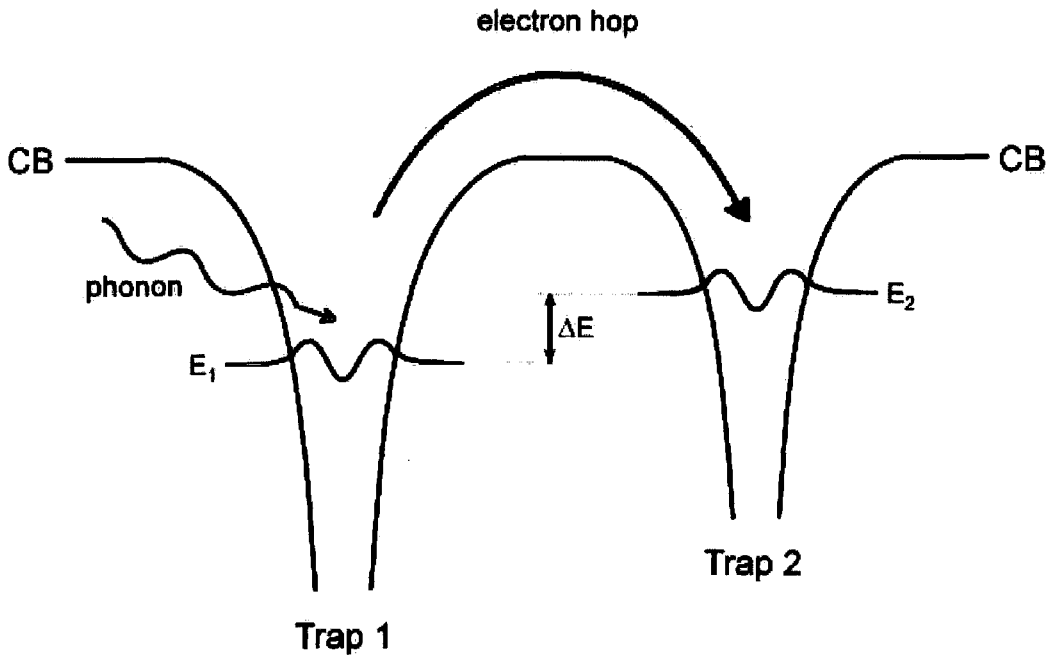


Figure 2.12: Thermally assisted hopping of electrons between trapping potentials

Thermally assisted hopping occurs when a phonon is absorbed, providing enough energy for an electron to overcome the barrier to an adjacent trapping site. Once the electron reaches the second site a phonon is emitted. In cases where phonon energies are not large enough to promote thermally assisted hopping, electrons may still move to adjacent traps through another mechanism. If the adjacent trap is of similar energy level then electrons may tunnel from the first trap through the potential barrier reaching the second trap. It is most likely that the electron will find a trap of similar energy at a distance further than its nearest neighbours. The distance of the “hop” is therefore variable and the name Variable Range Hopping [39] is used to describe the mechanism. The range of the hop is dependant upon the associated energy difference ΔE between the two trapping sites. Slight miss-matches in energies of the electron between trapping

sites is accounted for by emission or absorption of a phonon. The requirement of phonon interactions means that hopping conduction mechanisms are therefore temperature dependant. The overall process is analogous to phonon assisted tunnelling [41].

The phenomenon detailed above (SCLC, de-trapping and hopping) give mechanisms of electrical conduction through insulating materials, including the insulating regions of metal-polymer composites. This will effect the overall electrical conduction of the composites, particularly those relying upon percolation mechanisms [42]. A result of this is that metal-polymer composites can depend upon an electrical history of the material. Trapping sites may remain filled from a previous current-voltage sweep, effecting subsequent sweeps on the material.

2.11 Fowler-Nordheim Tunnelling

So far the simplest case of quantum tunnelling has been looked at. However the potential barrier between Nickel particles in QTC is a little more complicated. The first modification to the simple model is to consider the effect of an applied electric field across the barrier.

When applied across a square potential barrier it is found that an electric field will cause the barrier to be lowered on one side as shown in figure 2.13. The tunnelling current density is a function of the potential V at any point x through the barrier. Thus reducing the potential like this makes it easier for electrons to tunnel through.

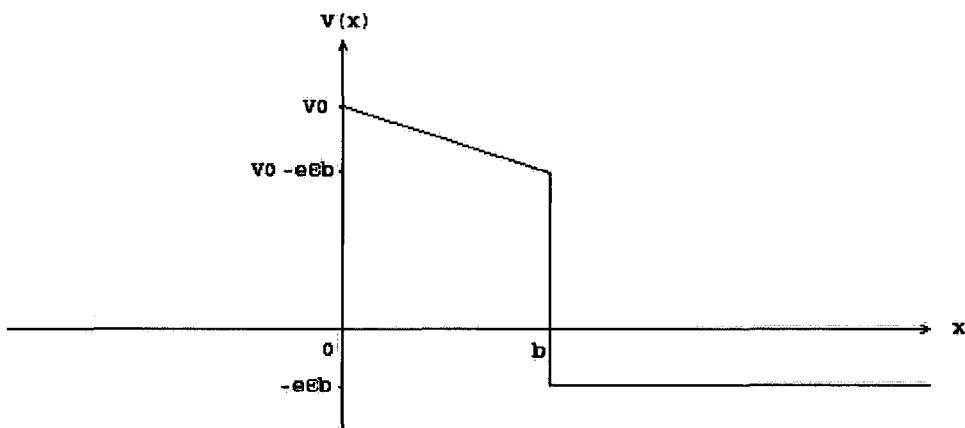


Figure 2.13: Potential Barrier with Applied Electrical Field

This can be described as a triangular barrier with the barrier potential now taking on the form $V(x) = V_0 - eEx$, where e is the charge on an electron, E is an externally applied electric field and x is the distance into the barrier from the front edge. Therefore using the WKB approximation (see Appendix B) the current density is now given by Eqn 2.27 [43].

$$J = A_0 \exp\left(-\frac{4}{3} \left(\frac{2m}{\hbar^2}\right)^{1/2} \cdot \frac{(V_0 - E_x)^{3/2}}{eE} \cdot b\right) \quad \text{Eqn 2.27}$$

This equation gives an approximation as to the effects of applying an external field across the barrier.

Fowler-Nordheim emissions occur when a very large electric field is applied across a barrier [45], such that the potential is dramatically distorted, figure 2.14.

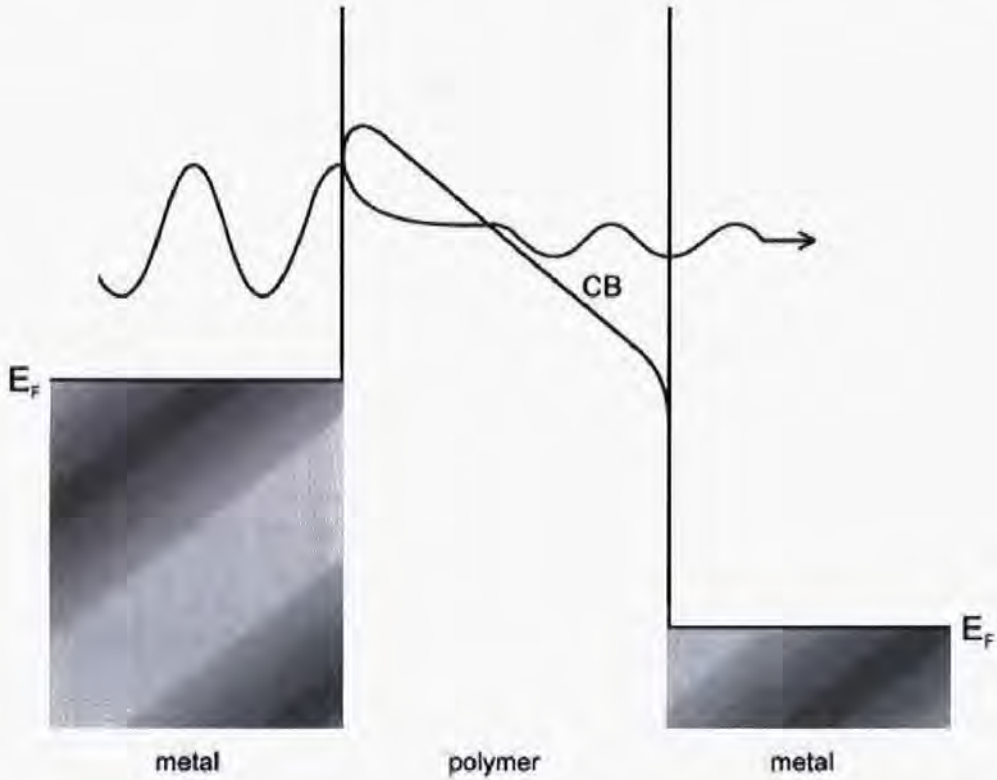


Figure 2.14: Fowler-Nordheim Tunnelling potential

The barrier is lowered now such that the electrons that tunnel through the barrier are injected into the conduction band of the insulator. In all the previous barrier models, even though some were lowered to a certain extent, the electron was emitted through the barrier into the conduction band of the second metal on the other side, region III.

The current density passing through the barrier must therefore be altered to accommodate the changes. It is found that there is now a quadratic dependency of the current upon the applied field. Because the electrons are now tunnelling into the conduction barrier of an insulator Child's Law must be considered,

which introduces a dependence of the current density to the electric field squared.

Considering Childs' law along with the work function energy, the current density J for a combination of thermionic and field assisted tunnelling mechanisms can be presented;

$$J = \frac{A_0 E^2}{\phi} \exp\left(-\frac{4}{3} \left(\frac{2m}{\hbar^2}\right)^{1/2} \cdot \frac{(V_{MAX} - \bar{E}_x)^{3/2}}{eE} \cdot b\right) \quad \text{Eqn 2.28}$$

Chapter 3, Electronic Properties of QTC

3.1 Experimental Introduction

The purpose of this set of experiments was to investigate the characteristics of QTC under high uniaxial compressions and to explain how and why the characteristics occur. Previous experiments have been undertaken in this area however compressions have only been examined up to about 25% (by length). Assumptions have been made as to how QTC will behave at much greater compressions but no work has been undertaken to date.

It is hoped that the results of these experiments will allow the author to describe more fully the characteristics of QTC and through their investigation attribute them to specific theoretical phenomena.

Further experiments are then conducted in order to investigate the effect of adding acicular filler particles to the composite. A range of loading fractions and start resistances are examined in order to characterise the new composite in terms of charge storage in the samples, noise in the current-voltage response, and sensitivity to mechanical force.

3.2 Sample Composition and Preparation

Samples were prepared and supplied by Peratech according to methods previously described [2]. There are two types of QTC used for the different aspects of the experimentation. The first set of samples consisted of QTC and is referred to as Pill Samples, having dimensions 4 mm x 4 mm x 1 mm. The pill samples are a composite of Inco Nickel Type 123 powder and Dow Corning Silastic T4 silicone rubber mixed by weight to the ratio 5:1 Nickel to Silicone. Samples are made on a continuous reel with each pill simply cut off the reel, thus making sample to sample variation very small.

The second set of samples was those used to investigate the effects of applying a third medium to the QTC mix. These were a composition of Inco Nickel Type 123 powder and Dow Corning Silastic T4 silicone rubber. However they also had acicular type electro-conductive particles added to them in small fractions. The loading ratios of Nickel and acicular filler were varied for comparison over six samples. They were referenced as described in table 3.1.

Sample Number	Nickel : Silicone (By weight)	Acicular Filler
1	4:1	0g
2	4:1	2g
3	4:1	4g
4	5:1	0g
5	5:1	2g
6	5:1	4g

Table 3.1: Loading ratios of fillers in samples

As part of the preparation process the acicular filler samples were placed in a vacuum chamber in order to evacuate any trapped air pockets from the material. However it was found at a later point that Sample 2 had not been subject to the vacuum process in its preparation and thus had trapped air pockets throughout.

This enabled a comparison for benefits of the preparation process but made it difficult to compare Sample 2 to the other samples. As a result only samples 4, 5 and 6 were used for testing. These correspond to a nickel loading of 5:1, which is the loading used in the pill samples and found in previous works to be the optimum nickel loading. The samples themselves were manufactured as sheets of QTC, which were approximately 1 mm thick however this did vary slightly and the exact thicknesses were measured. 4 mm x 4 mm samples were then cut from the sheet to provide good correlation with previous work undertaken on the pill samples.

3.3 Experimental Setup

The first setup was to measure the conductivity of the QTC as a function of force applied to it. A simple clamp setup was used to hold and compress the QTC samples. A Mitutoyo Force Meter was set up behind one clamp face. The second clamp jaw was fixed to a moving platform that could be controlled using a vernier screw. The vernier screw allowed samples to be compressed on a small scale accurately. The clamp jaws were constructed of steel, which allowed good conduction both electrically and thermally. The clamp also acted as a heat sink reducing greatly any heating effects on the QTC behaviour. This was important as sample heating can lead to PTCR effects which may mask the processes we are interested in for these experiments. The two conducting steel blocks at the face of each jaw were connected directly to a Kiethley 2420 high current sourcemeter using copper wires. The sourcemeter was connected to a computer via a GPIB card which allowed current-voltage sweeps to be made automatically in a repeatable manner using LabView software to control the experimental parameters. Figure 3.1 summarises the experimental setup.



Figure 3.1: Schematic of experimental setup

It also provided a method of recording results of each experiment directly into excel spreadsheets. Figure 3.2 below shows a photo of the experimental setup.



Figure 3.2: Setup to measure Resistance as a function of Force

In order to then measure resistance as a function of actual compression rather than applied force the rig was adjusted. This was because the Mitutoyo Force Meter had a degree of movement in it and any measurements of compression of the sample using the vernier scale was a combination of sample compression and the movement in the force meter. The Mitutoyo Force Meter was replaced by a fixed block of steel; this is shown in figure 3.3.

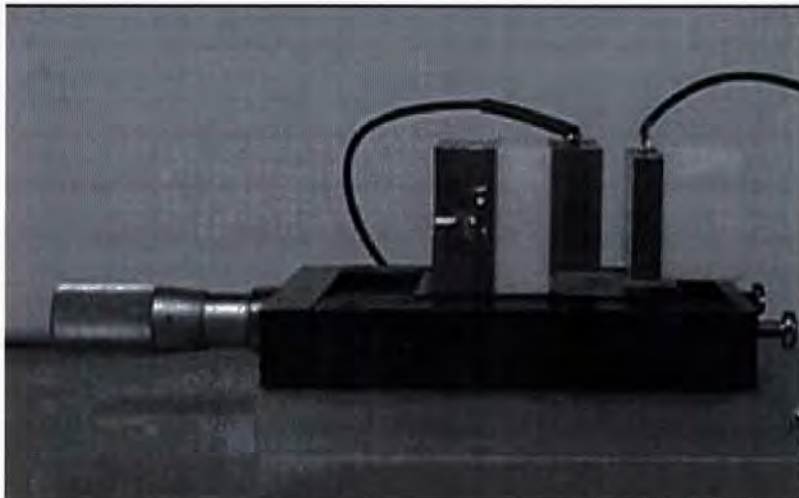


Figure 3.3: Fixed Jaws to measure Resistance as a function of Compression

This setup was connected to a computer in the same way as the previous setup.

3.4 Methodology

Force and Compression Experiments

The first experiments were developed to quantify sample resistances as a function of force and were set up as discussed above using QTC Pill Samples. It was initially envisaged that the entire set of compression experiments could be measured as both a factor of applied force and also actual compression of the sample. However it was found that due to the movement in the Mitutoyo Force Meter it was very difficult to accurately measure both force and compression on a sample simultaneously. Therefore the first results were a measure of resistance of the samples as a function of force and a reference chart was produced. This reference chart could be compared with later results from compression experiments should the value of the applied force be required.

For the force measurements samples were measured in the range of 0.5 N to 150 N, at a constant current of 10 μA . The internal resistance of the clamp setup was measured to be 0.0027 Ω . The same pill sample was used as the force was slowly increased in small increments. A number of runs were undertaken using a different sample for each to check repeatability.

Compression measurements were then undertaken using the fixed clamp set-up. Sample resistances were measured for compressions of 0 to 0.8 mm (which equates to approximately 0% to 80% compression) at a constant current of 100 μA . The same pill sample was used as compression was increased, but a number of repeat runs were undertaken on new samples to check repeatability.

Current-Voltage Sweeps

The main focus of the experiment was the current-voltage effects of QTC at higher compressions. Having already determined the basic resistance characteristics of the pill samples current-voltage sweeps were conducted in the range of compressions where the samples became conductive. This was from

just above 10% compression to 80% for the Pill samples. Current-voltage sweeps were conducted at compressions of 5% increments. Each sweep was conducted with a fresh sample, from the same batch, to eliminate any charge trapping effects of QTC.

After a number of preliminary tests, sweeps were ranged from 0 up to 0.5 V. The sweeping was fully automated and controlled by a LabView program. Voltages were incremented at 0.01 V. The limit of 0.5 V was necessary as at higher compressions the samples were very conductive and large currents were produced which were outside of the measurable range of the source meter when the voltage exceeded this range.

Charge trapping effects were investigated. This was done by running multiple current-voltage sweeps on single samples at a fixed compression. Ten consecutive sweeps were run at each chosen compression.

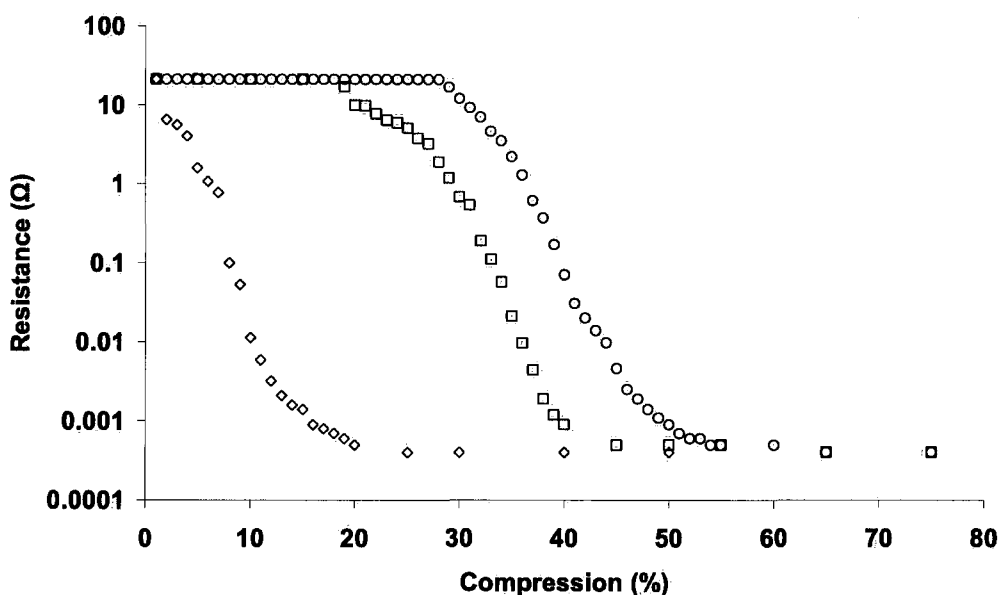


Figure 3.4: Compression responses of 3 sample types. Compression ranges:
 \diamond = Sample #3 (0.5 > 24 %), \square = Sample #5 (22 > 40 %),
 \circ = Sample # 6 (27 > 47 %).

The second part of the experiment was to look at the properties of the acicular filler loaded QTC. Three compositions were investigated. A similar treatment was undertaken to that applied to the standard QTC samples.

Sample resistance was measured as a function of percent compression for each of the three samples types containing different fractions of acicular filler. Figure 3.4 shows the results of these preliminary tests. It is evident from this data that each of the three samples reaches the sensitive, more conductive region at different applied compressions. It was therefore necessary to design the current-voltage sweep experiments to correspond to these more sensitive regions. The optimum compression ranges were therefore derived from this data to provide similar resistance ranges for like comparison between the three sample types when conducting the current-voltage sweeps.

Multiple sweeps were also employed to investigate charge accumulation. The current voltage sweeps on the acicular filler loaded samples were done over the voltage range 0 V – 20 V.

3.5 Results and Analysis

In this section the results from all the experiments will be presented. An analysis of the results will be given and relation and explanation made with respect to the theory discussed in previous sections.

3.5.1 High Compression Responses

Force Response

The first set of results obtained were those of the response to force of the pill samples. For each experiment a new sample was used. Samples were all taken from the same production batch to ensure matching compositions.

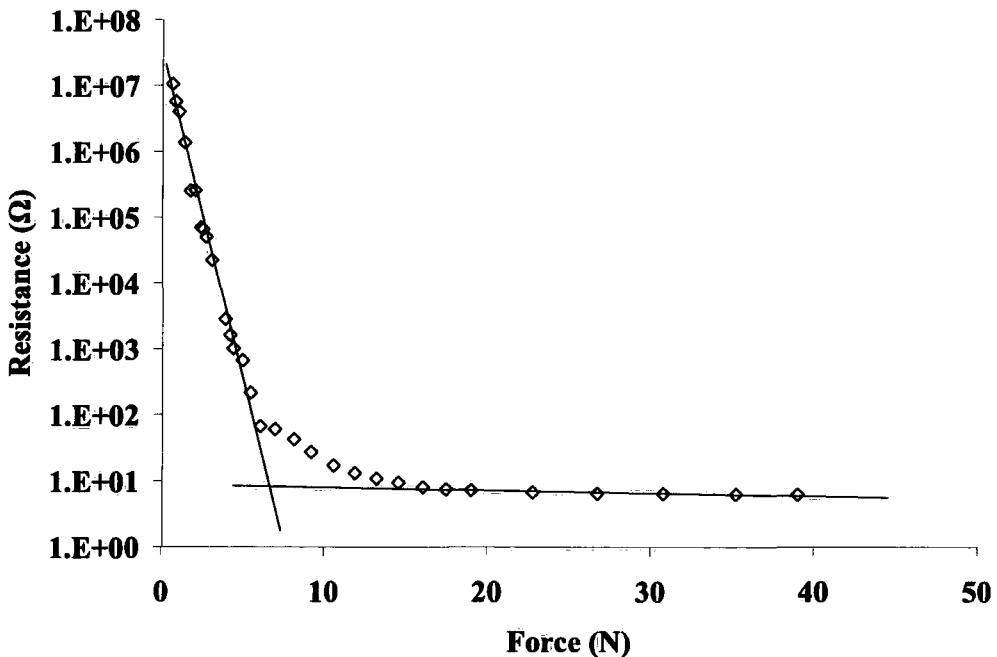


Figure 3.5: Response of a Pill Sample to an external uniaxial Force

Figure 3.5 shows an example of the resistance change of QTC as a function of applied force. As the silicone polymer compresses at a rate linear to the applied force, the resistance decreases exponentially corresponding to the trends described by Fowler-Nordheim tunnelling theory. At applied forces greater than

20 N sufficient current pathways are produced across the sample for the change in response to eventually become less than the sensitivity of the test equipment. This can be seen as a transition in figure 3.5 at 20 N.

Prior to transition it is seen that the exponential response falls off. The straight line on the log plot begins to curve between 10 N and 20 N. This is attributed to deformation of the sample laterally under heavy compression (figure 3.6). In this region the maximum number of effective conduction pathways is being approached and so change in resistance is becoming more dependent on the change in shape of the sample rather than new pathways being created. However lateral spread will be compensated somewhat by increase contact area, it would be extremely difficult to maintain a regime where only compression through the sample was upheld and so this effect is limited.

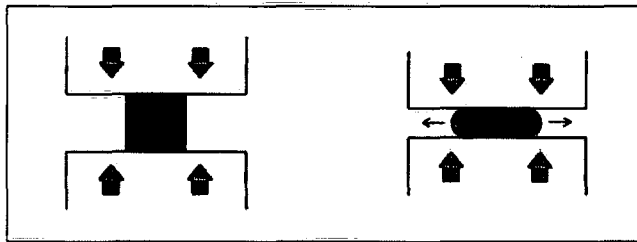


Figure 3.6: Deformation of Samples at higher compressions

As compression is increased further a regime where there is little response is observed. Here the number of conductive pathways has saturated and the trap filled limit of the material is coming into play, this is discussed further in the next section. This sequence of regimes can be described in terms of a percolation network, constructed in a Link-Nodes-Blobs structure with the conductive “Links” represented by a Fowler-Nordheim tunnelling mechanism, rather than a direct contact. The exponential region of figure 3.5 relates to the reduction of tunnelling distances between particles followed by a region where the effective percolation threshold is exceeded and sample deformation takes effect. The whole system is analogous to the effective medium models discussed in section 2.3 with the average resistance between all particles replaced with a

mean-field potential barrier representative of the Fowler-Nordheim tunnelling mechanism.

A short set of repeat measurements were taken to measure force as a function of compression. This was done in order to evaluate whether structural rigidity affected the compression response. It is hypothesised that at high compressions the volume fraction of filler particles may affect the dynamic properties of the composite. Under high compression whilst the silicone rubber continues to compress aggregates of metal filler do not and resist overall sample compression. Furthermore a breakdown of the filler network within the composite may also contribute to changes in dynamic response. Figure 3.7 shows the results from the force-compression tests. It can be seen in the data presented that there is a smooth continuous trend in compression under an applied force. There are no distinct changes that would relate to a breakdown in the filler network or a regime change where contacting filler aggregates provide resistance to compression. It is maintained based on this that the change in electrical response seen in figure 3.5 is an artefact of sample deformation under compression and limitations of certain conduction mechanisms.

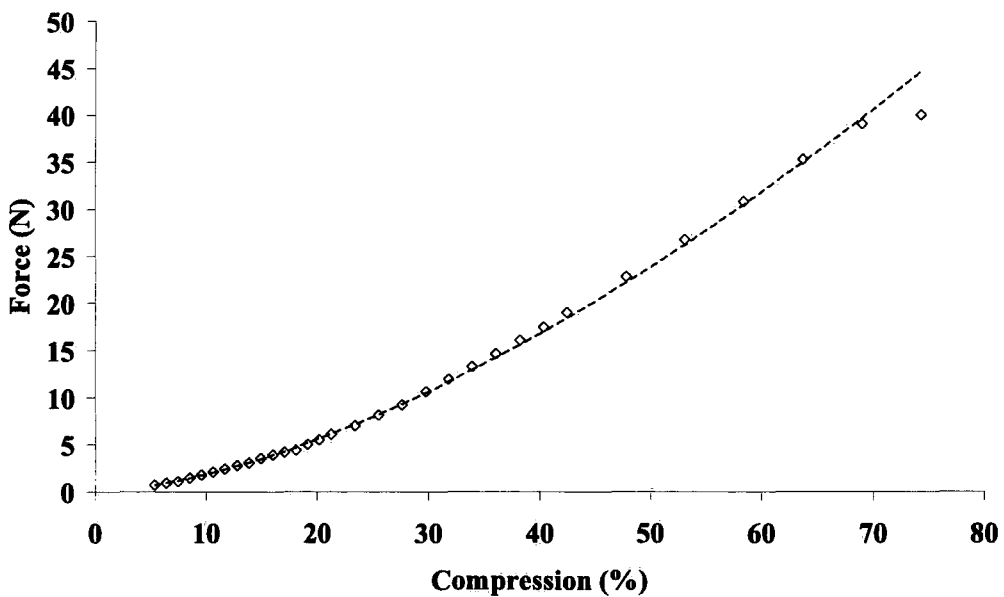


Figure 3.7: Measured compression as a function of applied force for QTC

Direct conventional percolation in the Pill samples is not evident even at high compressions where the relative concentration of metal particles is above that of the percolation threshold of the composite. Examination of previous work [12] involving SEM and TEM images of QTC samples shows that in the mixing process of the QTC, nickel particles are fully wetted by a layer of polymer creating an insulating layer between particles.

Analysis of SEM images has also shown that the dispersion of nickel particles throughout QTC materials is not even (figure 3.8).

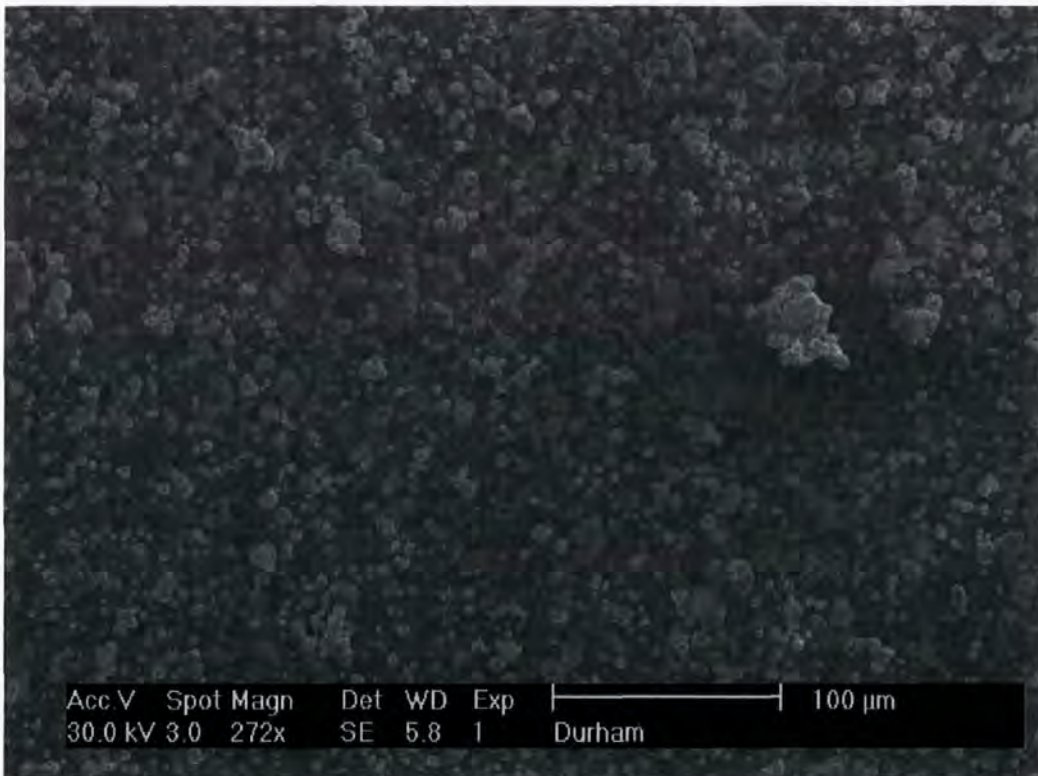


Figure 3.8: SEM image of standard QTC illustrating heterogeneous nature

It is seen that there is accumulation of particles in certain areas forming aggregates, figure 3.9. These vary in size and they are not evenly distributed throughout the samples. The QTC material therefore has some areas with large concentrations of nickel particles in it and other areas that are relatively sparse in nickel. This heterogeneous distribution of filler particles lends itself very well to being described by the Links-Nodes-Blobs model described earlier. The blobs

relate to the aggregates of nickel with the links consisting of Fowler-Nordheim tunnelling pathways between aggregates.



Figure 3.9: Example of an aggregate of wetted nickel particles.

The effects of this heterogeneous morphology is evident when looking at small sample sizes, specifically the granule samples used in the vapour sensors discussed later. It means that sample to sample variation is common, most noticeably the start resistances created at specific applied compressions. It is not uncommon to see one sample at 10% compression have a 10Ω resistance and another sample from the same batch at 20Ω when looking at small samples, below 0.5 mm^2 in size. It is often better for industrial application to group samples in terms of start resistance as well as other properties. The reason for this heterogeneous structure lies with the patented gentle mixing process. This needs to be maintained in order for the fine point like surface features to survive and allow quantum tunnelling, the down side being the uneven mixing of the material. A longer mixing process would even out the nickel distribution but would also smooth the surfaces of all the nickel particles [12]. When using the pill samples however they are sufficient in size that the scale of the uneven distribution is much smaller than their overall size. For these and larger sized

samples there is sufficient averaging over their volume to reduce the sample to sample variation. It is not fully removed though and still needs to be taken into consideration when applying QTC to any applications. The 4 mm² samples used in these experiments showed a variation in resistance of 20% based on resistance variation of 8 identical samples at 20% compression with an average resistance of 61.3 μΩ.

Compression Response

Having measured sample resistance as a function of force it was then measured as a function of physical compression of the sample.

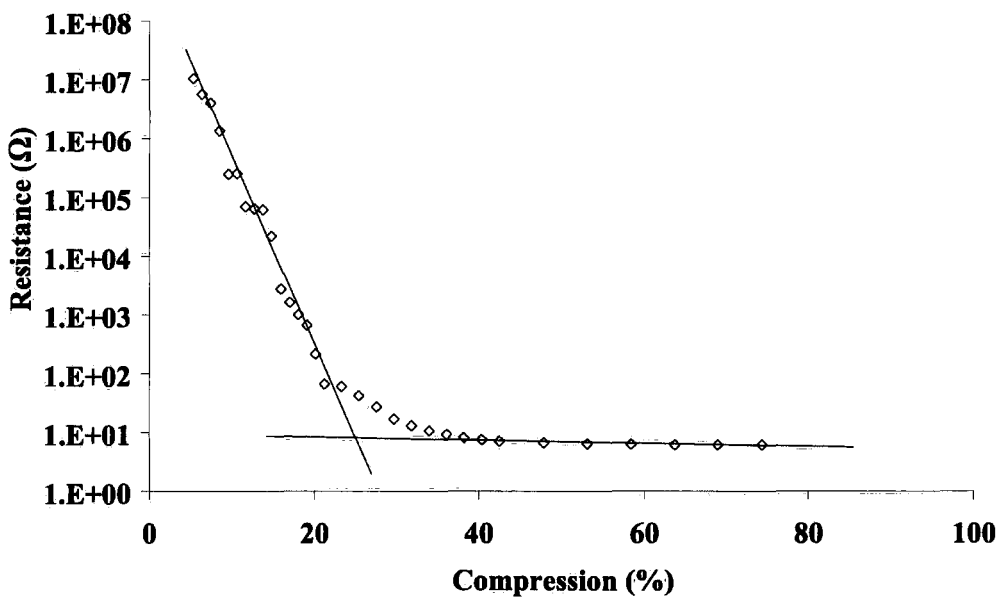


Figure 3.10: Pill Sample resistance as a function of compression

It is clear to see that this set of data follows the same characteristics as the previous force response in figure 3.5. It can be seen that the sample shows very little further change in response at higher compressions. Evidence of sample deformation is more evident as the resistance response begins to curve when 20% compression is exceeded.

Current-Voltage Characteristics of Pill Sample

A high field sweep was conducted, figure 3.11. This shows a typical I-V response of a Pill Sample on a single I-V sweep to 40 V.

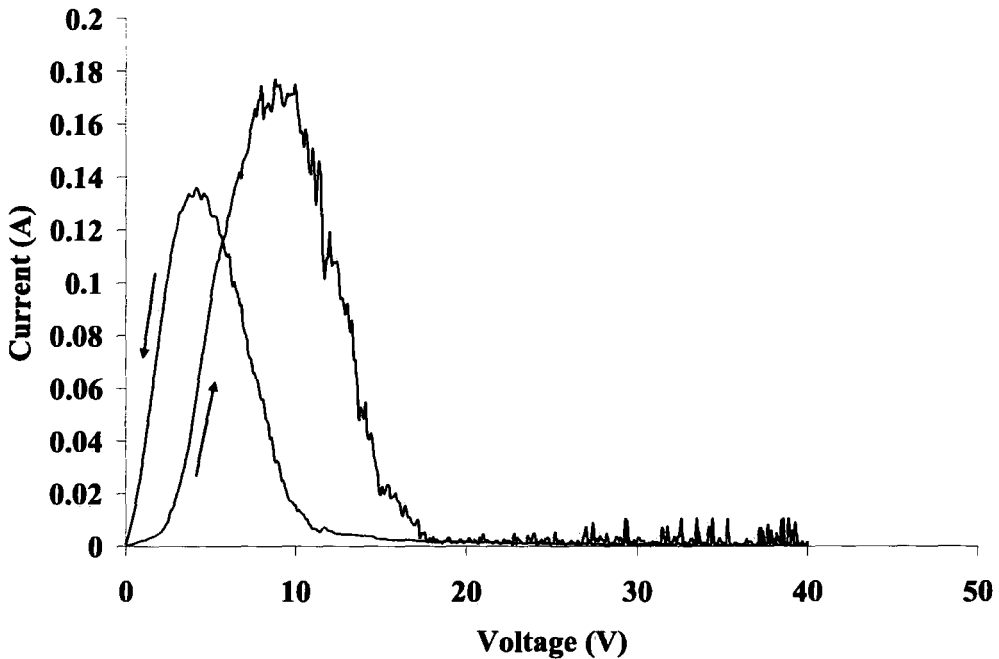


Figure 3.11: I-V sweep at 20% sample compression, start resistance 440 Ω

The main characteristic is the difference in resistance on the up sweep to that on the down sweep, emphasised by the two distinct peaks in the graph. This hysteresis can be explained by a conduction model based on the trapping and pinching of charge pathways within the QTC samples. As a current is applied across the sample there will be a number of pathways opened up each of which consists of a series of potential barriers that are overcome through a Fowler-Nordheim field assisted tunnelling mechanism. As the applied field to the sample is increased then barriers with greater potentials are overcome. There will however be pathways ending within the sample somewhere as a dead end. Charge will also be retained in the trapping sites of the polymer following charge injection from the nickel particles into the polymer insulating layer around them. Charge will then accumulate in these dead ends and within the insulator's traps as the direction of the applied field prevents the charge from

returning along the pathway it came down. As these dead ends store more trapped charge they will produce a local field that acts as a potential barrier to other nearby conduction pathways, resulting in them becoming ‘pinched’ off.

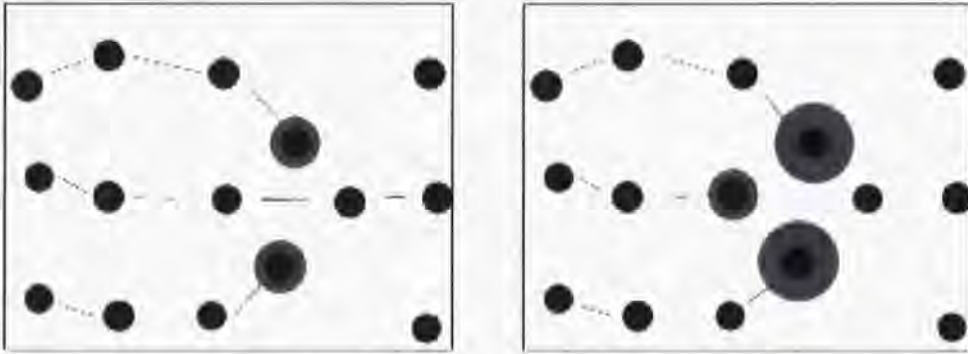


Figure 3.12: Charge storage and pinching of pathways

Thus a feedback mechanism is setup and the overall conduction through the sample is reduced. This is shown in figure 3.11 where the current flow in the sample begins to fall off as the applied voltage exceeds 10 V on the up sweep, the pinching is taking effect. The current then remains at almost zero up to 40 V as equilibrium is reached where all of the trapping sites are filled and there is a limited current. An analogy to SCLC in insulators can be made here with respect to the charge pinching behaviour made on the macroscopic level. The pinching causes charge trapping in the dead ends which eventually fill as voltage rises, in the same way trapping sites fill in a SCLC regime. A limited current is then seen as all the trapping sites are filled. There will also be charge injection and trapping of charge carriers on the microscopic level within the insulator and some effects of actual SCLC occurring.

As the applied field is reduced, charge remains trapped in the dead end sites until the electric field has fallen to a level whereby the trapping potential acting on the charge is sufficiently small that the charge can leak back out of the sample. The rate at which charge leaks from the trapping sites is much slower than the rate they are filled, as there is no negative voltage forcing them back out. The second peak in figure 3.11 is observed when sufficient trapping sites

have released their charge and pinching of neighbouring pathways is reduced. The second peak occurs at a lower voltage indicating the slower rate of charge release. Upon returning to zero applied field not all the charge has left the sample and so the end resistance of the sample is lower than its start resistance. This will be an artefact of charge that was unable to leave the sample, either through being trapped at impurities in the insulator as is described in SCLC behaviour, or also trapped in some pinched off pathways whose potential barriers remained even after the applied voltage returned to zero. Looking at the difference between initial and final sample resistances is a useful method for monitoring the amount of charge storage within QTC.

A further observed characteristic in figure 3.11 is the noise on the downward section of the first peak. This is the region where charge is beginning to accumulate on the filler particles at the dead end pathways and also in the trapping sites within the insulator. The observed noise in the data is caused by redistribution of charge within the sample as local fields at charge trapping sites exceed their local trapping potential, resulting in a cascade of charge to the surrounding sites [46]. This discharge to the surrounding sites may occur at any point up to the full charging of the trapping site. The sudden discharge to neighbouring sites is the cause of the observed RF emissions. The sharp nature of the white noise indicates spark discharging to the samples surface as the main source of RF emission, characterised by the single sharp spikes seen in the current-voltage plot, figure 3.11. This data also shows regions of linked cascading spikes among the single sharp spikes. It is believed that these occur due to RF emissions produced as a result of oscillatory decay of charge resonating between two nearby trapping sites. Further RF emissions may also be produced by coupling with neighbouring sites causing an induced oscillatory decay in these leading to further discharges.

Low field Sweeps of Pill Samples

Due to the relatively low start resistances created by high compressions currents passed at 40V were exceedingly high. For safety and to prevent unwanted heating of the sample, cycling was limited to sweeps up to 0.5V. Figure 3.13 shows an example of a low sweep data set.

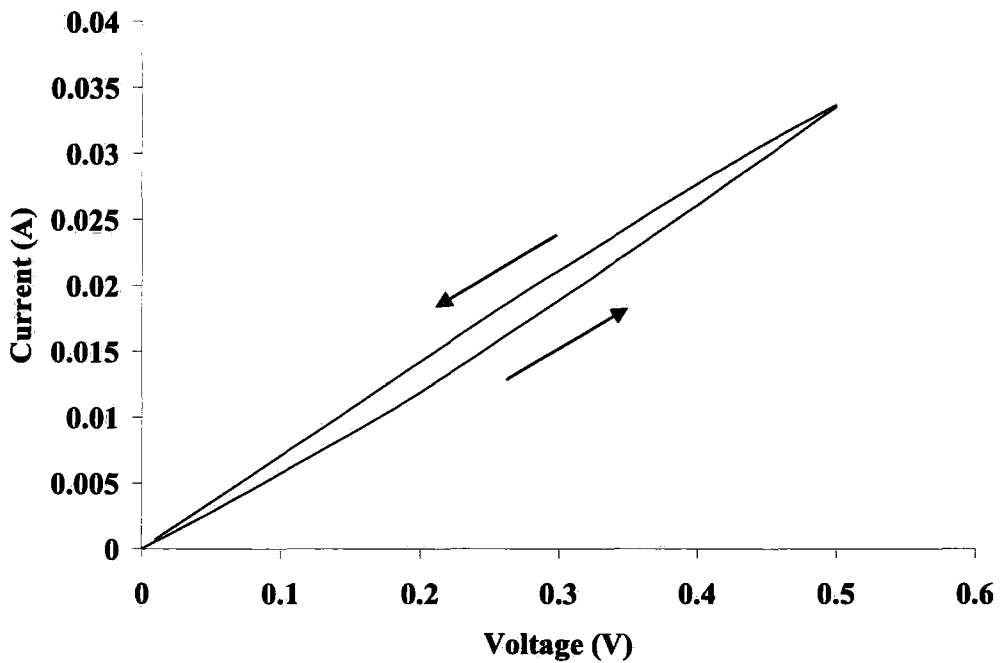


Figure 3.13: Low field sweep on pill sample

The next stage of experimentation was to evaluate how this charge storage effect and hysteresis are affected as a function of start resistance, i.e. as the physical compression of the samples was varied.

This was initially observed in each of the IV sweeps, the graphs showing less and less hysteresis for each successive sweep at a greater compression. These graphs were used to calculate start and end resistances of samples from their gradients. These were calculated using a linear approximation in of the first 0.05 V of the up sweep and the last 0.05 V of the down sweep, applying a simple $V = IR$ relation. It was then possible to find the ratio of up sweep to down sweep and

plot them against start resistances to examine how charge storage in samples varied under increasing compression. Figure 3.14 shows this data.

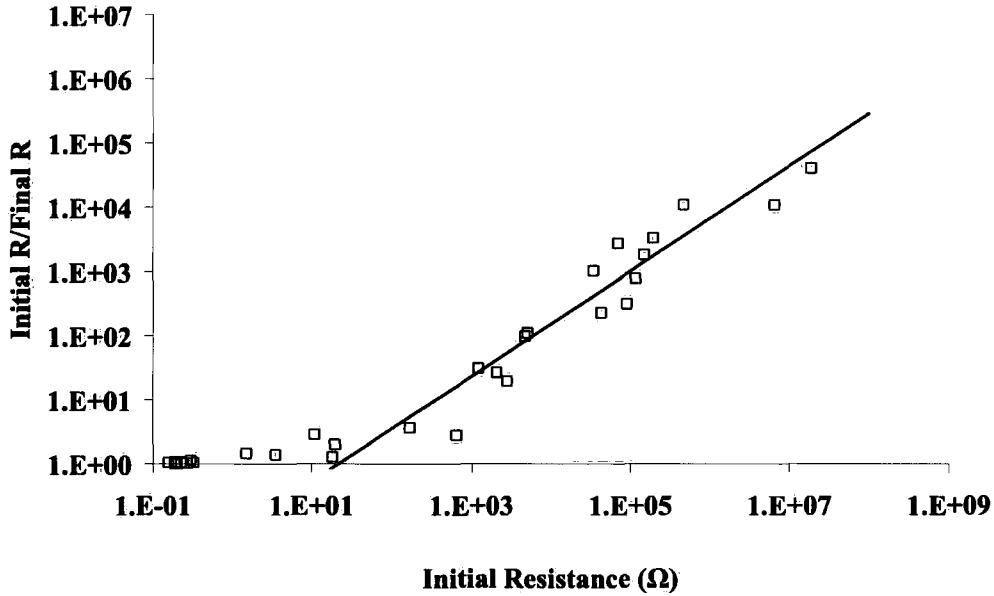


Figure 3.14: Initial to final resistance ratio as a function of initial resistance

In figure 3.14 the data begins to show a ratio approaching unity below 100 Ω indicating that start and final resistances are similar and there is little charge storage at start resistances below this value, the samples are showing Ohmic behaviour with no charge trapping or pathway pinching. This is not a sharp transition, it is seen that the amount of charge storage in the samples increases with increasing start resistance. This low initial resistance (below 1 k Ω) data was all collected using low voltage sweeps. This was a requirement due to the limitations of the current handling capabilities of the Kiethley Multi-meter being used. A current of 3 A was the upper limit of the Kiethley, this equated to a voltage limit of 0.5 V when measuring samples in the low resistance range. A selection of sweeps conducted in the higher start resistance range (above 1 k Ω) were repeated but with an extended voltage range, such as the high fields sweep shown in figure 3.11, it was found that the data fitted to the trends seen in figure 3.14. It is assumed that using a high current source meter future research could show that high field sweeps conducted at low start resistance would exhibit the same unity ratio between start and end resistance as seen in the low field sweeps.

Repeat Cycling of the Pill samples

The final stage of experimentation on the pill samples was to investigate the effects of cycling through a number of repeat cycles on a sample at a fixed start resistance. This was then repeated over a range of different start resistances, produced by applying different amounts of compression.

IV cycles were run for a range of sample compressions from 15% to 70%. Investigation of the graphs produced over a number of repeat cycles showed falling sample resistance over each consecutive cycle on the same sample. This behaviour was observed in the data from all the sample compressions tested up to 70% compression which relates to the sample becoming Ohmic in nature as found in the previous section. It was noted that the amount of charge storage over repeat cycles was reduced as the initial compression on the sample was increased. A selection of data is summarised in figure 3.15 below. Ratios of initial to final resistance are shown against cycle number, with each data set representing a different start compression.

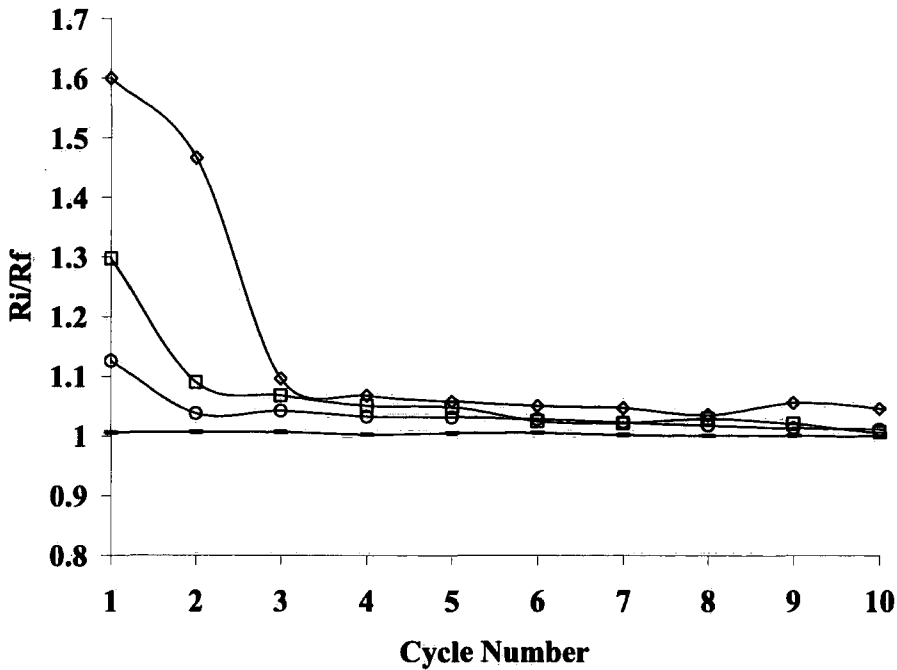


Figure 3.15: I-V repeat sweeps, at different start resistances, compressions:

◇ = 15%, □ = 20%, ○ = 50%, - = 70%.

Examination of the data in figure 3.15 shows that there is no resistance change over repeat sweeps at 70% compression when the sample is Ohmic. It shows also that there is significantly more charge storage in the first two cycles in all of the compression settings and the amount of charge trapped in each consecutive cycle becomes less each time.

The emphasis of this experiment is to investigate the responses of QTC at higher compressions so a closer examination of the cycling at 70% compression was made. The results from this data set proved to enhance the conclusions already made, that highly compressed QTC is Ohmic in behaviour. The number of trapping sites in the material, both within the polymer and macroscopic dead end trapping sites is reduced by the high compression regime. There is a high probability that those trapping sites remaining are full and the trap filled limit of the material has been exceeded. Any further charge injection will not be affected by charge trapping and so an Ohmic response is seen; as shown in figure 3.16. Here there is no hysteresis within any one cycle and only a very minor spread of resistance from the first cycle to the final one.

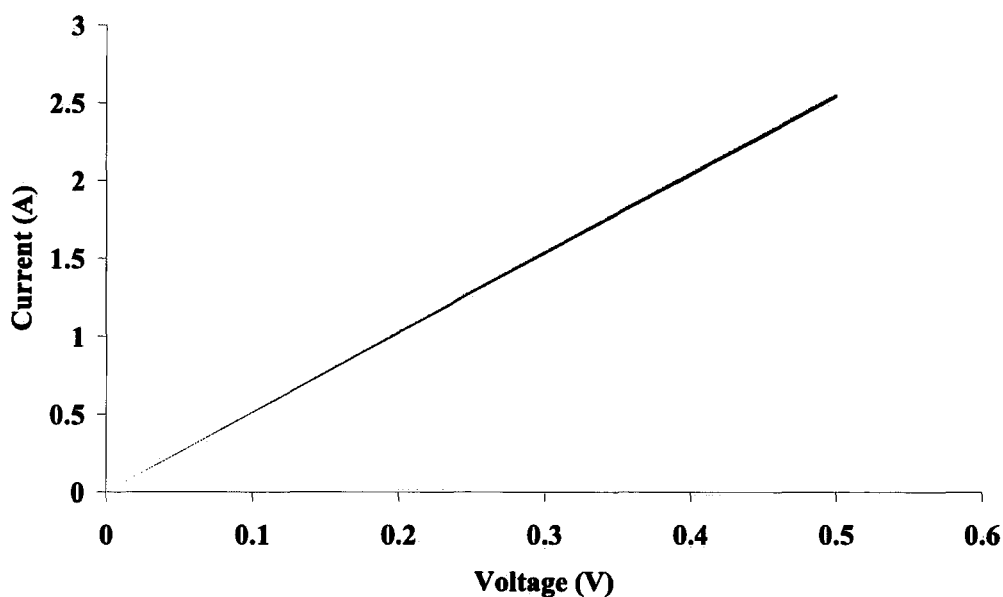


Figure 3.16: All 11 I-V cycles superimposed at 70% compression

Figure 3.17 shows the data presented in terms of resistance as a function of cycle number. This shows a roughly steady resistance for the first 6 cycles followed by a steady decrease over the following 5. The pattern is similar in both up sweep and down sweep indicating that it is not charge storage; this would be highlighted by differing resistances on up sweep to down sweep. The general drop in resistance over repeat cycling indicated that Joule heating may be causing thermal expansion in the sample. The sample is being held between two stationary clamps, thus swelling of the sample ultimately forces it to expand laterally increasing the surface area and so reducing resistivity. This explains the downwards trend seen after cycle 5 in figure 3.17. The slight upward trend seen prior to cycle 5 is attributed to some slight expansion that can occur, before lateral spreading, effectively separating particles and increasing barrier thickness between them. Further influence may also arise from competition between thermionic and field emissions within the samples, which have opposing responses, field emission decreasing and thermionic increasing to temperature increase. However it is believed that these effects would be overwhelmed by the changes caused through lateral expansion of the material. A quantitative assessment of these ideas is suggested as further research for a later project.

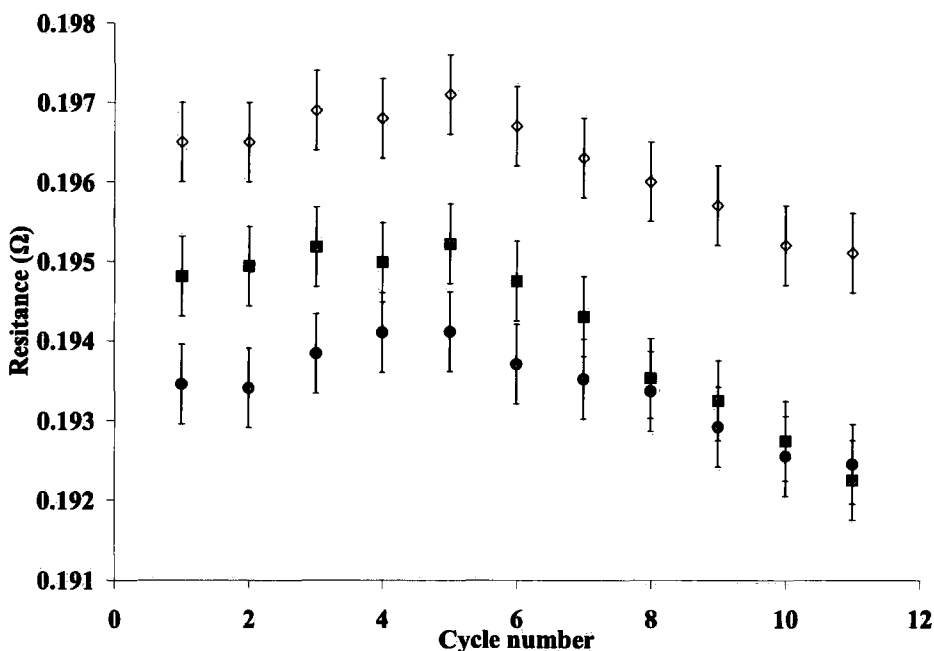
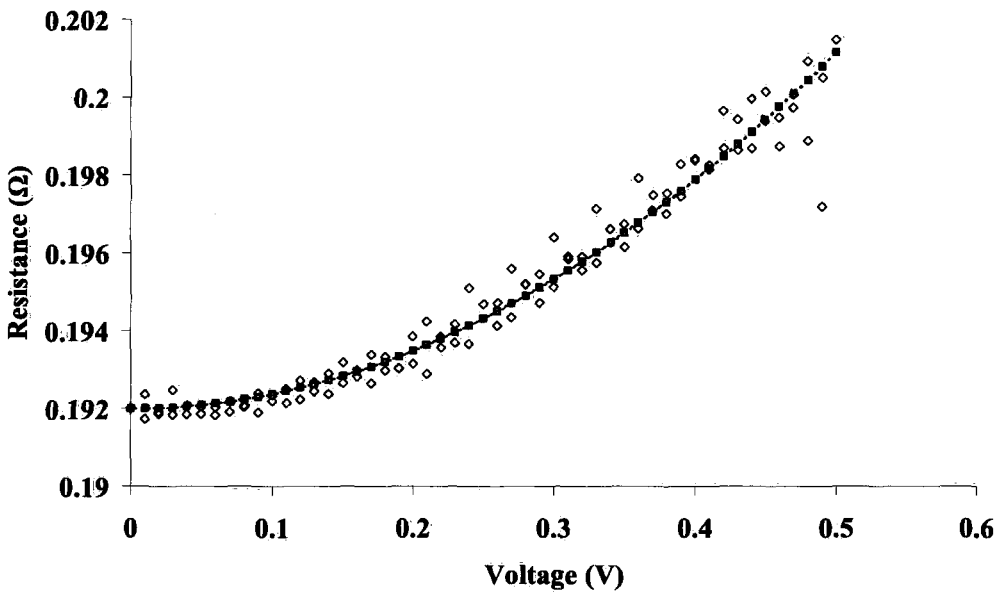


Figure 3.17: Resistances as a function of cycle number for 70% compression pill sample, ■ = R up, ● = R down, ◇ = R @ V_{max}.

Figure 3.18 shows the calculated resistance at each voltage step of the sample from the eleventh repeat cycle of a current-voltage sweep. The model fitted over the experimental data was calculated using a simple definition of power, equation 3.1.

$$P(t) = V^2(t) / R(t) \tag{Eqn 3.1}$$

Where P is power dissipated, I is current and V voltage, all recorded at time t . This equation represents the power required to heat the sample through Joule Heating. The data for the model fit was normalised to the experimental data by simply multiplying through by a numerical constant.



*Figure 3.18: Model of Joule heating compared to observed data,
 ◇ = data, ■ = model fit.*

It can be seen that the model fit matches the measured data very well; confirming that at high compressions, the current flow through QTC can produce Joule heating when subjected to repeat cycling.

3.5.2 Addition of Acicular Filler

Compression Response

The second section of results to be examined will be those from the QTC samples with acicular filler particles added in various fractions to the composite mix, as defined earlier in table 3.1.

Acicular fillers are used as anti-static fillers in a number of applications where electrical charge build up in a material is not wanted. These types of fillers were added to QTC initially to try and reduce the build up of charge within the samples that could be recorded as white noise in the RF range. Analysis of the new QTC material was therefore required in order to quantify its electrical properties with the addition of acicular filler.

Initial experiments were undertaken in order to characterise and quantify the sample resistances as functions of applied compression. As with the pill samples this was to provide a guide as to the point where each sample became electrically conductive in terms of applied compression.

The addition of acicular filler particles to the composite has effect on the sensitivity of the QTC to compression as shown earlier in figure 3.4. Although the response of the samples bears the same overall characteristics of the pill samples the compression at which samples become conductive increases with acicular filler loading. Samples with no loading became conductive at less than 5% compression. With the addition of 2 g of acicular filler particles the sample needs to be compressed by nearly 20%. A 4 g loading of acicular filler particles sees this value increasing to 30%. This is emphasised by the compression ranges outlined earlier in figure 3.5. All the samples exhibit an exponential response to compression which indicates that the dominating conduction mechanism remains as Fowler-Nordheim tunnelling.

Current-Voltage Characteristics of Acicular Filler Loaded Samples

Current-voltage sweeps were carried out on Samples 4, 5 and 6 over the compression ranges given in figure 3.4. This enabled a wide range of start resistances to be considered.

There was less noise observed in samples containing acicular filler particles compared to those without. With standard QTC it was observed that on the down sweep that there are often spikes in the response which result in RF emissions causing white noise. These spikes occur as a result of sudden discharges of accumulated charge dissipating through the material. The distribution of these events will be entirely random as they are based on the random nature of the distribution of nickel particles through the composite and the capacities of each aggregate of charge accumulation. Figure 3.19 below shows an example of a high field sweep on a sample loaded with acicular filler particles. It can be seen that there are significantly fewer spikes in the up sweep of the cycle compared to standard QTC, shown in figure 3.11 earlier.

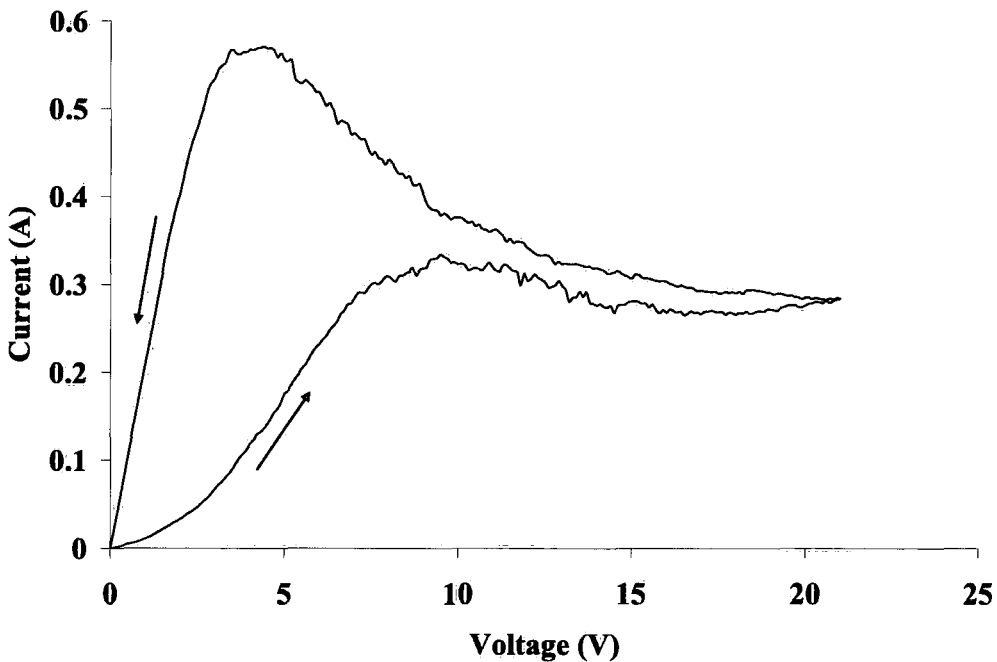


Figure 3.19: I-V characteristics at start resistances 100 Ω for a 4 g acicular filler loaded sample

Examination of these data sets also gives more information on the charge storage of the samples. In standard QTC (Figure 3.11) characteristically there are large peaks on the up sweep and on the down sweep. The response on the up sweep in figure 3.19 does not drop significantly after the peak (at 10 V). This is compared to the same characteristic seen in figure 3.11 (at 10 V) where the response falls almost back down to zero current. This relates to there being far less accumulated charge in the acicular loaded sample than the standard QTC caused by there being less pinching barriers formed in the acicular composite.

A proposed model to explain this behaviour is suggested below.

A summary of all the data for all three samples at varying start resistances is given in figure 3.20. The data is presented as the ratio of start to final resistance as a function of start resistance.

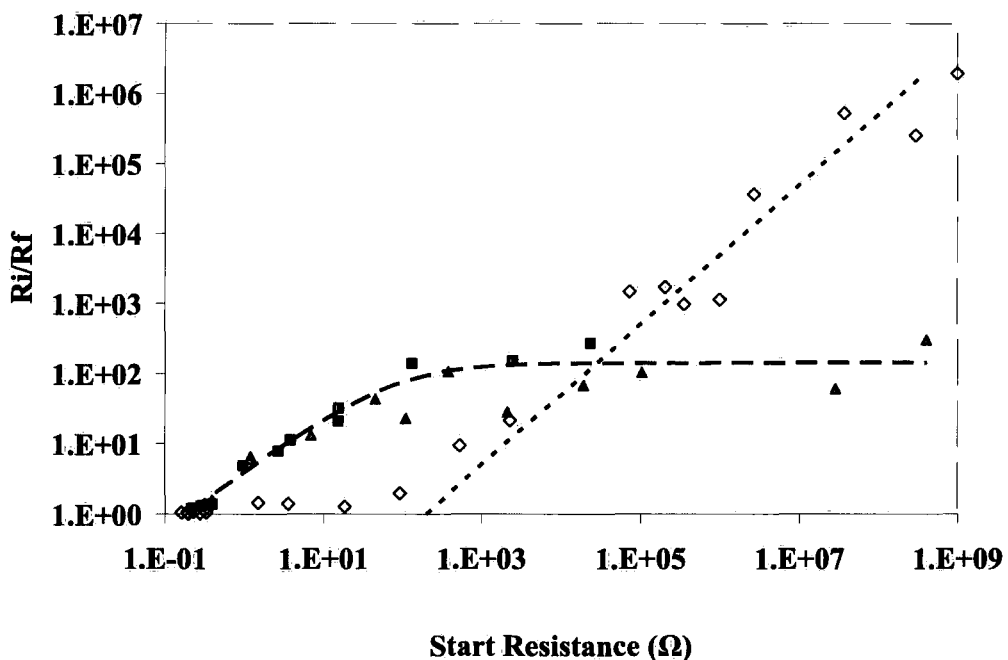


Figure 3.20: Ratios of initial to final resistances for all samples measured using low field sweeps, with: \diamond = Standard QTC, \blacksquare = 2g Acicular, \blacktriangle = 4g Acicular, QTC fit (dotted line) and acicular fit (dashed line).

The addition of acicular particles was seen to have a significant effect upon the charge storage characteristics of the QTC. The acicular particles can be seen in figure 3.21 and 3.22, SEM images of sample 6. It can be seen here that the acicular particles are not wetted in the way that the nickel particles are, shown by the high contrast in the SEM image that would not be present if they had an insulating layer around them, such as the effects seen on the nickel aggregates in the same image. This means they can act as additional conduction pathways between regions of charge. The acicular particles are Titanium Dioxide doped with Antimony, coated in a conductive Tin Dioxide layer making them a semiconductor material. Typical acicular particles are cylindrical with a 0.21 μm diameter and 2.86 μm in length.

The effect of the acicular particles is apparent in figure 3.20, comparing acicular loaded sample data to that of regular QTC. An explanation of the effects seen in the acicular loaded QTC can be given in terms of a modified version of the LNB model. The effects of the acicular filler are different depending on the amount of compression applied to the material. Looking first at the nickel aggregates that constitute the blobs in the model, distances between primary particles within aggregates are extremely small. Conduction within these regions is through simple quantum tunnelling through very small barriers that do not require any field assistance to reduce them. The addition of any acicular particles within these regions has no effect on the conduction and is not affected by any sample compression. The acicular particles simply act as part of the aggregate or blob.

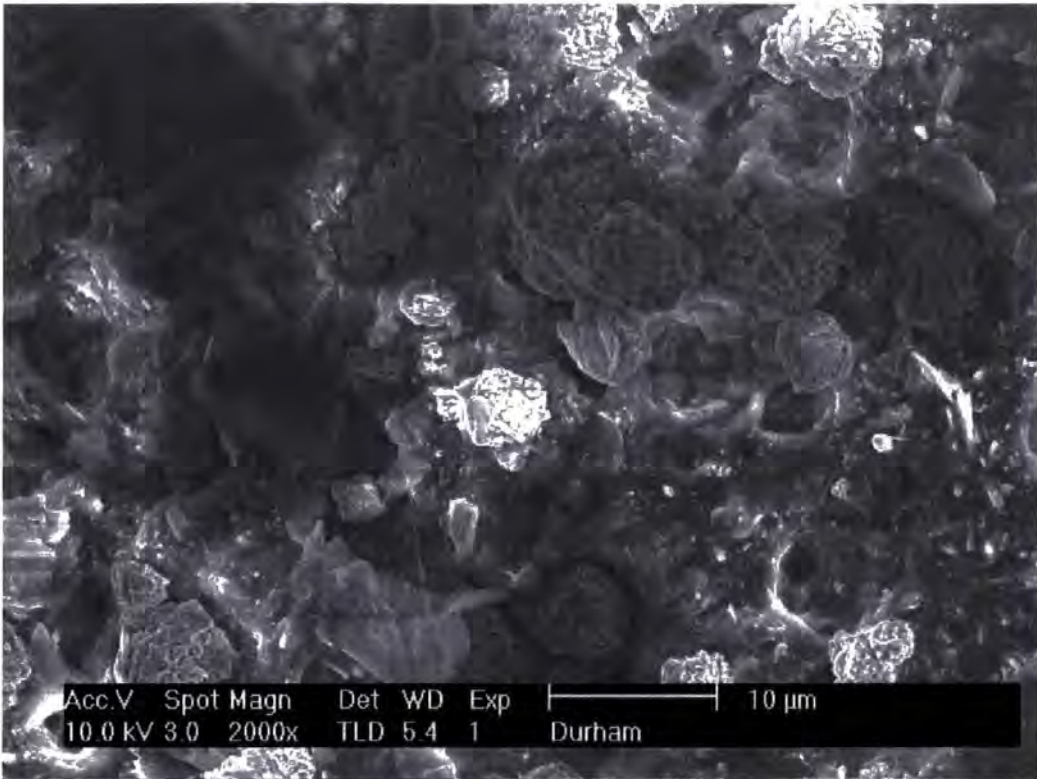


Figure 3.21: SEM image showing a cross section image of sample 6

The regions of most interest are the links connecting the Blobs. In standard QTC these are modelled as Fowler-Nordheim tunnelling pathways. However in the acicular loaded samples this is not always the case. Under compression the links between blobs become shortened, reducing the tunnelling distance and so increasing conductivity. At “high” compressions the average length of the links is shorter than the length of the acicular particles (approx. 2.68 microns). Thus any acicular particles that lie between blobs in this regime need to be orthogonal to the direction of the link between them, since this is the only orientation they may fit. The Fowler-Nordheim tunnelling will still occur, however the presence of the acicular particles will alter the current density slightly. This behaviour is illustrated in figure 3.20 between start resistances of 0.1 and 1000 Ω . In this region it is seen that there is a linear trend on the log-log scale for the acicular loaded QTC data set. The gradient of this trend is similar to that of the standard QTC. The offset and slight gradient difference between the two data sets is attributed to the effects of the acicular filler changing the intrinsic resistivity of the insulating material.

The acicular particles have the greatest effect when samples are in a low compression, low conductivity state. In this regime the average link length between blobs is greater than the range of the Fowler-Nordheim tunnelling. In this regime the material is not conductive. The blob separation in this case is now also large enough to allow acicular particles to align across the gaps between them, providing a conduction pathway where previously there was none. The random statistical nature of the dispersion of particles within QTC dictates the amount of acicular particles that align this way making it a statistical arrangement. This provides discharge pathways for charge leakage from trapping sites. This effectively reduces the amount of charge that can be stored in the material as a significant portion of the previous charge storage regions now have a discharge pathway. This effect is seen in figure 3.20 for start resistances above 1000Ω , in the low compression region, where the differential resistance flattens out. This is in contrast to standard QTC where the amount of charge storage continues to rise with increased start resistance. In this regime the effects of acicular filler on charge pathways between blobs has a much greater effect than the small effects it has on space charge within the insulator, underlined by the significant effects seen in figure 3.20 above 1000Ω compared to the SCLC effects below this start resistance. This is to be expected as the conduction through space charge limited currents is far less effective than that of the Fowler-Nordheim conduction mechanism.

An additional point to reiterate is the overall heterogeneous structure of the aggregate filler network. Within any one sample there will be a range of link lengths and blob sizes randomly distributed throughout. Therefore the results seen in figure 3.20 are a statistical average of the individual regimes present. In the high compression region there will be mainly very short link lengths and little acicular filler effect, however some regions of the composite will still exhibit longer link lengths that are affected by the acicular filler. Conversely in low compression samples there may still be regions with a high density of short links effectively reducing the effects of the acicular filler. The effect of this heterogeneous dispersion of particles and link lengths is highlighted in figure 3.20 by the gradual change in trend shown about the 1000Ω start resistance region.

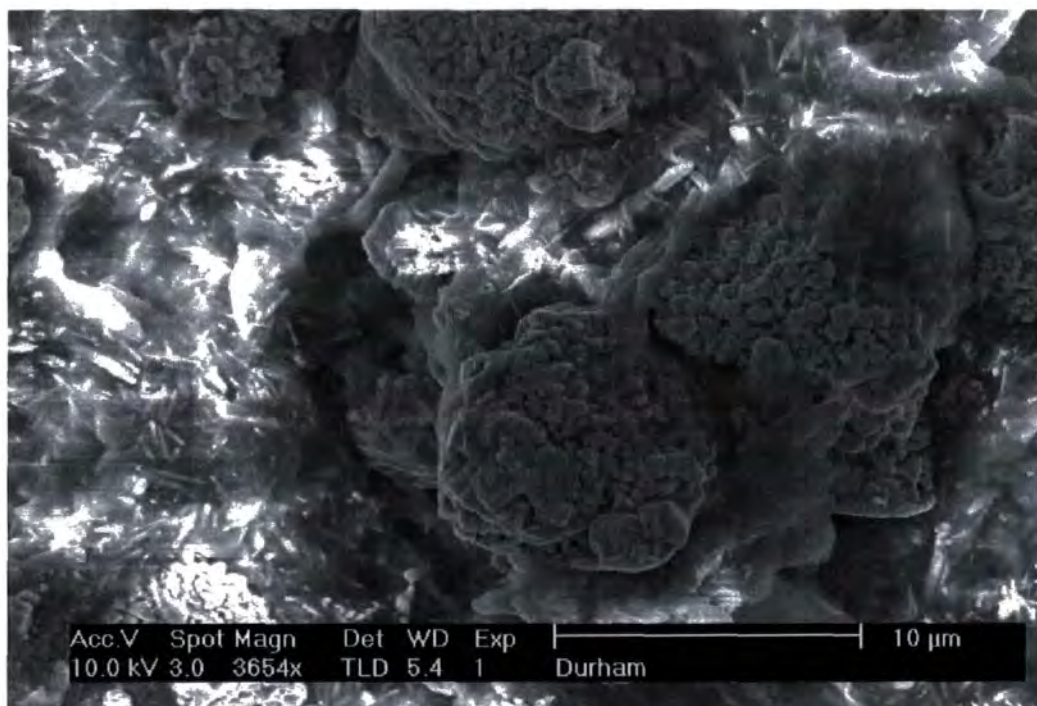


Figure 3.22: SEM image of acicular loaded QTC

Figure 3.22 shows a SEM image of an acicular loaded QTC sample. Within this image it is possible to see regions of blobs with links that are both long and short with acicular particles arranged orthogonally (top right of figure 3.22) and in line with links (top left of figure 3.22), emphasising the heterogeneous nature of the structure.

3.6 Conclusions

QTC exhibits a number of unique and unusual electrical properties. QTC can generally be described as a heterogeneous material constructed of two phases, polymer insulator and conductive nickel aggregates. A Links-Nodes-Blobs model can be applied to describe the system with links being made up of Fowler-Nordheim tunnelling pathways, the blobs being made up of aggregates of nickel particles. This model allows for the heterogeneous nature of QTC, which is responsible for the sample to sample variation encountered, along with the extremely sensitive electrical response to applied pressure.

Fowler-Nordheim tunnelling is a type of field assisted tunnelling that accounts for the electron tunnelling over relatively large barrier lengths required in QTC. This is not a phenomenon that would be possible through simple quantum tunnelling. The spiky surface nature of the nickel particles allows for high field densities (between 10-1000 KVcm⁻¹) to be present in the tips of the spikes. This leads to localised electric field enhancement which in turn produces field assisted tunnelling in the form of Fowler-Nordheim tunnelling.

A “pinching” model is proposed that describes macroscopically the electronic characteristics of QTC as exhibited in the current-voltage data. This occurs when charge becomes trapped in dead-end pathways up to a point where they begin to act as potential barriers to nearby pathways pinching them off. A feedback mechanism is setup and overall conduction through the sample is reduced. The description is analogous to SCLC behaviour. The rate of charge leakage from the samples is less than that of charging, resulting in charge storage within the sample, highlighted by a hysteresis in the current response. The large accumulations of charge promote further charge injection into the surrounding insulator. Defects and impurities in the polymer matrix provide trapping sites and charge is accumulated in these regions. In addition charge is also trapped in some of the remaining dead-end path ways and pinched off regions where charge has not leaked away. The overall effect is that a negative-differential resistance is observed between start and end resistances of a sample

upon current-voltage sweeps. This is highlighted further when subsequent repeat sweeps are conducted.

Noise in the current-voltage sweeps is observed and attributed to sudden cascades of charge as local trapping potentials are exceeded or overcome. Spark discharging and oscillatory decays from resonating charges caused in these events produce RF emissions, often detected as white noise. The random distribution of particles through the material accounts for the distribution of voltages at which these emissions occur.

In high compression regimes Joule heating is seen to have an effect on the QTC material. Large currents passing through the samples dissipate power producing heat; a model fit was applied and matched the data well confirming the observations.

The addition of acicular filler particles shows significant effects on the electrical characteristics of the composite. Higher loading densities of the acicular particles produce samples that are subsequently less sensitive. Current-voltage characteristics show that the filler particles affect the charge storage capabilities of the material. Under high compressions the orthogonal orientation of the filler particles has little effect upon the electrical characteristics. However at lower compressions acicular particles can align across gaps between regions of trapped charge allowing it to discharge and therefore reducing overall charge storage in the material. SEM images of QTC were presented providing additional evidence of these findings.

Chapter 4, Models and Theory of Vapour Absorption

Introduction

The second section of this PhD reports on the development of QTC as a chemical vapour sensor. Investigation will continue from previous work by Hands and Williams [12].

Previous work was conducted using compressed QTC granules to detect volatile organic compound (VOC) chemical vapours. Granules were compressed to produce a conductive regime, before the vapour was then forced through the granules at a known flow rate. It was found that upon exposure to the vapour the QTC granules swell causing a detectable increase in resistance. This change was seen to be large, over orders of magnitude, with response times of under a minute.

In order to create these early vapour sensors an alternative version of QTC was developed, granular QTC. This was achieved by using a 10:1 loading ratio (wt) of nickel to Silastic T4 as described earlier and in the patent [10]. The granules are large nickel aggregates coated by a polymer layer. It was found that the granular QTC displayed the same general electrical properties under deformation within the sensor rig as bulk QTC. Investigation of individual granule response characteristics is an area of potential future research. It is possible to manufacture QTC granules using different polymer binders including; polyurethane and polybutadiene [12].

The vapour sensors developed using compressed granules showed large, fast response to a range of organic vapours over a wide range of vapour concentrations. However the design of the experimental setup meant that repeatability of sample conditions was poor. Obtaining the same starting resistance and sample regime was difficult, with the granular QTC awkward to work with.

The aim of this PhD was to take the successful aspects from the early work and develop a QTC vapour sensor that was not only a good detector, but more repeatable and easier to use. It was based on these requirements that a new type of QTC was developed; intrinsically conductive QTC. This new QTC was still based on QTC granules. However to make it conductive the granules were not physically compressed. Instead they were mixed with a polymer solvent solution. This solution was deposited onto copper electrodes and left to cure. Upon curing the host (binding) polymer contracted around the QTC granules applying a compressive force putting the sample into a conductive regime. In this arrangement the granules themselves must be in contact providing a continuous electrical contact through the material. In effect there must be a percolative network of QTC granules across the sample held in place by binding polymer.

The remainder of this thesis will report on the production and development of intrinsically conductive QTC. Effects of the sample compositions in terms of both relative mixing ratios and the polymer types used will be explained. Response characteristics to different environmental changes such as temperature and solvent concentration exposures will be discussed.

This chapter will outline a number of relevant theories concerned with vapour absorption and diffusion through polymer materials.

4.1 Vapour Sensing Technologies

Before beginning a report on the application of QTC to vapour sensing it is prudent to first discuss other vapour sensing technologies already in use, both in industry and in academic studies.

There are available intrinsically conductive polymers, [46-48], that swell under exposure to VOC vapour causing resistance change. Other polymer types may exhibit a change in their polymer chain as a response to the vapour, thus causing changes in the charge carrier mobility within the material and so changing conductivity [49]. Polymer based sensors have the advantages that they respond fast and are recoverable. They can be made of different chemicals allowing them to respond in turn to a range of different vapours. In addition to this they are relatively cheap and easy to manufacture. Their main disadvantages are that they are susceptible to baseline drift if temperature and humidity changes. In addition to this they display instability in terms of oxidation and reduction which can cause samples to significantly degrade.

An alternative to using intrinsically conductive polymers is the use of filler-polymer composites. Swelling within the polymer due to vapour absorption is detectable through resistance changes in the conductive filler network. The most commonly used filler is carbon black, with a large amount of literature covering their development [50-53]. These sensors work based on filler loading densities being such that the material just exceeds its percolation threshold. Any swelling in the material then causes the filler density to fall below the percolation threshold, producing a large electrical response. Electrical response through swelling is often found to be proportional to vapour concentration [54], leading to the ability to gain quantitative information on the vapour. Furthermore it is also found that different vapour types can invoke different degrees of swelling in different sensor types. This too adds to the potential to gain quantitative data. As with intrinsically conductive polymers, these filler-polymer composites also show susceptibility to temperature and humidity changes. It is this bracket of vapour sensor that the QTC vapour sensors fall. However the addition of the

exponential electronic response to swelling is hoped to give QTC an advantage over conventional composite sensors.

There are sensors available that detect mass uptake of a surface layer that absorbs an exposed vapour [55-57]. Most commonly these are based upon a quartz crystal substrate with a vapour sensitive layer across their surface. Upon exposure to a test vapour the polymer absorbs the vapour molecules and increases in mass. These are referred to as Quartz Crystal Microbalances (QCM). This increase in mass changes the resonant frequency of the quartz crystal substrate. Measurement of this resonant frequency can be related directly to the mass uptake of the polymer layer. The type of polymer used for the surface layer can be changed to match with specific vapour types; gaining the advantage of polymer selection, fast response and recovery, but without the effects of temperature and humidity sensitivity.

A vapour sensor setup that also utilises a polymer layer as the vapour interface is the dual-slab waveguide vapour sensor [58-59]. In this setup the polymer layer provides the top layer of a multi-layer waveguide setup, figure 4.1.

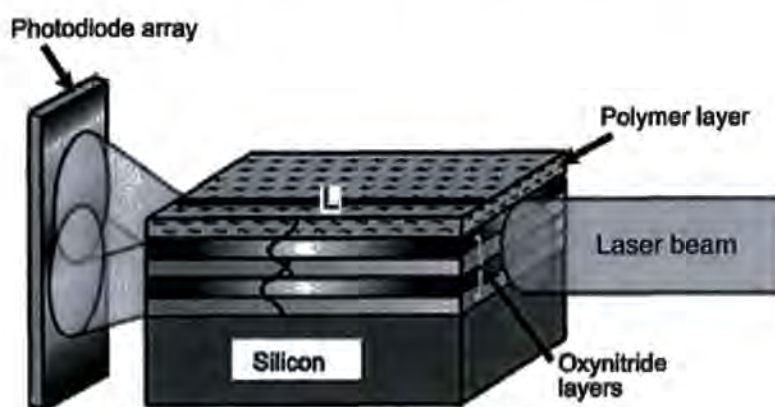


Figure 4.1: Dual slab waveguide interferometer

The waveguide is end lit with laser light. The layered structure of the slab waveguide is designed to allow two waveguide paths through it. The lower path acts as a reference with the top pathway incorporating the polymer surface layer. Two resultant beams exit the other end of the waveguide and an interference

pattern is observed. Changes in polymer density through vapour absorption and swelling lead to a change in refractive index of the upper wave path. This in return changes the interference pattern seen at the end of the waveguide and detected using a photodiode array. Changes in the interference pattern can therefore be used to detect vapours incident on the upper polymer layer.

Gas and vapour sensors are also available that utilise electrochemical interaction of gas and vapour molecules with metal-oxide semiconductors [60-64]. The semiconductor surface may receive or donate electrons from the vacant orbitals within the semiconductor or the adsorbed molecule. The transfer of charge that occurs can then be detected as a small current change within the semiconductor. These types of sensor show sensitivity down to 0.1 ppm, however their response and recovery times are much larger than those exhibited by polymer based sensors and are required to have a high operating temperature of hundreds of degrees Celsius.

The most accurate form of vapour detection is the use of mass spectrometry [65]. The analyte vapour molecules are ionised and then fired through a curved path using electric and magnetic fields. Analysis of the effects upon these fields as the molecules pass through them leads to information regarding the charge to mass ratio of the molecule, thus allowing accurate identification of the molecule. Although very accurate, this method is also very expensive making it unsuitable for many applications.

Gas and vapour sensors, such as those described above, can be designed to target a single, specific chemical species. This is often referred to as the “lock and key” method. In order to detect a wider range of analytes using this approach, a separate sensor element is required for each analyte. The majority of sensor elements therefore remain unused until its target chemical is detected.

This “lock and key” approach to sensing can be therefore be improved by constructing an array of sensors, each of which responds to a different, but wide variety of analyte types. Complex aromas are then introduced to the sensor array, whilst the response to all sensor elements is monitored simultaneously.

An odour map can be generated from the pattern of responses and pattern recognition software used to compare the results to a library of pre-programmed aroma responses. This system is the basis of an artificial olfactory system or an electronic nose [66]. In addition to pattern recognition, techniques such as principle component analysis (PCA) can be used to help classify and distinguish aromas, based upon the combination of responses obtained from the sensor array. The capabilities of an electronic nose are determined by its ability to respond to a wide range of specific analytes to a degree that make them distinguishable. Performance of electronic noses can be further improved by the introduction of analysis of the temporal response of the sensors to analyte exposure [67]. For further review on electronic nose systems the author directs the reader to the following references [67-70, 49].

4.2 Thermodynamics of Absorption

In a mixture comprising multiple components, the Gibbs Free Energy (G) is a thermodynamic potential associated with the work obtainable from an isothermal isobaric system. The free energy of a chemical reaction occurring in such a system (ΔG) can be defined as;

$$\Delta G = \Delta H - T(\Delta S) \quad \text{Eqn 4.1}$$

Where ΔH is the change in enthalpy, also known as the heat of mixing, ΔS is the change in entropy of the system and T is the absolute temperature of the system.

ΔH is generally obtained experimentally and is a measure of the energy released or absorbed in a reaction. The reaction can be endothermic ($+\Delta H$) or exothermic ($-\Delta H$), either aiding or opposing the mixing of a solvent and polymer respectively in this case. Enthalpy changes in a polymer solvent mixture are dominated by chemisorption and physisorption processes that are endothermic in nature. Thus ΔH values in the systems discussed in this thesis are positive.

For a mixture to form from multiple components the change in its free energy must be negative. In order for this to occur with a positive ΔH value, ΔS must be large and positive.

The change in entropy that occurs when a polymer and a solvent are mixed together consists of two processes. Firstly there is an increase in entropy as the two components mix, caused by an increase in the systems disorder. The physical process that controls this is known as diffusion and is discussed in detail in later sections.

The second process occurring is the swelling of the polymer matrix. Vapour molecules absorbed into the polymer cause it to dilate. This reduces the number of possible orientations the polymer chains can take and causes extension of the

chains. The polymer chains stretch and orientate to give less entangled states which results in a more ordered system and so a reduction in entropy is seen.

An overall increase in entropy is required for the reaction to occur and ensure ΔG is negative; therefore the swelling process must be overcome by the mixing process to allow more solvent to be absorbed.

4.3 Fickian Diffusion

Diffusion is the physical process that controls the rate at which a solvent mixes into a polymer. Entropy increases as the overall disorder of the system increases.

In order to create an initial simple model of the diffusion some basic assumptions are first made. There is assumed to be no swelling and no chemical interactions in the material as the vapour mixes with the polymer, these would have an effect on the entropy as described in the previous section. These assumptions mean that the change in enthalpy is zero and the only contribution to entropy change is the disorder created by the mixing of the two substances. As a result the polymer neither attracts nor repels the solvent molecules and the rate at which the solvent penetrates the polymer is controlled by the concentration gradient dn/dx , where n is the number of vapour particles and x is unit area. This relation is known as Fick's First Law of Diffusion and is given by equation 4.2.

$$F = -D \frac{dn}{dx} \quad \text{Eqn 4.2}$$

Where F is the number of particles crossing per unit area per unit time (the flux) and D is the diffusion coefficient. The diffusion coefficient is dependent on several factors. These include the porosity of the polymer [71], the average pore size and the pore density.

Equation 4.2 is limited in its application however due to the assumptions made in its derivation. Furthermore it also requires a constant concentration gradient which is unlikely. A finite sample with limited free volume will not show this behaviour requiring a time-dependent version of equation 4.2. Through conservation of matter within the system combined with equation 4.2 Fick's second law can be given as:

$$\frac{dC}{dt} = D \nabla^2 C \quad \text{Eqn 4.3}$$

C is the concentration of the solvent in the polymer and is equal to the volume of the solvent divided by the dry volume of the polymer.

A simple one dimensional solution to equation 4.3 is given in equation 4.3b, with a boundary at $x = 0$ with concentration maintained at $C(0)$.

$$C(x,t) = C(0)erfc\left(\frac{x}{\sqrt{4Dt}}\right) \quad \text{Eqn 4.3b}$$

Where *erfc* is the complementary error function, the length $\sqrt{4Dt}$ is called the diffusion length and provides a measure of how far the density has propagated in the x -direction by diffusion in time t and D is the diffusion constant. The implication from this is that the quantity of solvent sorbed into the polymer increases linearly with the square root of time, this is known as Fickian Diffusion.

4.4 The Flory-Huggins Parameter

Returning back to energy considerations, the entropy of mixing (ΔS_m) of vapour molecules into the polymer is described by the Flory-Huggins theory [72].

$$\Delta S_m = k_b \ln \Omega = -k_b (N_s \ln \phi_s + N_p \ln \phi_p) \quad \text{Eqn 4.4}$$

Ω is the total number of spatial arrangements of the solvent molecules within the polymer, the degeneracy, and k_b is the Boltzmann constant. This can be expressed in terms of the volume fractions of the polymer, ϕ_p and the solvent, ϕ_s (where $\phi_p = 1 - \phi_s$) and the number of polymer and solvent molecules are N_p and N_s respectively. Now assuming that this ΔS_m represents the total entropy change of mixing, the free energy of mixing can be described by substituting equation 4.4 into equation 4.1 mentioned earlier and expressing the enthalpy in similar terms of volume fractions and moles;

$$\Delta G_m = RT(n_s \ln \phi_s + n_p \ln \phi_p + \chi_{sp} n_s \phi_p) \quad \text{Eqn 4.5}$$

R is the gas constant and has been used in conjunction with Avogadro's number ($R = k_b N_A$) to change from number of molecules to moles (n_s and n_p). T is the absolute temperature and χ_{sp} is a dimensionless quantity that characterises the interaction energy per solvent molecule and is referred to as the Flory-Huggins parameter, a full derivation of equations 4.4 and 4.5 is given in Appendix G.

$RT \chi_{sp}$ represents the difference in energy of a solvent molecule immersed in the pure polymer compared to one surrounded by its own type of solvent molecule, i.e. immersed in pure solvent. The Flory-Huggins χ interaction parameter for polymer-solvent pairs plays a dominant role in explaining critical phase behaviour of compatible pairs. The value of χ provides an indication to explain the solvents ability to penetrate a certain polymer. A penetrant is described as a good solvent for $\chi = 0$, a non-solvent for $\chi > 1$ and borderline when $\chi = 1$.

The value of the parameter can be estimated using the Hildebrand solubility parameters δ_s and δ_p (discussed in the next section) where V_{seg} is the actual volume of a polymer segment.

$$\chi = \frac{V_{seg}(\delta_s - \delta_b)^2}{RT} \quad \text{Eqn 4.6}$$

4.5 Solubility Parameters

The Hildebrand solubility parameter is one of the most widely used of the theories for solubility matching. Variations of the general theory include the Hildebrand number, hydrogen bonding value, Hansen parameter, and fractional parameter [73]. These systems relate to non-ionic liquid interactions that also include polymer interactions, water based systems and systems incorporating acid-base reactions that cannot be evaluated using simple solubility parameters alone.

For a solution to occur the solvent molecules must overcome inter-molecular forces in the solute and the solvent molecules themselves must be separated by the solute. This happens more readily when the inter-molecular forces between both components are similar. If the forces are sufficiently different, the strongly attracted molecules will bond together, excluding the weakly attracted molecules, resulting in immiscibility.

The inter-molecular forces in question are van der Waals forces. These are a product of intermolecular polarities. Accurate predictions of solubility behaviour depend not only on determining the result of intermolecular attractions between molecules, but in discriminating between different types of polarities as well. A single molecule, due to its structure, may exhibit van der Waals forces that are the combined result of two or three different kinds of polar contributions. Substances will dissolve in each other not only if their intermolecular forces are similar, but more so if their composite forces are similar. Types of component interactions include hydrogen bonds, orientation effects, and dispersion forces.

It is the total van der Waals force that is used in the Hildebrand solubility parameter. The solubility parameter is a numerical value that indicates the relative solvency behaviour of a specific solvent. It is derived from the cohesive energy density of the solvent, which in turn is derived from the heat of vaporization, the energy required to vaporize a liquid

From the heat of vaporization, in calories per cubic centimetre of liquid, the cohesive energy density can be calculated using equation 4.6

$$C = \frac{\Delta H - RT}{V_m} \quad \text{Eqn 4.6}$$

C is the cohesive energy density, ΔH the heat of vaporization, R the gas constant, T the absolute temperature and V_m the Molar volume.

The cohesive energy density of a liquid is a direct reflection of the degree of van der Waals forces holding the molecules of the liquid together. The correlation between vaporization and van der Waals forces also matches a correlation between vaporization and solubility behaviour. This is because the same intermolecular forces have to be overcome to vaporize a liquid as to dissolve it.

In 1936 Joel H. Hildebrand [74], proposed the square root of the cohesive energy density as a numerical value indicating the solvency behaviour of a specific solvent.

$$\delta = \sqrt{C} = \sqrt{\frac{\Delta H - RT}{V_m}} \quad \text{Eqn 4.7}$$

The value δ in equation 4.7 is referred to as the Solubility Parameter.

Solubility parameters can be used to determine the solubility of polymers and solvent pairs. The following relationship can be used to estimate how compatible a polymer-solvent pair is. If the square root of the value of the solubility parameter of the solvent, δ_s , minus the solubility parameter of the polymer, δ_p , is less than 1, then the solvent will most likely dissolve the polymer [75]. This is summarised in equation 4.8.

$$\sqrt{(\delta_s - \delta_p)} \leq 1 \quad \text{Eqn 4.8}$$

4.6 Case-II Diffusion

When a polymer is exposed to an organic solvent vapour (penetrant) the weight of the polymer increases linearly with time, provided that the vapour pressure of the penetrant is sufficiently high [76].

An optical microscope can be used to analyse the polymer during exposure and monitor the progress of penetrant as it absorbs into the polymer [77]. This analysis indicates the presence of a front ahead of which the concentration drops off sharply. Behind this front the concentration gradient of the penetrant is negligible. The formation of the front is preceded by an induction period during which the penetrant concentration is seen to be a smoothly decreasing function of distance from the polymer surface. This precursor is a linear diffusion profile described by Fickian diffusion theory [78]. Immediately after the induction time a sharp front is formed that advances at constant speed. The concentration of the penetrant behind the front increases with time until its equilibrium concentration value is reached. For sufficiently low partial pressure of penetrant outside of the polymer surface, front formation is inhibited.

Case-II diffusion can be divided into two stages, the initiation stage where penetrant concentration builds close to the surface and front formation occurs and a stage where the concentration front propagates linearly.

The Thomas and Windle (TW) model [79] can be used to predict Case-II Diffusion. This model suggests that the diffusion process is strongly associated to the mechanical response of the polymer. Stating that the rate of penetrant absorption must be comparable to the swelling rate controlled by the creep deformation of the surrounding polymer. The creep deformation is subsequently dependant on both the osmotic pressure driving the swelling and the viscoelasticity of the polymer. The viscoelasticity and diffusivity of the polymer are very sensitive to the concentration of the penetrant ϕ , in the model this is assumed to depend only on one spatial dimension, $\phi = \phi(x,t)$. Large decreases in viscoelasticity and large increases in diffusivity are seen over just a

small change of penetrant concentration. These changes are caused by plasticization of the polymer upon sorption of the penetrant. The penetrant causes a decrease in polymer relaxation times, ranging from long times associated with glassy behaviour, to short times associated to rubbery behaviour. The penetrant occupies regions of space between polymer chains. For a polymer in the glassy state the polymer chains are in a random close-packed arrangement and so there is little free volume. Thus if the concentration, or volume fraction, of penetrant is greater than the volume fraction of free volume then there is a resistance of the polymer to sorption and relaxation times are longer, the polymer chains have limited space to move apart. If the polymer is above its glass transition temperature and rubbery in nature, the chains can readily move apart by processes involving rotation of the main chains and so concentration equilibrium is obtained very quickly.

The initial penetrant concentration ϕ will be less than the equilibrium concentration ϕ_c and will approach it as permitted by the motion of the polymer chains. It is the difference between the actual concentration and the equilibrium concentration that creates the osmotic pressure that acts upon the penetrant molecules. This osmotic pressure is resisted by the stress exerted by the glassy polymer chains. As bond rotation and motion of the polymer chains begins to occur the stress is reduced. This creates new regions of free volume and so sites for penetrant molecules to occupy. This results in an increase in penetrant concentration within the polymer and so a reduction in osmotic pressure.

It is this strong dependence of viscoelasticity and diffusivity on penetrant concentration that produces the characteristic Case-II diffusion, i.e. the propagation of a sharp concentration front.

The TW model describes the rate of change of volume fraction, or swelling, as the rate of linear viscous creep deformation driven by the osmotic pressure P . In the case of an infinitesimally thin polymer film extending to infinity in the y and z directions, remembering that penetrant only acts in the x -direction, equation 4.9 describes the rate.

$$\frac{\partial \phi}{\partial t} = \frac{P}{\eta} \quad \text{Eqn 4.9}$$

Where η is the viscosity of the polymer and P is the osmotic pressure driving the swelling that is calculated using equation 4.10.

$$P = (1/\Omega)(\mu_e - \mu) \quad \text{Eqn 4.10}$$

Where μ is the chemical potential of the penetrant, μ_e is the local equivalent potential at equilibrium, i.e. $\mu = \mu_e$ when $P = 0$ and Ω is the partial molecular volume (concentration) of the penetrant. At low penetrant concentration values the chemical potentials can be calculated using equation 4.11.

$$\mu = k_b T \ln(\gamma \phi) \quad \text{Eqn 4.11}$$

Where k_b is Boltzmann's constant, T the absolute temperature and γ is an activity constant that is independent of penetrant concentration [80].

Substituting 4.11 into 4.10 the osmotic pressure can be written in terms of the penetrant ϕ and equilibrium ϕ_e concentrations, equation 4.12.

$$P = (k_b T / \Omega) \ln(\phi_e / \phi) \quad \text{Eqn 4.12}$$

The viscosity of the polymer is assumed to decrease exponentially with increasing penetrant concentration, described by equation 4.13.

$$\eta = \eta_0 \exp(-m\phi) \quad \text{Eqn 4.13}$$

Where η_0 is the viscosity of un-swollen polymer and m is a material constant. The strong dependence of viscosity on penetrant concentration models the plasticizing effect of the penetrant on the polymer. Now combining the equations for viscosity and osmotic pressure, equations 4.13 and 4.12 respectively, with equation 4.9 an overall equation for the swelling rate can be formed, equation 4.14.

$$\frac{\partial \phi}{\partial t} = B \exp(m\phi) \ln\left(\frac{\phi_e}{\phi}\right) \quad \text{Eqn 4.14}$$

This equation is the basis of the TW model where B represents $k_b T / \eta_0 \Omega$. It is possible to then model the swelling rates using different values of m based upon the polymer being used. Numerical integrations can be used to evaluate this equation and model the swelling rate for different polymers.

The key features of Case-II diffusion are as follows:

- i) Sharp Diffusion Front
- ii) Linear Weight Gain with time
- iii) No concentration gradient behind the front.

For examples of TW modelling of Case-II diffusion and further discussion of this model the author recommends literature published by Hui [81-82] and also other works by various authors [83-85].

Chapter 5, QTC Vapour Sensors

Introduction

The second sets of experiments undertaken in this PhD were to develop and characterize QTC as a chemical vapour sensor. Following the completion of some preliminary experiments to identify areas requiring most development, detailed experiments are presented that first of all develop the physical parameters of the sensors, followed by a further set that help develop the composition of the vapour sensors. Finally a range of experiments are presented that test the sample response to differing environmental changes.

5.1 Experimental Setup

The main vapour sensing kit used to expose the QTC samples to solvent vapours was developed from the existing equipment used previously by Hands [12]. It was designed and built in house at Durham University.



Figure 5.1: Five sample chambers with vapour lines connected

It consists of five sample chambers, shown assembled with sample holders mounted in figure 5.1. Each chamber is a hollowed T-shape with push fit

attachments top and bottom to allow easy gas flow through the length of them, with a side section of the T-shaped chamber flanged to allow samples on specially made holders to be easily mounted into the gas flow, figure 5.2.



Figure 5.2: Sample mounted onto holder with wires connection to electrodes, ready to fit into a T-shaped holder

Samples were prepared and dropped onto acrylic boards 5 mm x 20 mm in size using a positive displacement dropper accurate to 0.05 μl . The sample boards had conductive electrodes printed onto their upper surface to allow electrical current to be easily passed through the samples, figure 5.3. The electrodes are connected via wires fed out through the sample holders to a Keithley 2740 Multimeter. This monitors all five sample resistances over a range of micro ohms to mega ohms at a sampling rate of one reading per second. This data is recorded by a LabView program on a PC that is connected to the Keithley multimeter via a GPIB interface card. Thermistors monitoring the external and internal temperatures of the sample chambers were also connected to the Keithley multimeter and logged by the LabView program. The five sample chambers are housed in an incubator maintaining a constant temperature of 20°C to eliminate environmental temperature effects.

The sample chambers have an in and out gas flow connection as described. Each out gas line simply passes to an exhaust line that vents to atmosphere. The line into the sample chambers is connected to a five way splitter that divides inward flow from one common line evenly to each chamber.



Figure 5.3: Sample boards and positive displacement dropper, insert shows electrode.

The common input line is then connected to a series of equipment allowing control of flow rates and exposures to test vapours. This setup is shown schematically in figure 5.4 and described in detail as follows.

Two lines of nitrogen carrier gas were supplied to the lab via a common boil off source. These provided two sources of nitrogen at around 2 bar pressure to two master valves. The two lines were filtered by two 10 micron in line filters just after the master valves. This prevented any unwanted contaminants entering the system.

One of the main lines was dedicated to sample purging. An inline mass-flow controller (MFC) was placed on the line and purge flow was maintained at 3 litres per minute. This line was maintained separate to the rest of the system in order to prevent any contamination by solvent vapours.

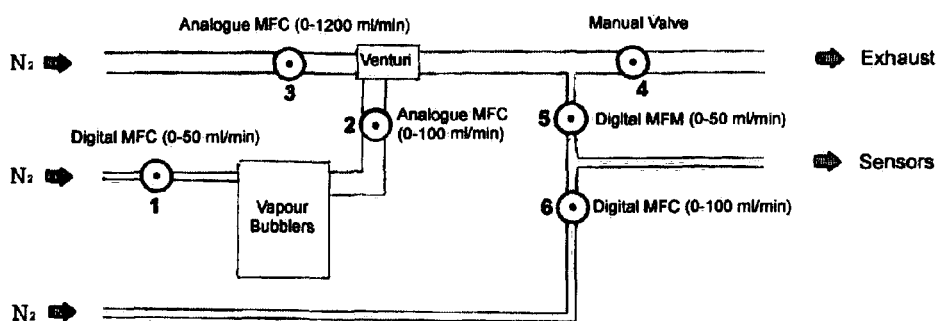
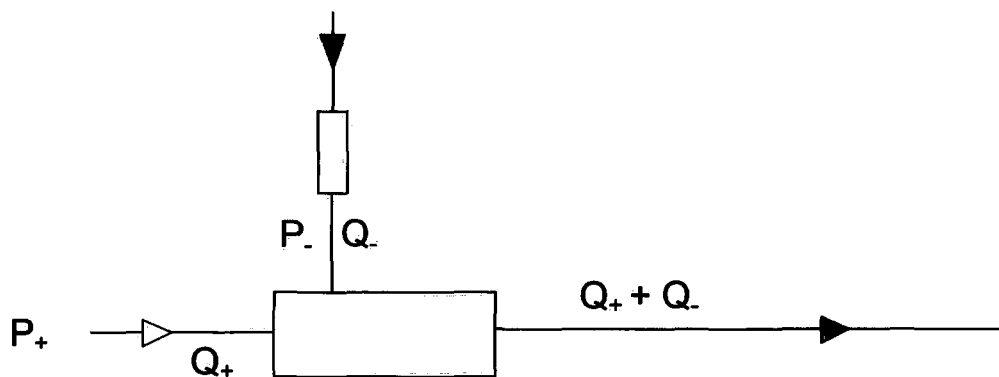


Figure 5.4: Schematic of dilution section of vapour kit

The second master line was split into three as shown in figure 5.4. The first line connects to an analogue MFC maintaining a constant flow rate of 1200 ml/min to a venturi mixing valve. This allows a very large dilution of solvent vapour by nitrogen to take place. Normally a junction between two vastly different flow rates will result in a back pressure and flow restrictions in the lower flow line. The venturi operates by passing a large flow over a laser cut orifice within an enclosed chamber. The low pressure created by the fast moving flow draws vapour up into the main flow from the third orifice, figure 5.5. The size of the laser cut orifice dictates the mixing ratio between the main flow line and the secondary flow, the mixing ratio of the venturi used in this experiment was set at 1200:30 ml/min.



P = Pressure
Q = Flow rate

Figure 5.5: Schematic of venturi flow and pressure directions

The second flow line was controlled by a Cole-Palmer digital mass-flow controller accurate in the range of 0 to 50 ml/min to 0.1 ml/min. Remote control of this and the other digital MFCs were possible through the same LabView program using a digital to analogue card in the PC. The nitrogen line connects from the digital MFC through to two gas bubbler chambers in series, figure 5.6. These contain the test solvent in liquid form. Nitrogen gas is flowed through the bubblers; two are used to ensure that the nitrogen carrier gas is fully saturated as it flows through the solvent liquid. The chambers were designed specifically for the experiment and incorporated narrow necks to reduce the possibility of liquid escaping the chamber through splashing. Additional liquid trap flasks were placed in line before and after the bubblers to prevent any liquid escape in the event of a malfunction, the digital MFCs are susceptible to damage if liquid solvent passes through them.



Figure 5.6: A bubbler chamber and additional liquid trap

The concentration of the vapour solvent can be controlled accurately through variation of the temperature of the solvent bubblers. Correlation between solvent temperature and vapour pressure are described in detail in Appendix E. From this correlation it is possible to calculate the relative concentration of solvent vapour. The solvent temperature was controlled using a Grant LTC20-40RS oil bath. This was a low temperature circulator with a 20 litre capacity and a temperature range from -40°C to 100°C . The bath was filled with Baysilone M3 silicone fluid, which acted as a heat transfer system. The solvent temperature was controlled by immersing the two bubblers into the oil bath.

The flow rate of the nitrogen through the bubblers was maintained at 30 ml/min. This was so the output flow from the bubblers matched the input flow drawn up by the venturi valve. The flow from the venturi out was then directed to a digital mass-flow meter (MFM). In order to control the flow through the MFM a manually controlled exhaust line between the MFM and the venturi was fitted. This provided two functions, controlling amount of flow to the sensors and also

preventing any backpressure to the venturi caused by more restrictive flow lines in the later parts of the equipment.

The third nitrogen line from the first master valve was connected to a second digital MFC. This was set at 50 ml/min matching the output from the MFM and venturi output. Thus a further 50:50 dilution of the vapour was achieved.

Overall in the above system vapour concentration can be controlled in three ways providing vapour concentration ranging from 20 ppm up to 100,000's ppm. Fine control of concentration is attained through temperature variation of the solvent in the bubblers. A higher range of concentrations can be attained by removing the venturi mixer from the system and taking the saturated solvent vapour directly from the bubblers. The push fit pipe work allowed easy interchange between dilution systems and bypass of the various parts. Table 5.1 summarises the concentration ranges available using combinations of the dilution setup for THF test vapour.

Temperature (°C)	Direct PPM	PPM using venturi at 30:1200	Additional 50:50 dilution
-40	4511	110	55
-30	9631	235	117
-20	19102	466	233
-10	35561	867	434
0	62660	1528	764
10	105239	2567	1283
20	169461	4133	2067
30	262911	6412	3206
35	323371	7887	3944
40	394654	9626	4813

Table 5.1: THF concentration values for various kit setups

Once the diluted vapour had been produced it was then channelled to a four-way 11500 series electronic solenoid rotary valve supplied by Omnifit. Also connected to an input on this valve is the purge line from the secondary master valve described earlier. This line purges the sample chambers with nitrogen gas flushing out any solvent vapour. Two valve positions were available, allowing

the sensor chambers to be exposed to the diluted solvent vapour flow or purged by nitrogen gas. Figure 5.7 shows the two solenoid valve positions schematically.

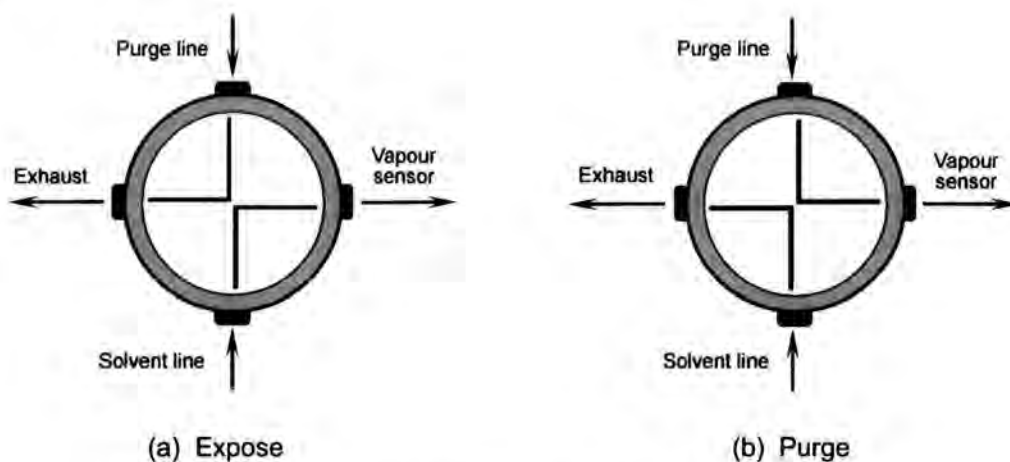


Figure 5.7: Schematic of electronic solenoid valve flow routes

The solenoid valve is controlled by the LabView program via digital I/O channel on the analogue/digital conversion card. This allowed automated controlled repeat exposures and sample purge for fixed time periods.

Teflon tubing was used throughout the experimental setup to prevent contamination of the solvents and degeneration of the lines.

5.2 Sample Manufacture and Preparation

Samples were prepared in house at Durham University using QTC granules produced and provided by Peratech.

Firstly polymer-solvent solutions were made by dissolving polymer pellets into a host solvent, loading quantities were measured by weight. Ratio of solvent to polymer was one of the quantities measured in later experiments. Details of the ratios used are given in the later sections describing specific experiments. A heated magnetic stirrer was used to mix the solutions at 40°C for 2 to 3 hours until the polymer was fully dissolved into the host solvent.

The solutions were then mixed by weight with QTC granules to create a final mixture. The granules were stirred into the solution by hand until they were fully mixed in. The ratios of granule to solution are a further quantity investigated later and experiment specific ratios are given in the experimental descriptions.

The mixtures were applied to an acrylic board with two conductive electrodes printed onto the surface. The electrodes were 5 mm x 25 mm in size with the QTC mixture applied so as to cover both electrodes. Application of the mixture was made using a positive displacement dropper, accurate to 0.05 micro-litres, figure 5.3. Samples were made using 10 micro-litres of solution, with the exception of the specific experiments conducted to investigate droplet size.

Having dispensed the required amount of sample mixture onto a sample board they were placed in an incubator at 20 °C and left for 12 hours to dry out. After this the samples were ready to be used for vapour testing.

5.3 Methodology

QTC vapour sensing experiments were all undertaken using the same underlying method. Samples were prepared using the process described earlier. They were then loaded into the vapour sensing rig and the electrodes from the samples connected to the Keithley Multi-meter. This in turn was connected to the LabView program.

The physical setup of the vapour dilution part of the kit was chosen depending on the required concentration range. For the preliminary experiments the venturi mixing valve was not available so solvent vapour concentration range was limited to temperature variation and direct final dilution with nitrogen through the second MFC. Upon choosing the required dilution regime gas flow was initiated and the system left for an hour to allow flow to smooth out and temperature of the sample chambers to equalise with the rest of the kit following the addition of new samples.

The LabView program through control of the solenoid valve then switched the gas flow to the sensors from purge to expose. After a pre-determined time, 1 minute for preliminary and early experiments and 5 minutes in later experiments, the solenoid switched the flow to the sample chambers back to purge. Purges for early experiments with 1 min exposures were for 10 min, the later 5 minute exposures corresponded to 5 minute exposures. The number of purges and exposures carried out was set to 10 for early experiments but then reduced to 5 for later experiments due to time constraints. This also maintained an experimental cycle of approximately 10 minutes for each exposure. The early experiments were conducted at relatively high concentrations of exposed solvent vapour, thus a short exposure time and longer purge time were used. Conversely in later experiments lower solvent concentrations were used and so longer exposure times were needed to ensure a full response was recorded. Subsequently less purging was required due to less solvent being absorbed.

Data from each of the five chambers was recorded by the LabView program and saved directly into an excel spreadsheet. This allowed for easier data post experiment analysis of the experimental data. The measurement of five samples simultaneously allowed for direct comparison of sample compositions in identical environments. It was also useful in identifying experimental faults and distinguishing responses to equipment failure from those to actual vapour exposure and individual sample response.

5.4 Preliminary Experiments

The first sets of experiments developed were designed to be broad sweeping tests to identify the most influential variables for later more detailed experiments. Further to this it was possible to eliminate variations of samples that had very poor or no response at all. The first set of experiments consisted of testing on seven variables as listed below:

- Polymer Type
- Powder or Granular QTC
- Droplet Size
- Polymer to Solvent Ratio
- Filler to Solution Ratio
- Vapour Type
- Concentration of Test Vapour

At the time of undertaking these preliminary experiments it was not known which variables would have the greatest effects if any at all. With the benefit of conducting five experiments at a time it was possible to look at a large number of variables in a short time. Each experiment was repeated three times, this was not enough to gain any real quantitative data however qualitative assessment of each variable could still be made. A brief discussion of each variable and the effects on sample response will now be reported. Throughout the preliminary experiments only the variable mentioned was changed. All other variables were maintained at the values determined best by quantitative testing:

- | | |
|-----------------------------|--------------|
| • Polymer type | #1 |
| • Filler type | Granular QTC |
| • Droplet Size | 10 μ l |
| • Polymer to Solvent Ratio | 2 g to 10 g |
| • Granule to Solution Ratio | 2 g to 4 g |
| • Vapour Type | THF |
| • Vapour Concentration | 113000 ppm |

Polymer Type

The vapour sensors are prepared using a binding polymer with QTC granules mixed into it. Use of different polymer types was expected to have an effect of sample response to vapours and environmental responses due to the different molecular structures and solubility parameters of different polymers. A range of five different polymer types were investigated, they were as follows:

1. Polystyrene-b-poly(ethylene-ran-butylene)-b-polystyrene
2. Polystyrene-b-polyisoprene-b-polystyrene (17wt% styrene)
3. Polystyrene-b-polybutadiene-b-polystyrene
4. Polystyrene-b-polybutadiene
5. Poly(chloroprene)

For the remainder of this report the above polymers will be referred to by their reference number, and the prefix PS denoting Polystyrene and PC Polychloroprene i.e. PS #1 through to PS #4, and PC #5. The rationale for the choices was somewhat subjective, since detailed characterisation was not available to determine the most suited polymers for vapour sensing application.

A number of polymers were initially identified by Peratech, and trials carried out to produce dissolution in suitable solvents. From these trials, polymers were identified with solubility parameters ranging from approximately 7-12 $(\text{cal}/\text{cm}^3)^{1/2}$, this was a range of solubility parameter relating to the VOC vapours to be detected and also the solvents available to dissolve the polymers. A number of these polymers were subsequently disregarded due to insolubility or unsuitable physical form (e.g. waxy); a selection of 15 polymers was made.

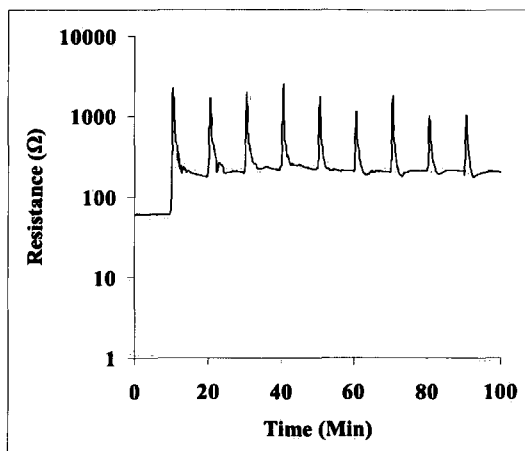
Various granule formulations were manufactured to assess the effect of granule size and composition upon the properties of a (granule/ polymer solution) blend. It was found that granules manufactured with relatively low polymer content (i.e. >20:1 filler/polymer in granule composition), and small size (<45 microns) were suitable. These granules were easily dispersed into the polymer solutions, and generally produce a conductive structure when evaporation of solvent

occurs. Larger granules did not blend homogeneously with the polymer solution, and were not suited to droplet formation.

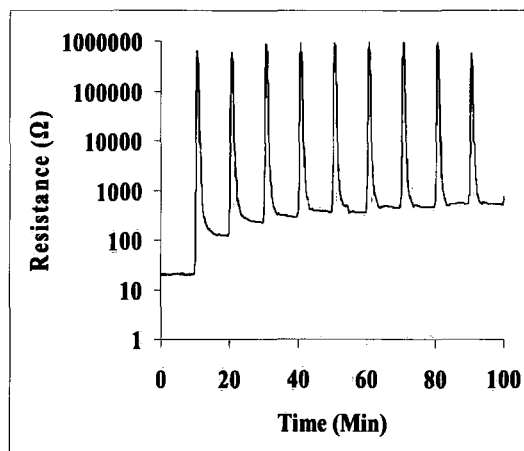
Following testing of these polymer types five were chosen as the most promising by Peratech, based on start resistance, adhesion to sample boards and indication of response to solvent vapours. The latter of these factors simply involved monitoring a resistance change in a sample as it was put in proximity to the surface of a solvent vapour. The polymer was judged to be suitable if start resistances of like polymer samples were similar, samples remained adhered to their surfaces during testing and there was a measurable electronic response and then recovery from exposure to Toluene and Acetone vapours.

Figure 5.8 shows a typical response of each of the five chosen polymer types to exposure of 113000 ppm of THF vapour. In the preliminary experiments exposures were undertaken using high concentration values in order to determine the response characteristics of sample at the limits of their potential ranges.

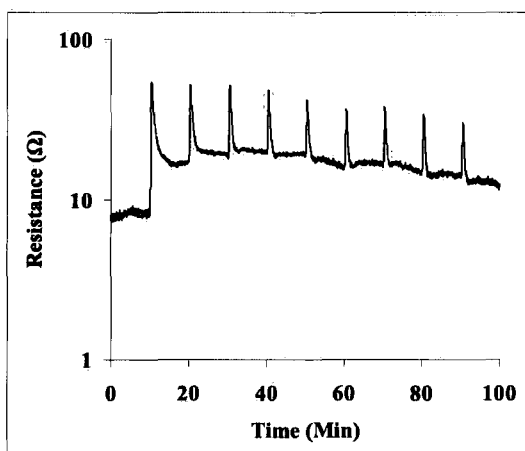
PS #2 and #4 showed consistently higher response to THF vapour compared to PS #1 and #3. PC #5 exhibited different behaviour to all other polymers. Upon exposure to solvent vapour at 113000 ppm, it was seen that the resistance responds beyond the limit of the test equipment, 10 M Ω , remaining there even upon purging. It was found that PC #5 eventually recovered to its original start resistance after a time period of several days. This indicates that the diffusion rate associated with this polymer is vastly different to that of the other polymers. This is an interesting characteristic, but not relevant to this stage of testing as one of the primary requirements of the QTC Vapour Sensors is that they both respond and recover quickly to vapour exposure. On this basis PC #5 was removed from any further testing. There was not scope to test further all four of the remaining Polymer types due to time management and the number of other variables requiring investigation. PS #2 and #4 exhibited much larger response magnitudes than PS #1 and #3. Based on this observation only PS #2 and #4 were carried forward for further testing.



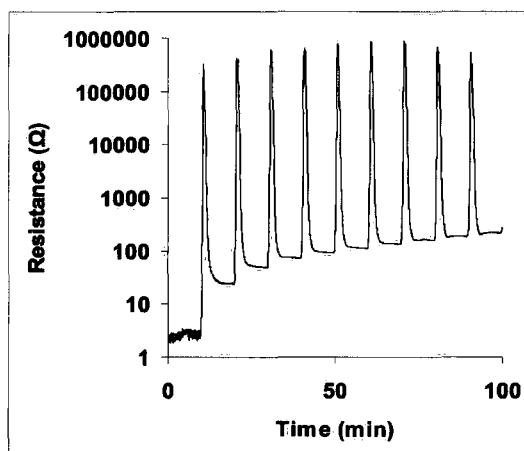
(a)



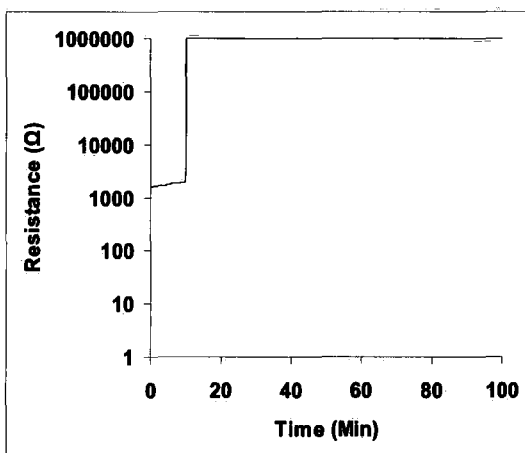
(b)



(c)



(d)



(e)

Figure 5.8: Response characteristics of; a) PS #1, b) PS #2, c) PS #3, d) PS #4, e) PC #5, to 113000 ppm of THF for 1 minute exposures with 10 minute purge times



Filler Type

The requirement to use QTC granules in the compositions as opposed to raw nickel power was a factor for consideration. Comparisons were made by undertaking parallel tests using identical solutions, with either granular QTC or nickel powder as the filler.

Figure 5.9 shows the response of an experiment identical to that used to produce figure 5.8d with nickel powder used in place of QTC granules. All of the experiments conducted showed a fundamental difference between the responses of the two sample types. Results, as shown in figure 5.8, were typical of all such powder based sample responses. Sensors prepared with Nickel powder gave consistently poor or no response at all to any of the solvent vapours. It is apparent that QTC granules are required in order to achieve any reasonable response to vapour from the sensors. No further samples were made using only nickel powder as the filler.

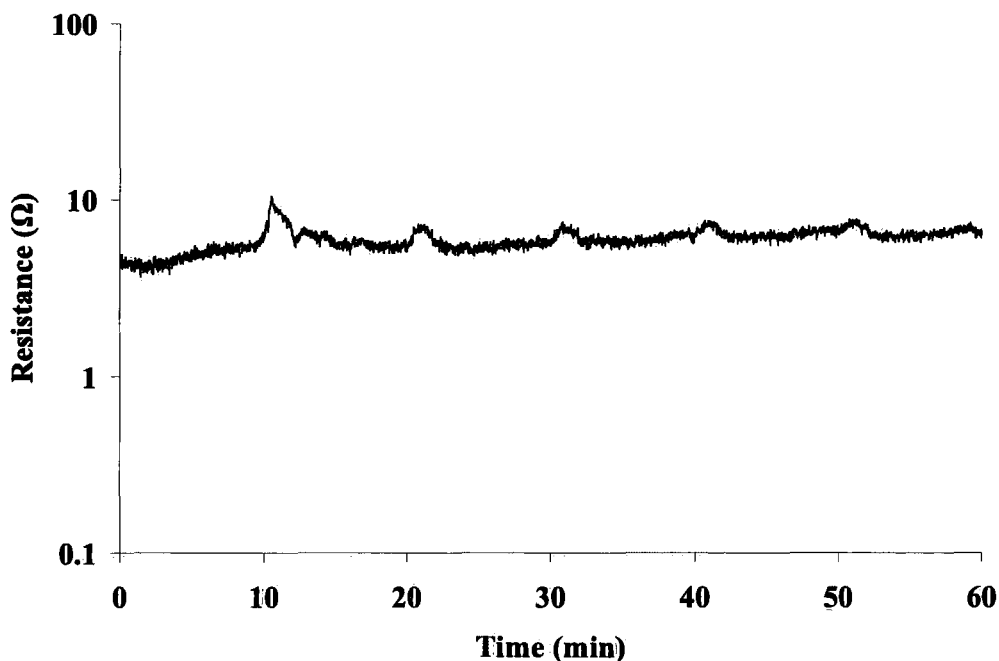


Figure 5.9: Response of Nickel powder based vapour sensor to 11300 ppm of THF vapour

This result was expected as the process of adding just nickel powder to a polymer in this way is effectively trying to produce QTC from a solution process. It has been found by Peratech in development of QTC production methods [2] that for a conductive composite a specific chemical process needs to occur to wet the nickel particles fully. Thus for this development of QTC, it is essential that properly processed QTC granules are first made and then bound together using a secondary polymer solution.

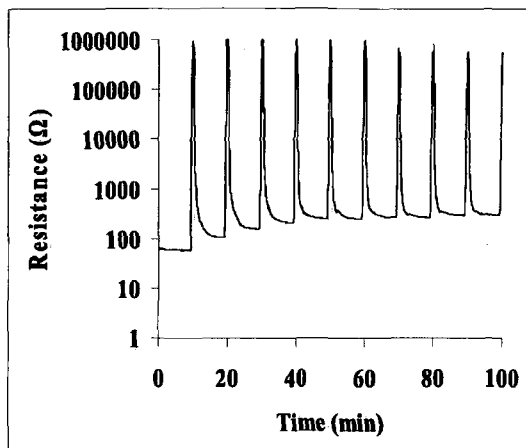
Droplet Size

Quantitative control of droplet size was possible using the positive displacement dropper described earlier. Since absolute sorption of vapour by a sensor will determine absolute resistance change, it was necessary to quantify any response changes due to droplet size. Based on the physical size of the sample board electrodes the following droplet sizes were determined for investigation:

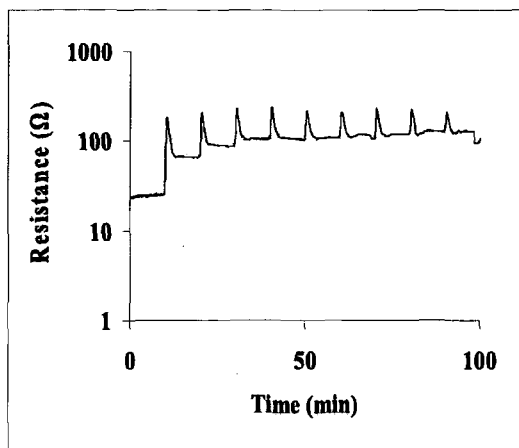
1. 5 μl
2. 10 μl
3. 20 μl

Figure 5.10 shows the difference in response behaviour between the three different droplet sizes used.

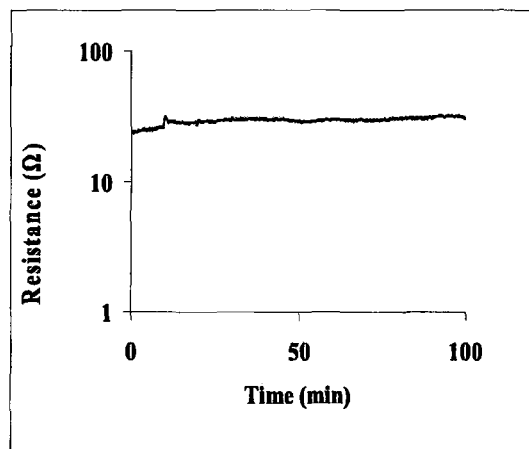
It can be seen that smaller droplets appear to give larger response amplitudes than the larger droplet sizes. This trend was seen across all of the data collected testing different droplet sizes. The behaviour seen is thought to be a result of absorption of vapour in smaller droplets having a greater relative effect on sample response than in larger droplets. It was decided that this variable would be examined further and is investigated fully in a later section of this report.



(a)



(b)



(c)

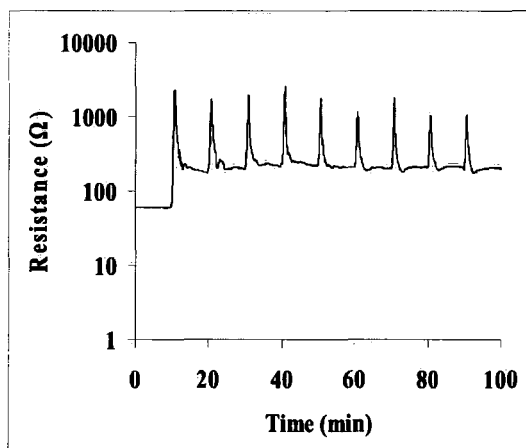
Figure 5.10: Response of Polymer #1 based samples exposed to 113000 ppm of THF vapour for droplet sizes of; a) 5 μl , b) 10 μl and c) 20 μl

Polymer to Solvent Ratio

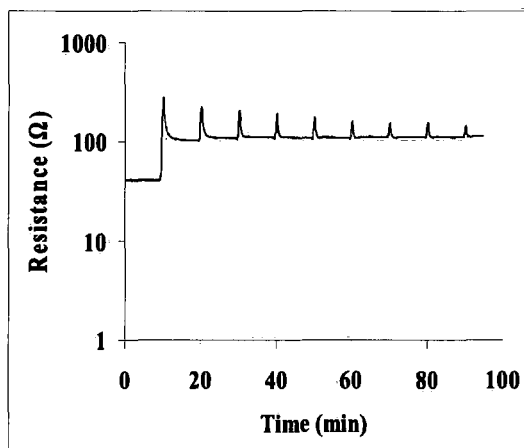
Approximate Polymer to Solvent ratio was initially determined from qualitative examination of the viscosity of the solutions produced. If the viscosity was relatively low the granules would not be brought close enough together upon curing to produce an inherently conductive material. If viscosity was too high then it was not possible to fully disperse the QTC granules into the solution. The optimum quantitatively determined Polymer to Solvent ratio was determined to be 1 g Polymer to 10 g of Solvent (Toluene in the preliminary experiments). Variations of this ratio were examined to indicate if there would be an effect

upon response characteristics. The following three Polymers to Solvent ratios were therefore examined:

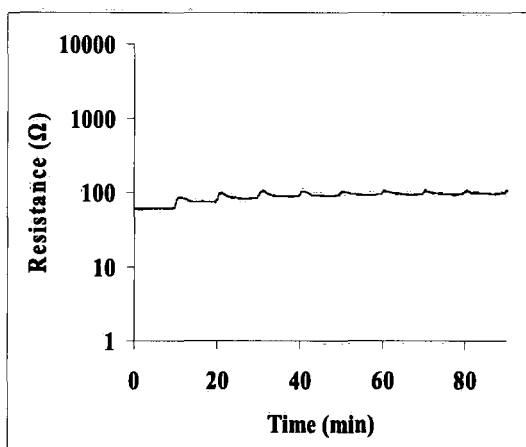
- 1) 1 g : 20 g
- 2) 2 g : 20 g
- 3) 3 g : 20 g



(a)



(b)



(c)

Figure 5.11: Response of PS #1 samples exposed to 113000 ppm of THF vapour for Polymer to Solvent ratios of; a) 1 g : 20 g, b) 2 g : 20 g and c) 3 g : 20 g

Figure 5.11 shows typical results for the three ratios tested. The general trend shows that there is a dependence upon the ratio between Polymer and Solvent. The data is not wholly conclusive and further more detailed analysis of this variable is conducted later in the report.

Granule to Solution Ratio

Again qualitative testing was undertaken in order to determine the best granule loading ratio to apply. It was found that even with relatively large changes in granule loading ratio that inherently conductive QTC could be made. It was anticipated that lower loadings of granules would be more likely to display a larger change in resistance since sensitivity would be greatest when the granules have the most freedom to separate during swelling. It was also believed that there would be greater homogeneity in the final mixture. Too few granules however were expected to have an effect on the number of overall conductive pathways available. Too high a granule loading was thought would affect the adhesion of the samples to the electrodes due to there being insufficient binding polymer to bond. Based on these assumptions and indications from qualitative assessment the following three Granule to Solution mixing ratios was investigated:

- 1) 2 g to 4 g
- 2) 1 g to 4g
- 3) 4 g to 4 g

Figure 5.12 shows typical response characteristics from the three variations of granule loading. The overall results showed that there was a dependence on the granule loading ratio that was worthy of further investigation. A larger range of ratio values and a quantitative assessment of this variable will be discussed further in later sections.

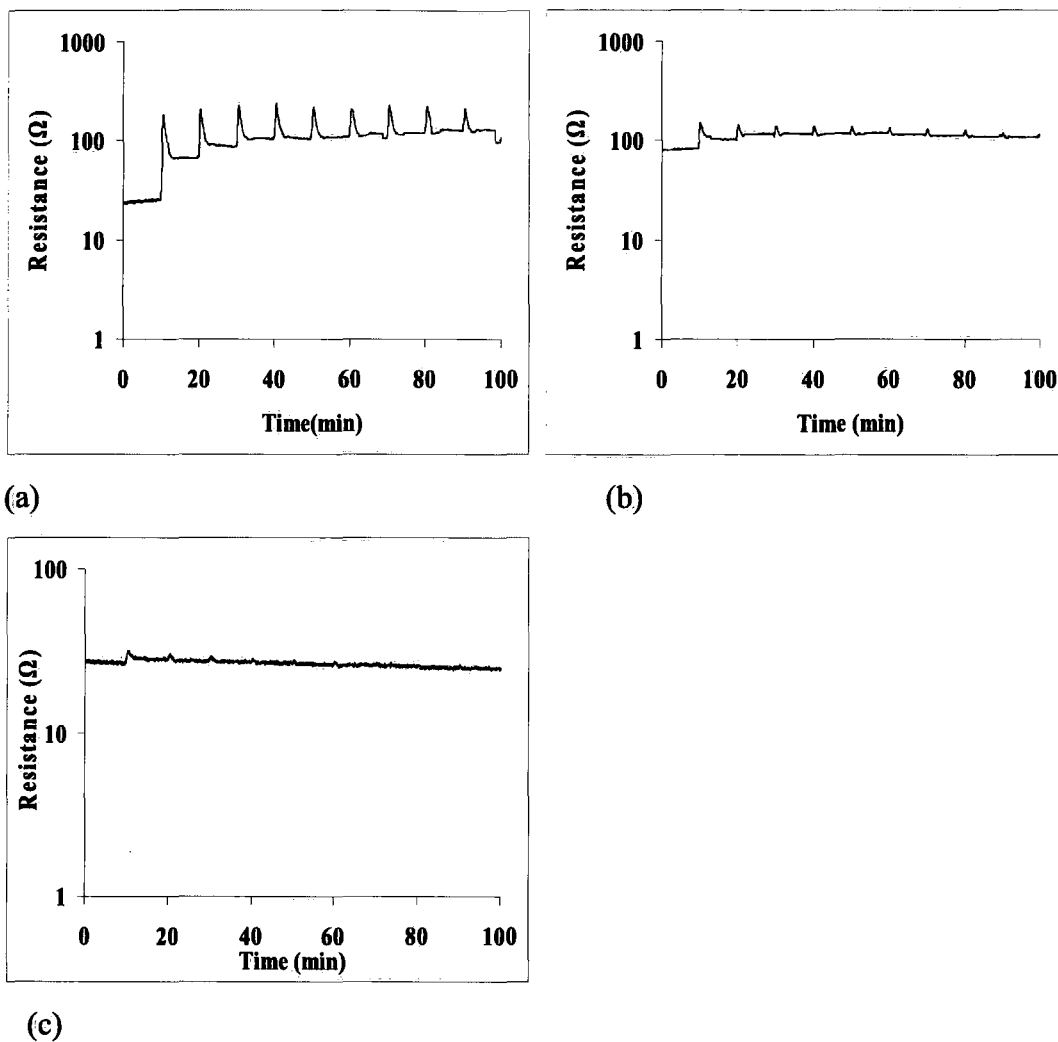


Figure 5.12: Response of PS #1 based samples exposed to 113000 ppm of THF vapour for Granule to Solution ratios of; a) 2 g : 4 g, b) 1 g : 4 g and c) 4g : 4g

Vapour Type

The type of test vapour exposed to the samples is paramount to the potential application within an electronic nose system. Furthermore it was important to identify solvent vapours that readily create good response in the samples being tested here in order to easily investigate the effects of the variables of sample composition. Four vapours were considered for exposure to the samples, they were as follows:

- 1) Hexane
- 2) Tetrahydrofuran (THF)
- 3) Toluene
- 4) Acetone

Typical responses are shown in figure 5.13. The downwards trends of the response peaks seen in parts a) and d) of figure 5.13 are a result of experimental flaws; specifically there was an overpressure in the vapour bubblers leading to too high concentration for the first few exposures.

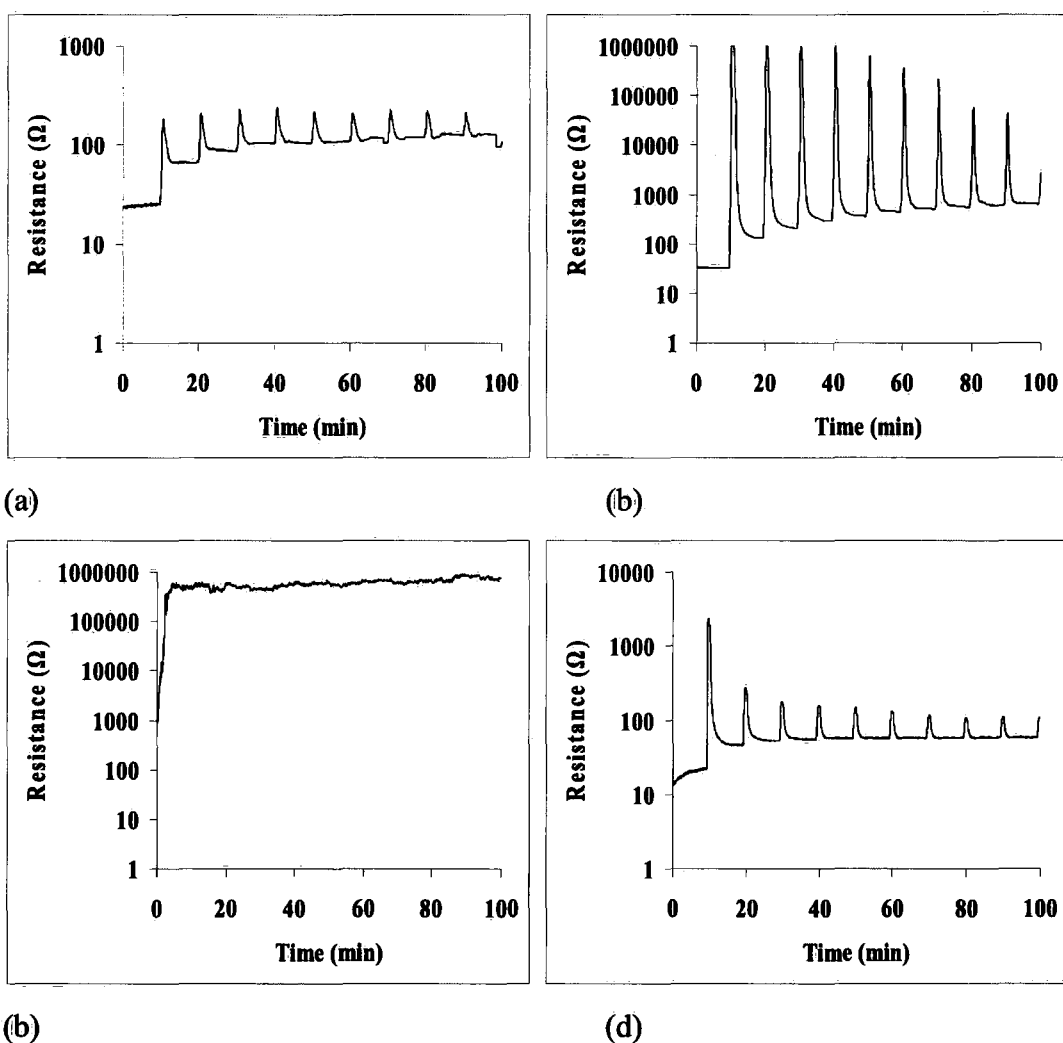


Figure 5.13: PS #1 based samples tested against four solvent types; a) Hexane, b) THF, c) Toluene and d) Acetone, all at 113000 ppm

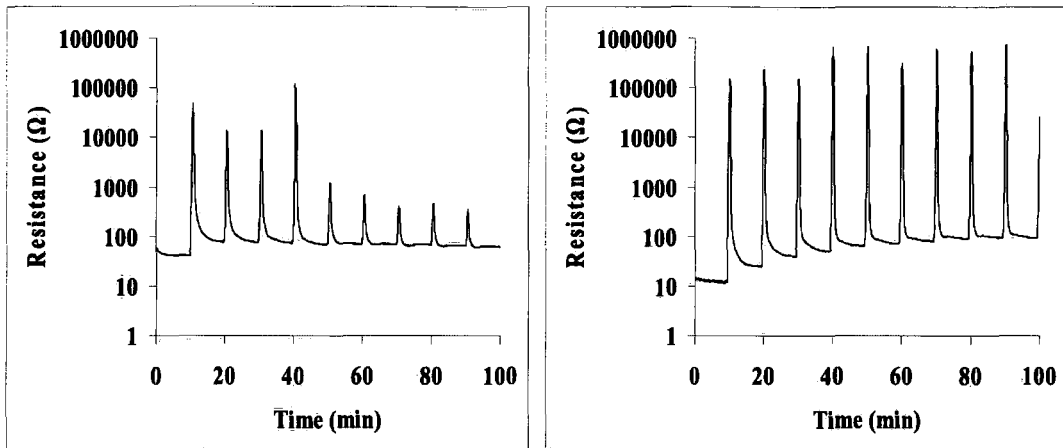
General trends indicate that there is a slightly larger response of all the polymers to THF than Hexane with exposures to Acetone slightly less than those to Hexane. Exposures to Toluene showed distinctly different response. Initial exposures showed some response; however there appeared to be no recovery by the samples upon purging. It was also found that subsequent new samples loaded into the test chambers, even after significant purging, were showing an immediate response. This indicated that the nitrogen purging was inefficient at purging the toluene. Although an interesting phenomenon warranting further investigation, it was not prudent to continue testing with toluene in this thesis. It was decided that based on the slightly better response characteristics that further sample composition experiments would use THF as the main test vapour.

Concentration of Test Vapour

Equally as important as distinguishing between different test vapours for an electronic nose system is the ability to detect the amount of a specific vapour. In order to confirm that the QTC vapour sensors are capable of this, three concentrations of test vapour were exposed to samples. At the time of conducting these preliminary tests the only method of dilution was via mixing with different MFCs, thus the three concentrations examined at this stage of testing were relatively high. The following flow rate ratios of Nitrogen to Solvent Vapour were implemented:

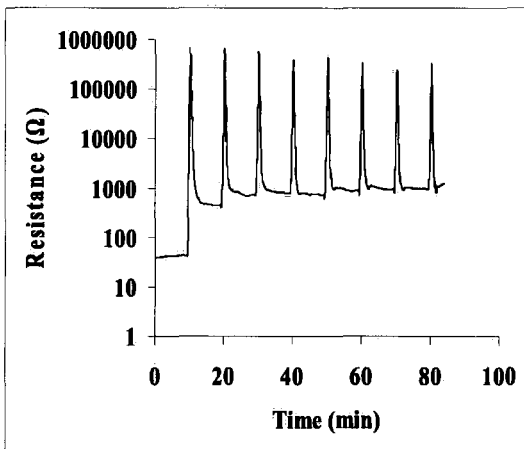
- 1) 20 : 10 ml/min (56500 ppm)
- 2) 10 : 20 ml/min (113000 ppm)
- 3) 00 : 30 ml/min (169500 ppm)

Figure 5.14 shows typical response characteristics from the three concentrations of exposure vapours. The general trend seen in figure 5.14 is representative of all the experiments undertaken. The expected correlation was observed between concentration and response, with higher vapour concentrations relating to larger sensor responses. A detailed set of experiments and analysis into vapour concentration effect upon response size is given later in the thesis.



(a)

(b)



(c)

Figure 5.14: Response characteristics of QTC vapour sensors to THF vapour at: a) 56500 ppm, b) 113000 ppm and c) 169500 ppm

Conclusions to Preliminary Experiments

The preliminary experiments provided information on the variables that would be best to investigate in further experiments and those that could be discontinued.

Polymer type was found to have an important influence on response with PS #2 and #4 highlighted as the most responsive polymers recommended for further investigation. It was noted however that the polymers tested so far were all of similar molecular compositions with just slight structural variations. Later

polymer type investigations would need to include additional polymers with different structures.

Nickel powder filler was discounted as a viable replacement for the QTC granules as the Nickel Powder based samples showed poor or no response to vapour exposure.

Droplet size was investigated and seen to have an effect on response magnitudes. Further experiments over a larger range of sizes are planned to quantify the effects of droplet size.

Polymer to Solvent and Granule to Solution mixing ratios were examined. Both sets of experiments indicated that mixing ratios of constituent materials played a large part in sample responses. Additional experiments are planned to investigate more fully the effects of changing these two ratios.

Exposure to different solvent types showed a different response magnitude for each vapour type, this was promising as a potential future application. However, time constraints lead to only THF vapour being used as the test vapour for later experiments. This was chosen as it provided the largest response magnitude of the four vapours. Experiments to investigate a full range of different test vapours to a larger range of polymer types would provide an area of potential future research.

Concentration dependence of QTC sensors was seen to occur. It was seen that higher concentrations of solvent vapour gave larger response upon exposure. Further experiments are conducted and analysed later in this PhD to quantify the relationship between solvent concentration and response magnitude. This data will also be used to identify the physical mechanisms present in the absorption and diffusion of solvent vapour into QTC sensors.

5.5 Vapour Sensing Experiments

Following the implementation and analysis of the preliminary experiments the main body of work was developed. This included experiments to further examine the variables highlighted by the preliminary experiments along with some additional parameters identified later.

The experiments were planned to fall into three main sections, Physical Parameters, Sample Composition and Environmental Responses.

Physical Parameters

The Physical Parameter experiments involved identifying the most suitable electrode and sample board materials in addition to investigating the effects of Droplet Size used to create the QTC vapour samples.

Three materials were identified as potential electrodes and two types of sample board material were considered. Copper on acrylic, Tin coated Copper on acrylic and Indium-Titanium-Oxide (ITO) coated glass were the three combinations experimented upon. The tin coated copper and pure copper electrodes were tested in order to ascertain if sample adhesion and sample conductivity could be improved with the addition of an interface layer. Identical experiments were undertaken using 10 μl of PS #4 based samples deposited on two sets of ten sample boards. The first set comprising just copper electrodes and a second ten deposited onto tin coated copper electrodes. Both sets of electrodes were printed onto acrylic sample boards. The QTC composite used was made with a 2:20 g Polymer to Solvent ratio and a 4:4 g Granule to Solution ratio. The samples were then loaded five at a time into the vapour sensing kit. All twenty samples were subsequently exposed to 16950 ppm of THF solvent vapour in 1 minute exposures separated by 10 minute purges using Nitrogen gas. Data was collected electronically for all 20 experiments for analysis.

A set of experiments were then undertaken to determine the suitability of using ITO coated glass sample board and electrode configurations. The primary aim of using glass based sample boards was to eliminate any possible thermal response that may have been present in the acrylic sample boards but it was also important to assess their general effect on sample response and characteristics in comparison to the copper and acrylic based samples. The ITO samples were tested at a later stage in the development of the sensors, at a time when the majority of experiments were being conducted with the aim of reducing temperature response. The primary binding polymer being tested at this stage of work was PVC. Thus PVC based sensors were compared on ITO and Glass to PVC sensors on Copper and Acrylic boards. Drop sizes were maintained at 10 μl with a Granule to Solution ratio of 1:1. Polymer to Solvent ratios for PVC based samples was found to be optimum at 1:10 g which will be discussed later. Twenty samples using PVC type samples were prepared, ten on ITO and Glass boards and ten on Copper and Acrylic boards. All twenty samples were then exposed to 9000 ppm of THF solvent vapour for 5 minute exposure, with 5 minute purging with nitrogen gas. The response data was collected alongside continuous temperature measurements made during the experiment. Stand alone temperature experiments are reported in a later section of this work. The start resistance of each sample was recorded prior to the first exposure using a Keithley 2420 source meter.

Following the preliminary experiments one of the variables outlined for further investigation was droplet size. A range of droplet sizes were investigated from 1 μl , the smallest size that would span the electrodes, up to 15 μl , the largest size that would fit onto the sample boards. The droplet sizes investigated were (in μl of mixture); 1, 2, 2.5, 4, 5, 7.5, 8, 10, 12, 15. Five samples at each size were made using PS #2 polymer. The same test regime as used to test sample board types was implemented with copper on acrylic boards used for all droplet sizes.

Sample Composition

The second series of experiments were aimed towards development of the composition of the samples themselves. The goal being to produce samples with the quickest response times, largest response magnitudes, with good recovery and repeatability. The four variables investigated at this stage of research were as follows:

- Polymer to Solvent Ratio
- Granule to Solution Ratio
- Polymer Type
- Polyurethane based granules

The first of these variables to be examined was the ratio of binding polymer to host solvent used to create the solution in which the QTC granules were to be dispersed. Indications from the preliminary experiments showed that the qualitatively assessed ratio of 2 g to 20 g (Polymer to Solvent) gave the “best” response characteristics. In order to quantify these claims five different ratios were chosen to experiment on, table 5.2.

Polymer (g)	Solvent (g)	Ratio
1	20	0.05
2	20	0.1
3	20	0.15
4	20	0.2
5	20	0.25

Table 5.2: Mixing ratios of Polymer to Solvent

PS #2 was used as the polymer with Toluene as the host solvent. Early quantitative tests by Peratech showed toluene as the solvent in which the polymers used were most readily soluble in.

Five samples were prepared at each mixing ratio with a 1:1 granule loading. Droplets of 10 μ l for each sample were deposited onto copper and acrylic boards. The samples were then exposed to 16950 ppm of THF solvent vapour for 1 minute exposure, with 10 minute purging with nitrogen gas. Ten exposures were completed for each set of samples. The samples were loaded into the vapour sensing equipment so that one sample of each ratio value was present for each batch of exposures. This ensured like for like comparison between ratios and allowed for easy identification of experimental faults. As with earlier experiments start resistance was recorded prior to exposure to vapour.

Granule to Solution mixing ratio was another variable outlined in the preliminary experiments as having effect upon sample response. In these experiments “solution” refers to the solution created from the Polymer and Solvent described in the previous section. It is evident that the two parameters will be closely linked and change in one will closely affect change in the other. In order to investigate Granule to Solution ratio five mixing ratios were investigated as outlined in table 5.3.

Granule (g)	Solution (g)	Ratio
1	4	0.25
1	2	0.5
1	1	1
2	1	2
4	1	4

Table 5.3: Quantities used to create Granule to Solution mixing ratios

Each sample was made using a solution comprising 2 g of PS #2 mixed with 20 g of Toluene. The remainder of the variables remained the same as those used in the Polymer to Solvent ratio tests outlined above. The same experimental

method was also used; samples were exposed to 16950 ppm of THF solvent vapour for 1 minute exposure, with 10 minute purging with nitrogen gas. Ten exposures were completed for each set of samples. Samples were also loaded into the test equipment so as to expose one of each ratio type in each batch of five tests. Start resistances were also taken prior to first exposure.

One of the most important factors in developing an electronic nose system is how different sensor types respond to a solvent vapour. It is therefore prudent to have available a range of potential polymer types that are capable of both a fast response and recovery. The preliminary experiments identified two polystyrene variants that were suitable for further investigation in addition to eliminating the polychloroprene based samples. In addition to these polymer types it had come to note that sample response to temperature change would be an important factor for any future applications. To this end two additional polymer types were suggested for testing as binding polymers. These were polyvinyl chloride (PVC) and polyphenylene oxide (PPO). These were chosen on the basis of their slightly stiffer less rubbery molecular structures, making them less likely to respond to small temperature changes. It was found that in some preliminary experiments to determine the suitability that neither of the two new polymers was fully soluble in Toluene. It was however possible to dissolve both polymers into chlorobenzene solvent. There was insufficient time to conduct a full set of quantitative tests such as those conducted on the polystyrene based samples. However qualitative testing and comparison to similar effects seen during the quantitative polystyrene testing yielded polymer to solvent ratios of 1:20 g for PVC and 2:20 g for PPO polymers. Granule to solution ratios were maintained at 1:1 loading for all the samples tested, both polystyrene based and the PVC and PPO based ones. It was found that good conductivity was produced in the new samples using these values with start resistances comparable to those seen in the polystyrene samples, i.e of order 50 to 100 Ω . This was important as it was found that start resistance of samples had a significant effect upon response magnitudes. Further discussion of this phenomenon and the derivation of the values 50 to 100 Ω is discussed in detail in the next chapter.

In order to compare the four polymer types, samples were prepared using the optimum conditions and physical parameters calculated from earlier tests. Details of these calculations and conclusions are discussed in detail in Section 5.6 of this thesis. Copper electrodes on acrylic sample boards were utilized with 10 microlitre droplet sizes used to deposit the sample. Granule to Solution loadings were maintained at 1:1. A summary of the Polymers used and their host solvents is given in table 5.4.

Polymer	Solution	Relative Ratio
Polystyrene-b-polyisoprene-b-polystyrene	Toluene	2 to 20
Polystyrene-b-polybutadiene	Toluene	2 to 20
Polyvinyl chloride	Chlorobenzene	1 to 20
Polyphenylene oxide	Chlorobenzene	2 to 20

Table 5.4: Polymer types and relative solvent mixing ratios

For each polymer type ten samples were manufactured using the quantities and variable values given above. Sample start resistances were measured before any vapour exposures. All forty samples were then exposed to 4133 ppm of THF vapour. This is significantly lower than in previous experiments and represents the fact that the sensors being used at this stage of development are much more responsive to vapours. Using a lower concentration level also means that all the sensors will now have a peak response magnitude as opposed to previous experiments where nearly all samples hit the equipment measuring limit (10 M Ω) and response time to this limit was the measurable quantity. Exposure times were increased to 5 minutes to allow time for a full response and purge times were subsequently reduced as the much smaller amounts of solvent were found to leave the samples in a much shorter time period. The additional length in exposure times also allowed for better analysis of temporal response characteristics.

Polyurethane based QTC granules were made to test against the Silastic-T4 (silicone rubber) based granules used throughout testing up to this point.

Previous work by Hands [12] showed that polyurethane based QTC was a viable alternative to the standard silicone rubber based composite. Some of the vapour testing conducted by Hands even suggested that it may in fact be more responsive to certain solvent vapours. In order to quantify this, experiments were undertaken using polyurethane granules in intrinsically conductive QTC vapour sensors. The polyurethane samples were manufactured in the same way as the silicone rubber based samples with the simple replacement of the Silastic T4 with a polyurethane based rubber compound. Samples were then created by mixing these granules into a solution of 2 g PS #2 and 20 g Toluene. 10 μ l droplets were deposited onto copper and acrylic sample boards and left to cure. The granule to solution mixing ratio was varied in the same way as tested for the silicone samples to allow direct comparisons with earlier results. The mixing ratios are outlined in table 5.5.

Granule (g)	Solution (g)	Ratio
1	4	0.25
1	2	0.5
1	1	1
2	1	2
4	1	4

Table 5.5: Mixing ratio of Polyurethane QTC granules in Toluene solution

Five samples were produced for each loading ratio and all 25 samples exposed to 16950 ppm of THF vapour. The concentration of test vapour was increased for these experiments in order to allow direct comparisons with earlier work. Exposure times were set to 1 minute and Purge times to 10 minutes. All start resistances were independently recorded before exposures to vapour.

Environmental Responses

Having conducted experiments to ascertain the fastest most responsive sample compositions for QTC vapour sensors it was then necessary to characterise how they responded to changing environmental parameters. This characterisation would be of particular use for commercialisation of the QTC vapour sensors.

An important factor as eluded to already was the temperature dependence of the vapour sensors. The ultimate goal would be to have a vapour sensor that both responds well to vapours but has very little response to temperature. However these two parameters are not mutually exclusive since the processes governing swelling and vapour response are very much linked to the molecular structure of the polymer that dictates temperature response. Details of these ideas are discussed fully later. With this in mind the minimum aim of this section of experiments was to be able to predict the temperature dependence of samples so their effects could be easily removed in the data processing stages of any future applications.

In order to investigate the temperature characteristics of QTC vapour sensors an oven was used to change the temperature of samples over a fixed range while the sample resistances were monitored. The oven used was custom built made in house at Durham University, borrowed from the teaching laboratories. It could be ramped up to temperatures of 200 °C and was accurate to the nearest degree. Sample temperatures were monitored via a thermistor placed in contact with the sample boards being used. Both temperature and sample resistance was measured in real time at a sampling rate of 1 measurement per second through the Keithley 2740 multimeter connected to the PC and monitored via a LabView program.

Three sample sets were investigated for temperature dependence, these were based on the three main polymer types investigated earlier using their respective optimum compositions. A decision was made to use PS #2 as a representative of the polystyrene samples as there was insufficient time to investigate both PS #2 and #4. The decision was based on results obtained in the polymer type

experiments, analysis and discussion of which are given later. The binding polymers and host solvents used are summarized in table 5.6.

Polymer	Solution	Relative Ratio
Polystyrene-b-polyisoprene-b-polystyrene	Toluene	2 to 20
Polyvinyl chloride	Chlorobenzene	1 to 20
Polyphenylene oxide	Chlorobenzene	2 to 20

Table 5.6: Binding polymers and host solvents used for samples measuring temperature dependence

All samples were manufactured using silicone based QTC granules in a 1:1 ratio and deposited onto copper and acrylic sample boards in 10 μ l droplet sizes. Five samples based on each polymer type were manufactured. The samples were then placed in the oven and the temperature ramped from room temperature (approx. 22 °C) up to 80 °C. The resistance of the samples was monitored and recorded as temperature was increased. This was conducted on all fifteen samples.

An additional 5 samples were produced using PVC as binder polymer maintaining the same parameters as used above with the exception of those being dispensed onto ITO and glass sample boards. These five samples were also subjected to a temperature ramp from room temperature to 80 °C and their resistances recorded.

Concentration of Solvent Vapour

The final set of experiments undertaken on the QTC vapour sensors in this PhD was to quantify the sensors responses to concentration of test vapour. Analysis of both amplitude and temporal responses would be used to evaluate both sensor characteristics and physical mechanisms responsible for the characteristics.

Experiments were conducted on PVC and PS #2 samples to record their response to THF vapour at over a range of exposures of set at different concentrations. PPO samples were not investigated at this stage as there were adhesion issues with the samples causing more than half of them to fail, this is discussed later. The range of increments available outlined in table 5.1 earlier were used to provide exposures of THF vapour from 22 ppm to 105,000 ppm in 15 increments. Sufficient samples were produced in order to allow five samples to be exposed to each different concentration setting for both polymer types. Exposures to THF vapour were then conducted 5 samples at a time for 5 minutes with 5 minute purges in between. Ten successive exposures to each concentration value were made. The samples used were prepared to the same specification as those described in the previous section for temperature response experiments.

5.6 Vapour Sensing Results and Analysis

Introduction

The experiments conducted and reported on here are those to identify the best physical parameters and sample composition for QTC vapour sensors. The term “best” throughout this thesis is used to describe parameters and composition of QTC vapour sensors that have the fastest response with largest peak amplitude. Looking back to figure 5.8b (reproduced below as figure 5.15 for convenience) show typical high concentration response characteristics to THF vapour by QTC vapour sensors.

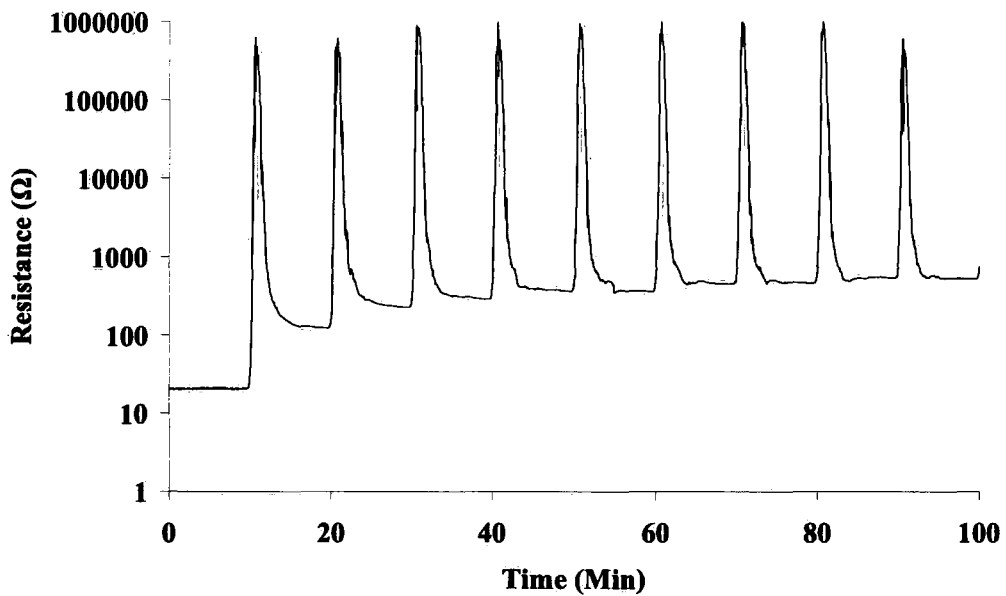


Figure 5.15: Response characteristics of a PS #2 based sample exposed to 16950 ppm of THF solvent vapour.

There is an initial start resistance of order 50 Ω , but this can vary from 10 Ω to 100 Ω depending on the composition. A first exposure after 10 minutes shows a very fast response by increase in resistance up to a peak response value, limited to 10 M Ω in this example due to equipment limitations. Vapour has been absorbed into the sample causing the polymer binder matrix to swell. This subsequently reduces the compression on the enclosed granules allowing them

to move further apart and so resistance is increased. This is analogous to reducing applied physical pressure to standard bulk QTC seen in the first half of this thesis. The full dynamics behind the response to vapour absorption will be discussed in detail later. After a minute of exposure the system returns to purge and it can be seen that the resistance drops again. The rate of recovery is much slower than the rate of response. This is attributed to different vapour concentration differentials between the two regimes and can be explained by referring to the CASE-II diffusion mechanism. This describes a wave-front propagating through a material with a concentration gradient driving it into the polymer. However upon leaving the polymer there is no wave-front and so solvent molecules are drawn out because of a concentration gradient caused by the differences of vapour pressure inside and outside of the polymer material of the analyte. After purging for 10 minutes the sample is then exposed again.

It can be seen however that the sample does not return to its original start resistance upon recovery. It is seen that subsequent responses recover to a consistent baseline after the second exposure. The step up from the start to the baseline through the rest of the responses is attributed to stress relaxation in the polymer upon first exposure. Upon first exposure the chains in the polymer expand due to swelling, reducing entropy of the system as discussed in section 4.2. During the first purge the polymer chains then relax, but reform to a more energetically favourable formation that is different to the initial conditions. This is a one off occurrence and is only seen in the first response as subsequent expansions then return to the new configuration during purging.

Evidence of this is seen in mass uptake measurements (covered in the next chapter) where there is no evidence of any residual trapping of vapour in the matrix that could cause a response by maintaining a swollen regime whilst purging. Also the step change is only observed in exposures to relatively high concentrations of vapour, i.e. those that can cause swelling capable of expanding the polymer chains past a point where they return to a different configuration.

5.6.1 Physical Parameters

Electrode Type

The first experiments conducted were to identify the most appropriate sample boards and electrodes to use. The response of the three types of sample board were analysed, they were; Copper and Acrylic, Tin coated Copper and Acrylic and ITO and Glass. The response of the Copper and Tin coated electrodes both exceeded the peak limitations of the equipment, with all of their response magnitudes exceeding $10\text{ M}\Omega$. For these results the time to respond to the maximum limit was used as a measure of the sample response to the vapour. Figure 5.16 shows all of the measured response times of both the copper and tin coated sample boards to 16950 ppm of THF vapour as a function of start resistance.

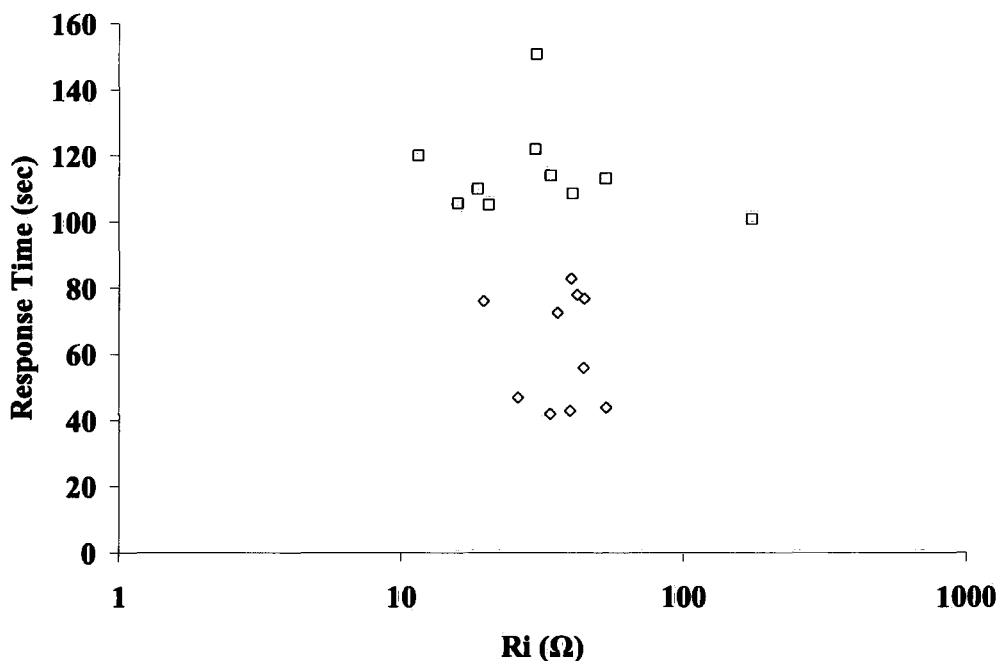


Figure 5.16: Response time to peak magnitude for copper and tin coated electrodes upon exposure to 16950 ppm of THF vapour, \diamond = Copper, \square = Tin

This data shows that the tin coated sample boards had in general longer response times and a slightly larger spread of start resistances.

The main factor that is affected by different electrode surfaces is adhesion and so electrical contact between electrode and sample material. It is intuitive therefore that poor electrical contact will lead to a poor response to vapour and reduced sensitivity. Thus it was surmised that there must be an underlying feature that was causing poor adhesion in the tin coated samples compared to the copper samples. A 182 times optical microscope was used to look at the surface of the electrodes being used. Figure 5.17 shows two images from the microscope showing sections of copper electrode surface and tin coated electrode surface.

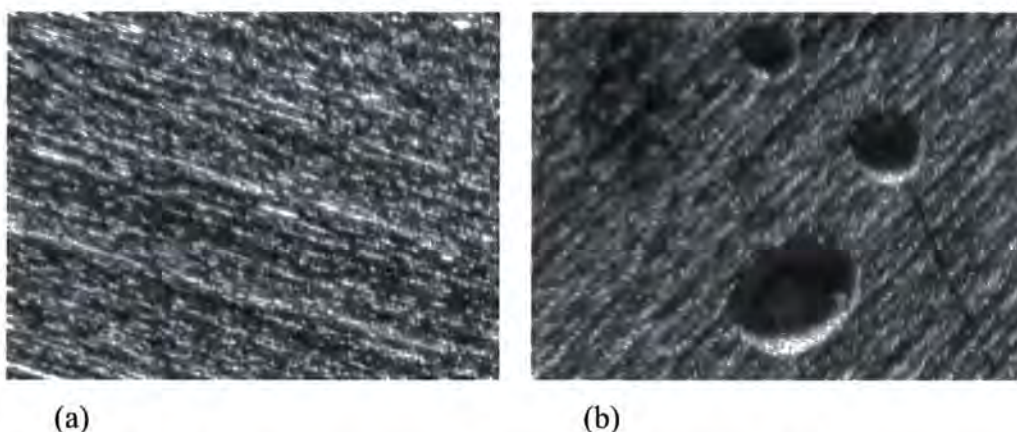


Figure 5.17: Optical microscope images at 182x for (a) a section of copper electrode surface and (b) a section of tin coated electrode surface

It is immediately apparent that there are a number of imperfections in the tin surface, shown in figure 5.23(b). These were seen over approximately 20% of the tin surface on all of the tin coated samples. These imperfections are deemed responsible for the poor adhesion of the sample and thus the longer response times for the tin coated samples. The original choice of using tin coated copper electrodes was to eliminate the possible effects of copper oxide layers on the electrode surfaces. However in practice the copper oxide layer has little effect and any dirt can be easily removed by wiping with acetone, whereas the imperfections seen in the tin coating are an inherent effect of the coating process. Plain copper electrodes would therefore be used in further testing with any contaminants or surface dirt removed by cleaning with acetone before sample deposition onto the surface.

The use of ITO coated glass electrodes was also investigated as an alternative to the copper and acrylic ones. A series of experiments were undertaken as described earlier, using PVC based QTC vapour sensors that were exposed to 9000 ppm of THF vapour. It was found that in these experiments the peak response of each exposure was within the equipments' measuring limitations and used as an indication of the samples sensitivity to vapour exposure. Figures 5.18 shows typical data sets for comparison:

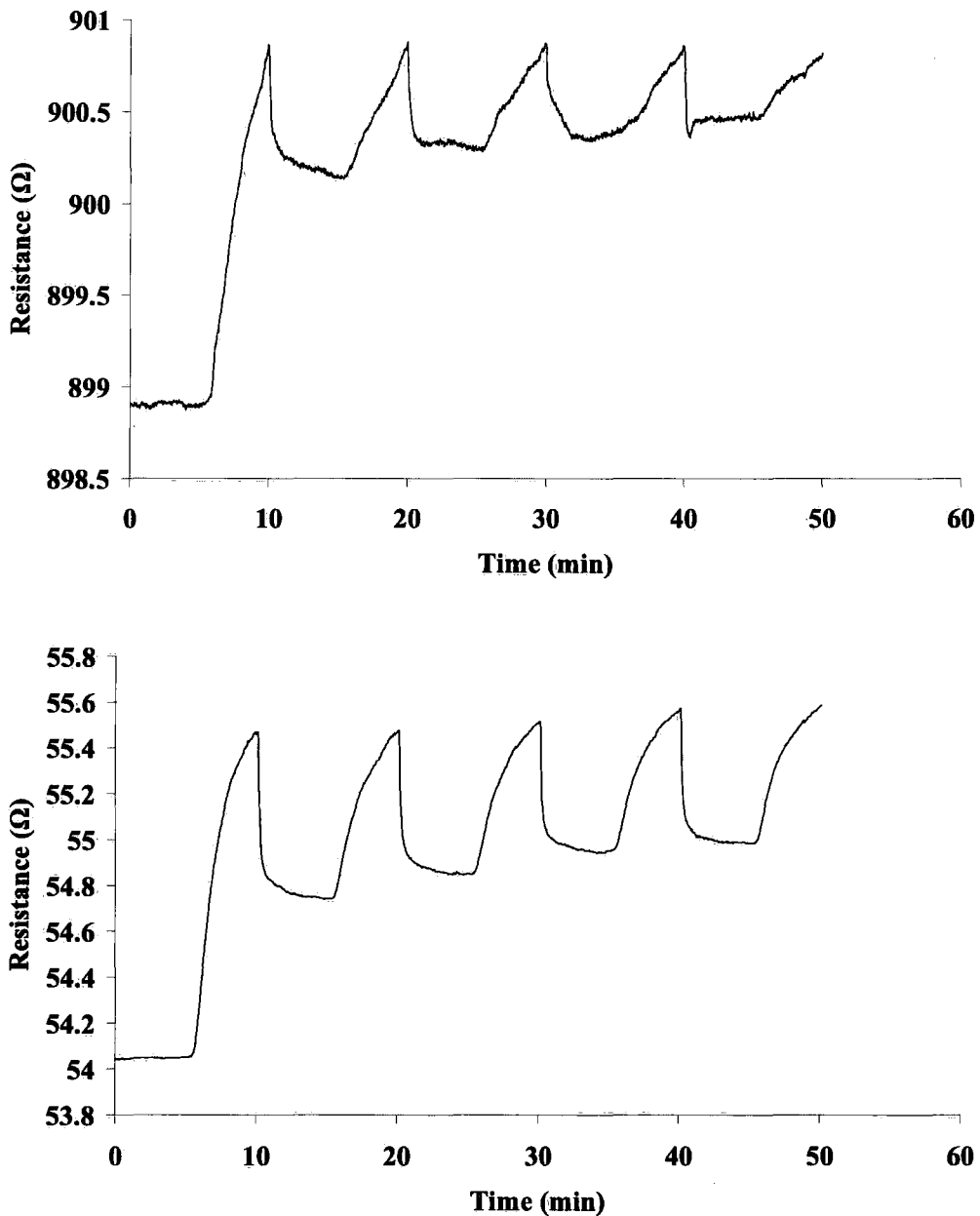


Figure 5.18: Typical response of PVC based QTC to 9000 ppm of THF vapour on (Top) ITO and (Bottom) copper and acrylic sample boards

The noise seen in the signal of figure 5.18(a) is an artefact of the measuring equipment and not the sample. Comparison between the two data sets above shows that the ITO based sensors exhibit very similar characteristics to those with a copper and acrylic base. Over all 48 samples were produced including those for vapour sensing. Prior to any vapour exposure the start resistance of each was recorded, in all there were 24 ITO samples and 24 copper samples. It was found that the average start resistance of the ITO based samples was 125 Ω , whereas the copper based samples showed an average start resistance of 48 Ω . Both sets of data exhibited a variance of start resistance of 20%. The higher average start resistance of the ITO based samples could indicate a possible weaker cohesion of polymer to the board surface but is more likely a factor of the higher resistance of ITO compared to copper.

Peak response magnitudes were measured for the sets of samples exposed to THF vapour. This was taken as the difference between resistance values immediately before exposure (initial resistance R_i) and immediately before purging is initiated (final resistance R_f). Thus the difference $\Delta R = R_f - R_i$ can be calculated for each response to each exposure. In order to make the data from different samples with different start resistances, the responses were all normalised by dividing through by respective R_i resistance values, a $\Delta R/R$ value for each response was therefore used in any data analysis. It was found that over ten repeat exposures to 9000 ppm of THF vapour, five ITO based samples and five copper based samples that the copper and acrylic sample boards corresponded to a higher average response magnitude. The average $\Delta R/R$ value for copper and acrylic board samples was calculated to be 0.0058, whereas the equivalent ITO based samples gave a value of 0.0027, approximately half the relative response amplitude.

This data coupled with the data comparing start resistances indicates that the copper acrylic boards may have a better surface adhesion with the sample material providing better electrical contact with the electrodes compared to the ITO glass boards. Images of the ITO glass surface do not show any imperfections as was the case for Tin coated electrodes. It is assumed therefore

that the poor adhesion is simply a factor of the surface bonding to glass being less effective than for acrylic with respect to the PVC based polymer QTC vapour sensors.

The ITO based samples gave adequate response to vapour but their preparation was both more complex and far more expensive than the copper and acrylic counterparts. The only factor that could make the ITO sample boards a viable option would be a large influence in preventing temperature response in QTC vapour sensors. This will be investigated later. For all other applications and experiments in the remainder of this project copper electrodes printed onto acrylic sample boards were used for preparing vapour sensors.

Droplet Size

The final stage of identifying the optimum physical parameters for vapour sensor designing was to investigate the effects of droplet size deposited on the sample boards. A range of droplet sizes were investigated as described earlier. Two sets of data are presented and analyzed in order to investigate the effects of droplet size, response time and start resistance.

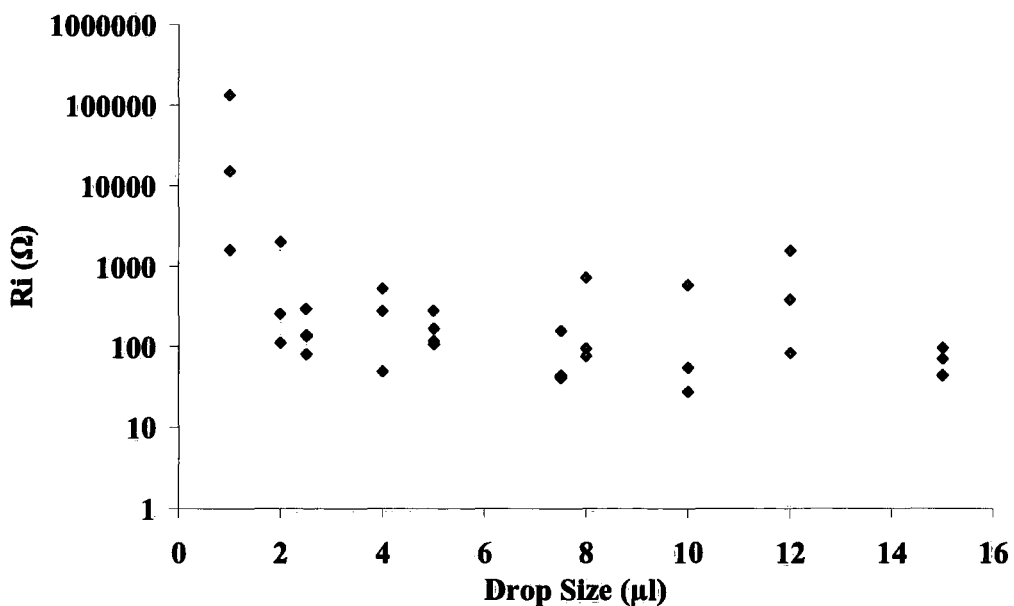


Figure 5.19: Start resistance as a function of droplet size

Looking at the initial resistance behaviour trend in figure 5.19 indicates that for very small droplets below 2 μl the start resistance begins to increase above this value the resistance remains roughly constant. This is explained simply in terms of contact area of polymer onto the electrodes. Above 2 μl there is sufficient contact area to create contact resistance that is greater than the inherent resistance of the polymer sensor, shown by the steady start resistance at higher droplets sizes. For small droplet sizes the contact area becomes less, which leads to contact resistance greater than that of the polymer. From this it is decided that sensors be created using deposits greater than 2 μl .

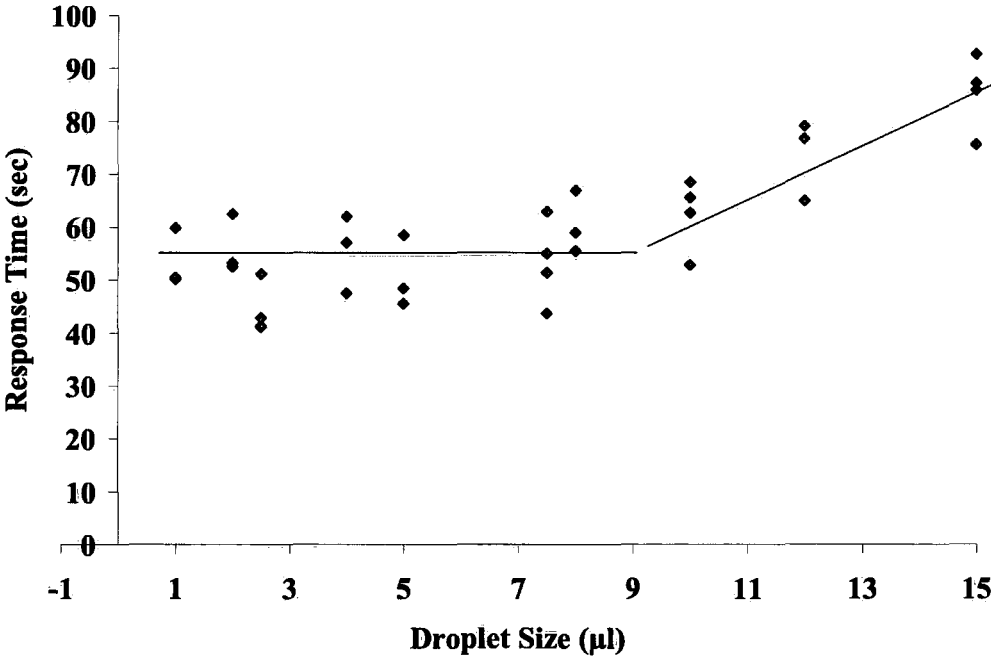


Figure 5.20: Response time as a function of droplet size

Figure 5.20 shows the response times of all the exposures of the samples to 16950 ppm of THF solvent vapour. It can be seen here that increased droplet size has a detrimental effect on response times. For sizes above 10 μl the rate of response increases greatly. The response times for droplets below and at 10 μl , are all in the range of 40 to 60 seconds. This change in behaviour is attributed to the mass of material that swells and causes resistance change. As droplets size

increases the amount of polymer required to swell to gain the same resistance increases. However above 10 μ l the rate of absorption is no longer quick enough for the whole bulk of the polymer to swell at the same rate as smaller samples. Thus longer response times are seen.

From this data, droplets sizes need to be 10 μ l or smaller in order to have optimized response times. The two sets of data presented in figures one and two it is seen that droplet sizes for QTC polymer deposition are required to be between 2 and 10 μ l. From a production point it is easier and more accurate to deposit larger droplets in a repeatable manner. Based on this the largest value in the optimum range (10 μ l) was used for the testing throughout the remainder of the experiments conducted.

5.6.2 Sample Composition

Having investigated the physical parameters of making the most effective QTC Vapour Sensors, the next stage was to investigate the optimum sample composition used. This was conducted in four main areas as discussed previously in the methodology, Polymer to Solvent ratio, Granule to solution ratio, polymer type and Polyurethane granules were examined. The aim of these experiments was to provide data to create vapour sensors producing the best possible response. Some known theoretical models will also be compared to the results in order to explain some of the characteristics seen.

Polymer to Solvent Ratio

The first variable evaluated was the ratio of binding solution into which the QTC granules were mixed. As described earlier five ratios were made and tested. The first thing to note is that the lowest ratio tested, 1 g to 20 g was not intrinsically conductive. The explanation of this result is that upon curing and the solvent evaporating away there was insufficient binding polymer to compress the granules effectively. In this case it is also considered that adhesion of the mixture to the electrode surface would be affected as it is the binding polymer that provides the surface adhesion.

It was seen during preparation that polymer sensors with low polymer ratios were very easily dislodged from the electrodes. Higher ratio polymers were found to be much more resistant to being physically removed. Although very rudimentary, this indicated effects of the surface adhesion playing a part in addition to granule compression.

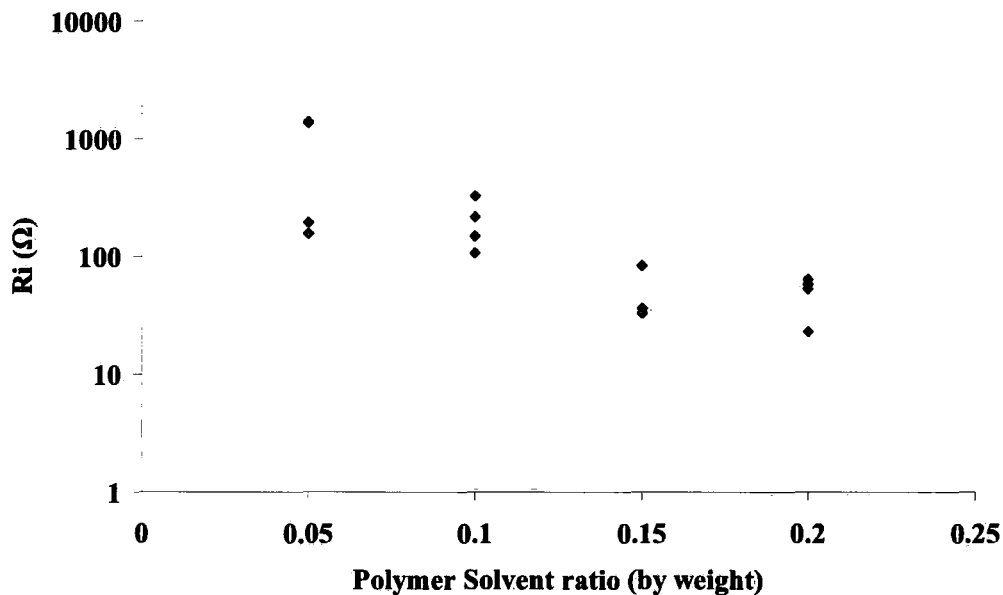


Figure 5.21: Start resistance of QTC vapour samples shown as a function of Polymer to Solvent ratio

For the remaining four ratios, start resistance has been shown as a function of polymer loading in figure 5.21. Although limited, this data shows that increasing ratio reduces the inherent start resistance of the samples. It can be seen that there is a spread of start resistances at each ratio value, this observation will be analyzed later in the report. Interpretation of this data is that the increased amount of binding polymer in the solution means that upon curing there is a greater compression of the granules from the increased polymer amounts and that this is analogous to applying greater physical compression to standard bulk QTC, only here the compression is provided by the contraction of binding polymer whilst curing. However it is expected that if the relative amount of polymer was increased yet further that it would begin to act between granules, causing a separation between them and effectively reducing the conduction pathways through the material. This would be seen on this graph as an increase in start resistance at larger polymer loading ratios.

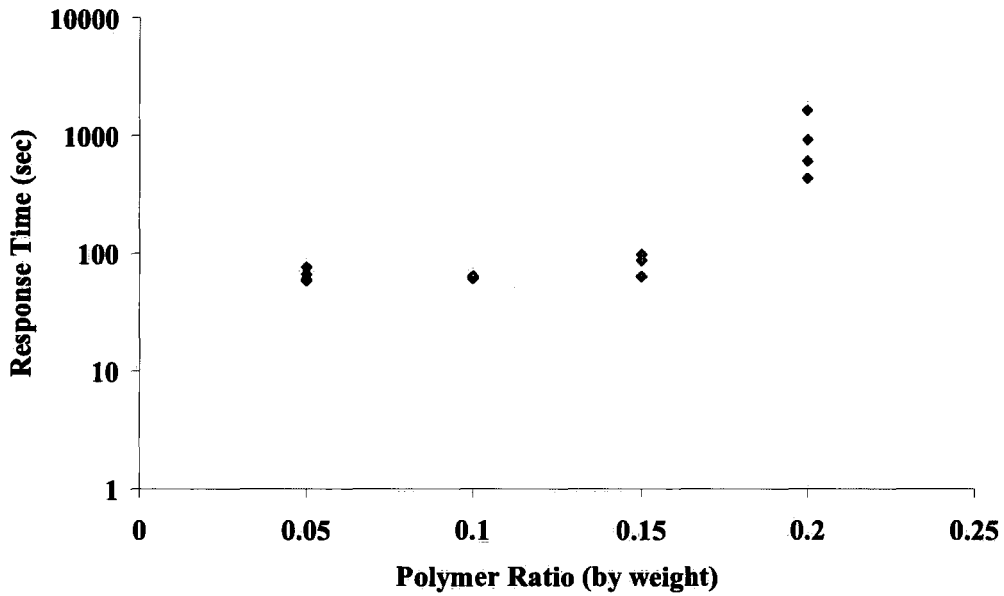


Figure 5.22: Response time of QTC samples to THF exposure at 16950 ppm as a function of Polymer to Solvent ratio

Figure 5.22 shows the response times of the samples as a function of polymer to solvent ratios. Here we see that the average response time does not significantly change in the lower ratio samples.

However upon reaching the ratio of 0.2 the response time doubles and the spread of data increases. From this we can infer that at high polymer loading there is a greater binding effect on the enveloped granules making it harder for the polymer to expand upon exposure and swelling. In the lower start resistance regime, of the higher polymer ratio, the samples will be more sensitive to small changes as they are near to the exponential region of the QTC conduction trend.

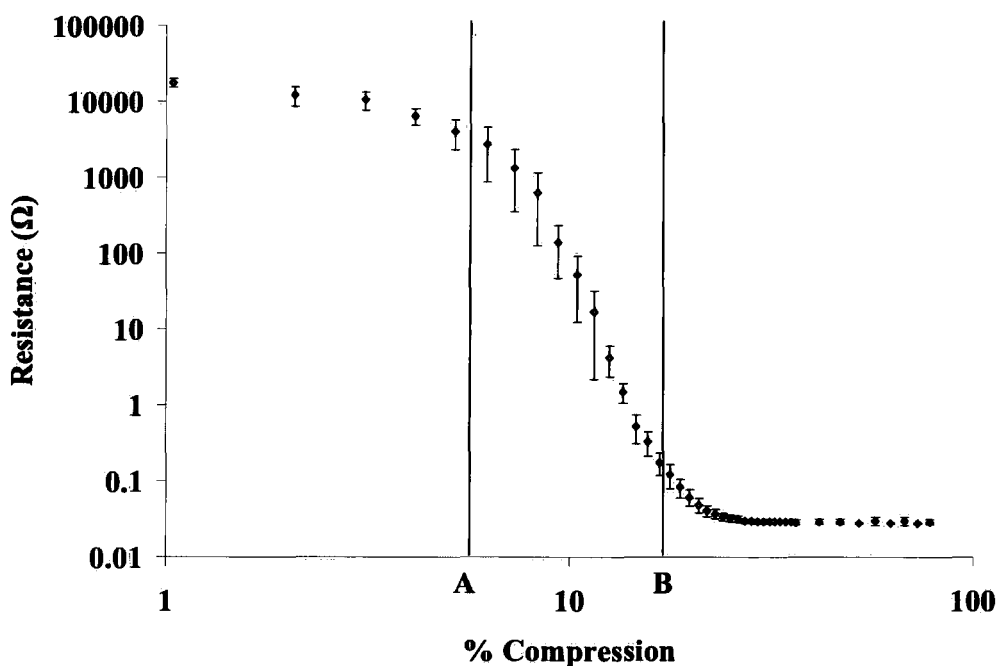


Figure 5.23: Resistance response to applied compression for bulk QTC

Small sample to sample variations caused by the heterogeneous morphology of QTC exhibit larger variation in response times. The idea of start resistance effects can be described further by analogy to bulk QTC properties.

Figure 5.23 shows a typical resistance to compression response of QTC. If the polymer ratio is set so that the start resistance of the sample falls between A and B, and the sample is then exposed to solvent causing swelling, the same effective change in compression by the swelling will have a much greater effect on resistance than outside this region. It is believed from this that there is a range of sample start resistance that provides best vapour response.

In addition to investigating solvent to polymer ratio, the ratio of granules added to the solution was investigated. Five granule loading ratios were investigated; figure 5.24 shows the measurements of start resistance as a function of loading ratio.

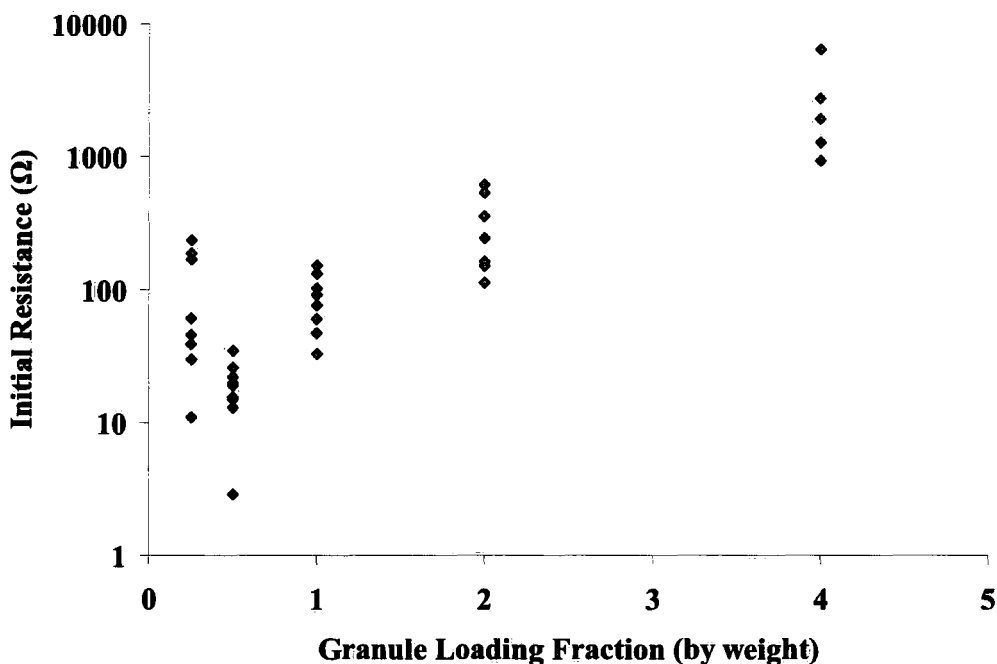


Figure 5.24: Start resistance measured as a function of Granule to Solvent mixing ratio

Here it can be seen that the amount of granules have a significant effect upon the sample characteristics. Starting at the highest loading ratio of 4 g granules to 1 g of solvent (4.0), it can be seen that the average start resistance is much higher. Start resistance then falls steadily down to a loading of 0.5. Granule loading below this threshold exhibits a rise in start resistance. From these results a similar principle as applied to polymer to solvent ratio previously can be used, as the same process is occurring. When there is a large quantity of granules added there is less binding polymer per granule holding them together and so lower start compression upon curing. This compression increases as number of granules to polymer increases e.g. granule loading increases, up until the point where there becomes insufficient granules to provide conduction through the sample. This results in the start resistance going back up as seen at 0.25 loading fraction. These ideas are mirrored by the response times measured for exposures to THF vapour shown in figure 5.25.

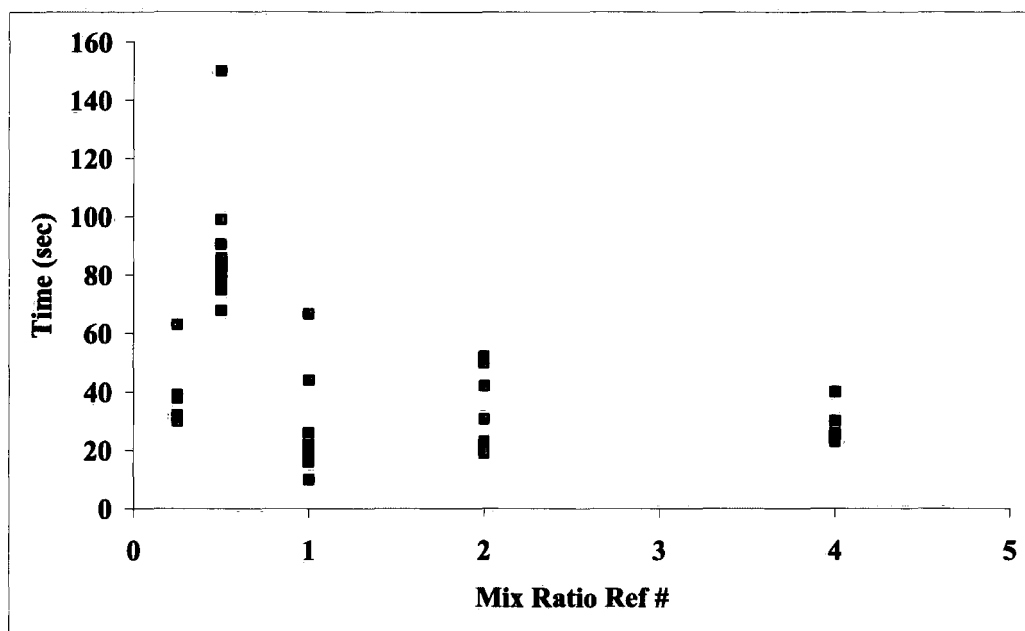


Figure 5.25: Response times of QTC vapour sensors as a function of Granule to Solution loading ratio.

Here there are shorter response times at higher granules loadings, which become longer as granule loading decreases. The longest response times correspond to 0.5 loading which also gave the very low start resistances. There is then a slower response time for the lowest granule loading. These overall results agree with the idea discussed previously regarding the amount of binding polymer in relation to the amount of granules, with the additional variable of very low granule loading providing poor conduction. It was also found that at high granule loadings that adhesion of the polymer was affected, with samples become very easy to dislodge from the electrodes. This was attributed to the small relative amounts of binding polymer in contact to create the adhesion required for the samples to stick.

Results from polymer to solvent ratios and granule to solution ratios lead to strengthen the idea that response of samples is strongly linked to the amount of binding provided by the additional relative amount of polymer and therefore the initial start resistance of the samples. Start resistance to response time for all the data examined in this section is plotted in figure 5.26. It can clearly be seen that there is a linear trend on the log-log scale that corresponds to the same trend in

figure 5.23 between points A and B The sensitivity of the sensors, based on the indications provided by response time, increases as start resistance increases.

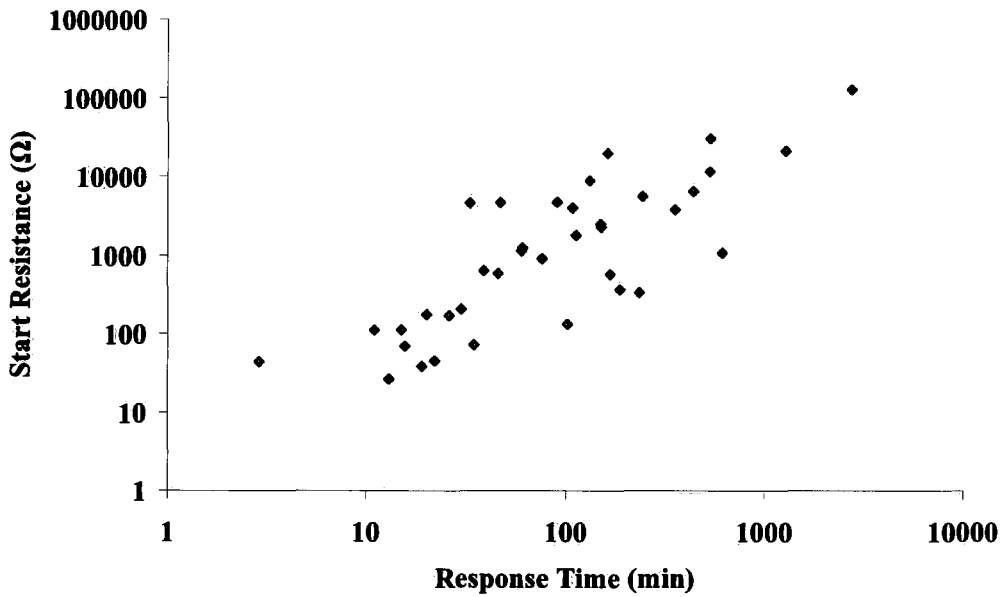


Figure 5.26: Response time as a function of start resistance for all the above experiments

The final stage of evaluation was to decide upon the optimum ratios to use. This was achieved through use of all the data shown in figures 5.21 through to 5.26. The final figure 5.26 indicates that the fastest response times occur in the start resistance range from 40 to 100 Ω . Relating this back to figure 5.21 this range was achieved for loadings between 0.1 and 0.15 ratios. Looking then at figure 5.22 both of these ratios gave the same average fast response time. Based upon these results either ratio was appropriate. The ratio of 0.1 was chosen based on manufacturing ease, the solution created being slightly thicker and easier to work with in the later stages of production. Figure 5.24 indicates a start resistance between 40 and 100 Ω is produced using a 1:1 loading (1.0) of granules. Figure 5.25 shows a fast response time at this loading ratio. Therefore a 1:1 ratio was identified as the optimum granule loading ratio, coupled with a Polymer to solvent ratio of 1:10.

Polymer Type

Four polymer types were investigated in this study for their response to 4133 PPM of THF solvent vapour. They were PS #2, PS #4, PPO and PVC. In addition to start resistance the peak response magnitude was measured for each exposure, this was possible because of the low test vapour concentration. The solubility parameters for the four polymers are as given in table 5.7.

Material	Solubility Parameter ($\delta = (\text{cal/cm}^3)^{1/2}$)
Polystyrene-b-polyisoprene-b-polystyrene	8.56
Polyvinyl chloride	9.75
Polyphenylene oxide	9.22
Tetrahydrofuran (THF)	9.52

Table 5.7: Solubility parameters for the polymer types used here and the THF test vapour

As a preliminary to the main analysis, data from PS #2 and PS #4, responses were examined. It was found that the two polystyrene based samples exhibited very similar characteristics. In order to allocate more time to later experiments it was decided that only one of these polystyrene samples would be examined further. From the data already collected in earlier experiments figure 5.27 shows the response times of PS #2 and PS #4 samples as a function of start resistance for exposures to THF vapour at 4133 ppm. This shows clearly that PS #2 based samples all fall within the required 40 to 100 Ω start resistance and as a consequence exhibit faster response times. Therefore PS #2 was chosen to compare response characteristics against PVC and PPO based samples.

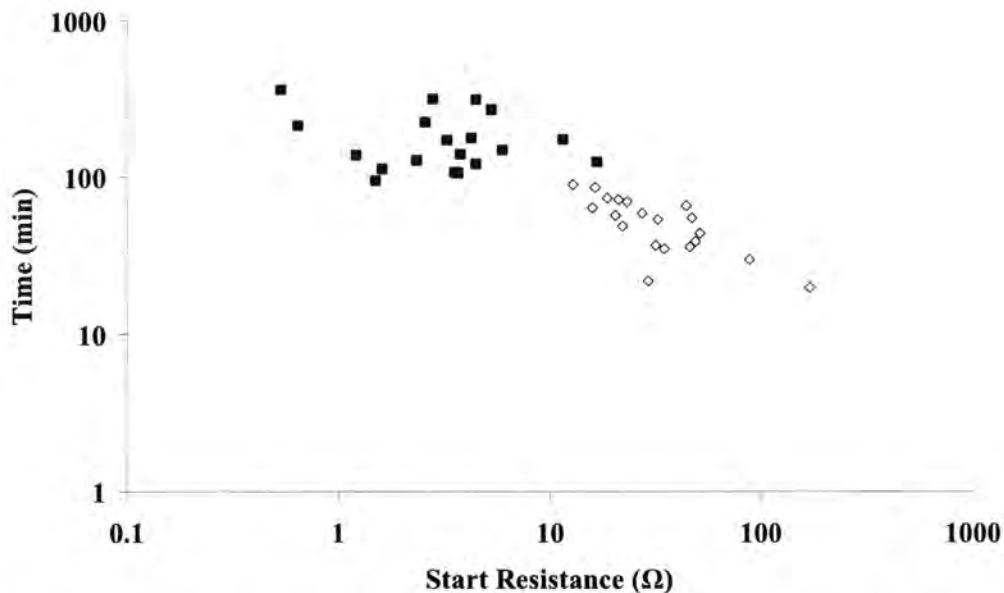


Figure 5.27: Response characteristics of PS #2 and PS #4, \diamond = Polymer 2, \blacksquare = Polymer 4.

The main experiments for this section involve direct comparison of PS #2, PVC and PPO responses to 4133 ppm of THF vapour. The average start resistances of the three polymer types are shown in figure 5.28.

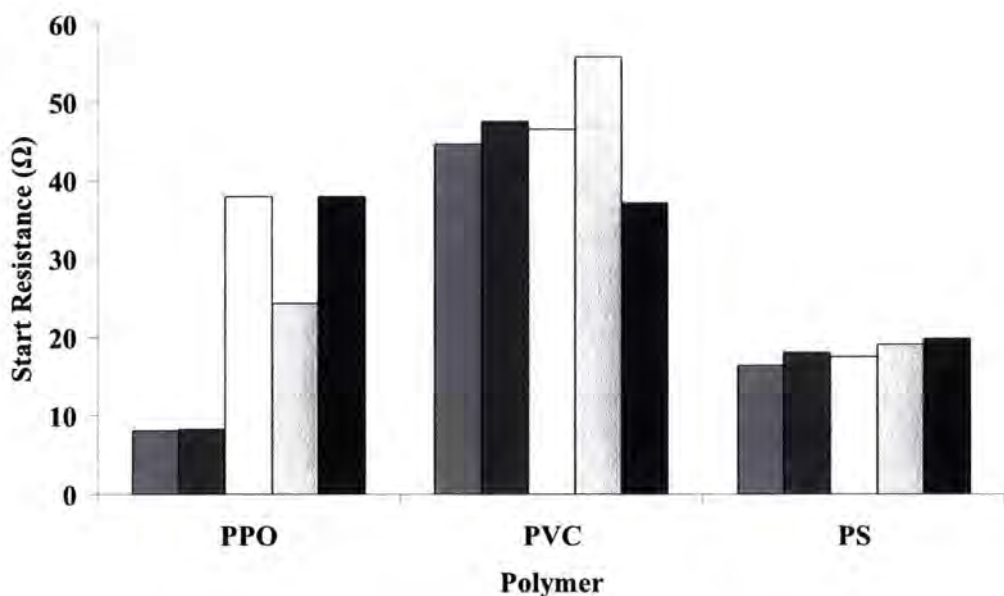


Figure 5.28: Start resistance of different samples used

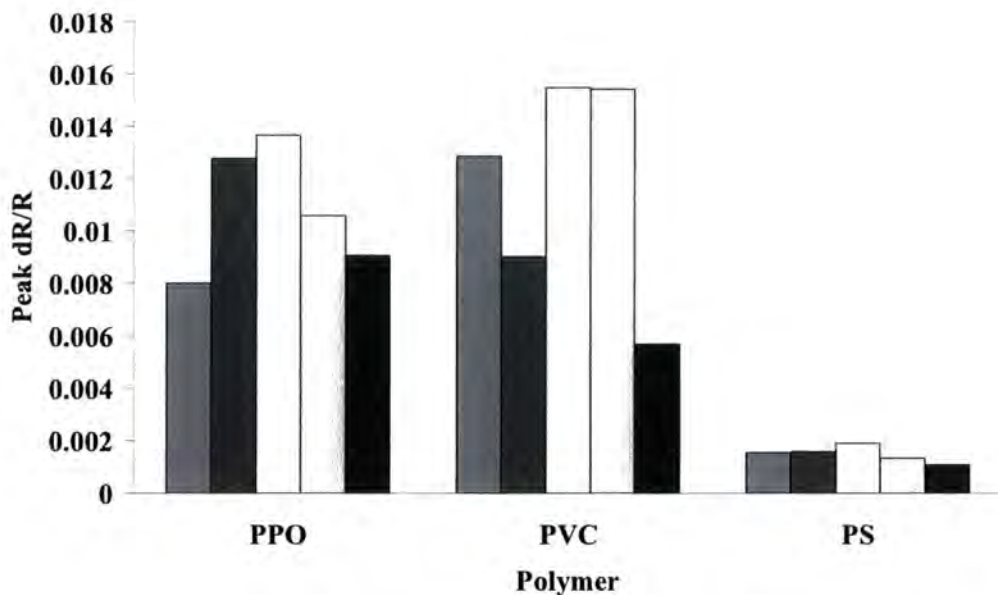


Figure 5.29: Normalised peak response to THF test vapour

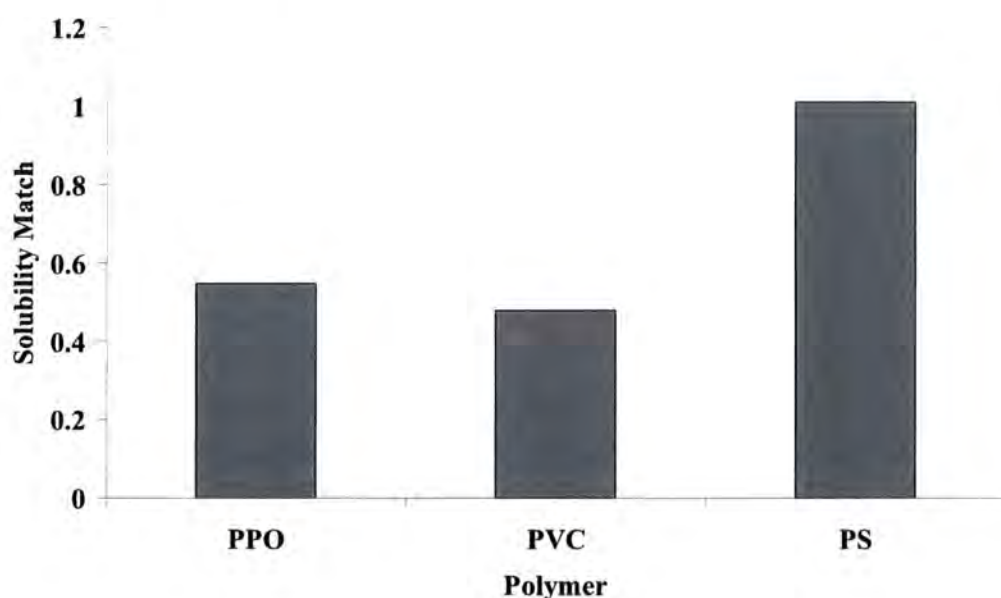


Figure 5.30: Solubility match values for polymers used compared to THF vapour

Figures 5.29 and 5.30 show normalized response and solubility match values respectively for the three polymers used. Start resistances were maintained as close as possible to the optimized values calculated earlier. They were then used to calculate the relative peak responses as shown in figure 5.29. The solubility match values shown in figure 5.30 were calculated using the data shown in table

5.7 and equation 4.8. The comparison of data in figures 5.29 and 5.30 show clear correlation between solubility match and response to vapour. It can be seen that for PS #2 there is a relative mismatch in solubility parameter compared to that of the THF, which relates to a much smaller relative response to vapour. The PVC and PPO samples however both indicate a much nearer match in solubility parameters to THF and as a result both have greater response to THF vapour. It can therefore be surmised from this data that choice of polymer type for specific vapour sensing applications can be achieved by calculating the solubility match between the polymer and solvent combination.

One practical problem that arose during these experiments was the cracking and physical breakup of some of the PPO samples. As will be discussed in more detail later, PPO has a much more rigid polymer chain structure. Thus upon curing as part of a solution it is prone to fracture and cracking. This in turn leads to very poor surface adhesion of the samples. It was seen that on a number of occasions that PPO samples would simply slide off the sample board surfaces. This phenomenon meant that the PPO samples would be unsuitable for any large scale productions as a large percentage of the manufactured sensors would exhibit this problem.

Polyurethane based Granules

Before proceeding to the environmental response experiments the use of a different type of QTC granule was investigated. Previous work by Hands [12] was carried out using Polyurethane based QTC samples, these were found to show very good response characteristics when exposed to test vapours using the old regime of granules compressed physically between two porous electrical contacts.

Inherently conductive samples were therefore produced and tested as described earlier. Figure 5.31 shows the response time as a function of start resistance for the Polyurethane samples exposed to 16950 ppm of THF solvent vapour. It can be seen that the response times of the Polyurethane based samples show similar

response times to the equivalent silicone rubber based samples in the lower start resistance region.

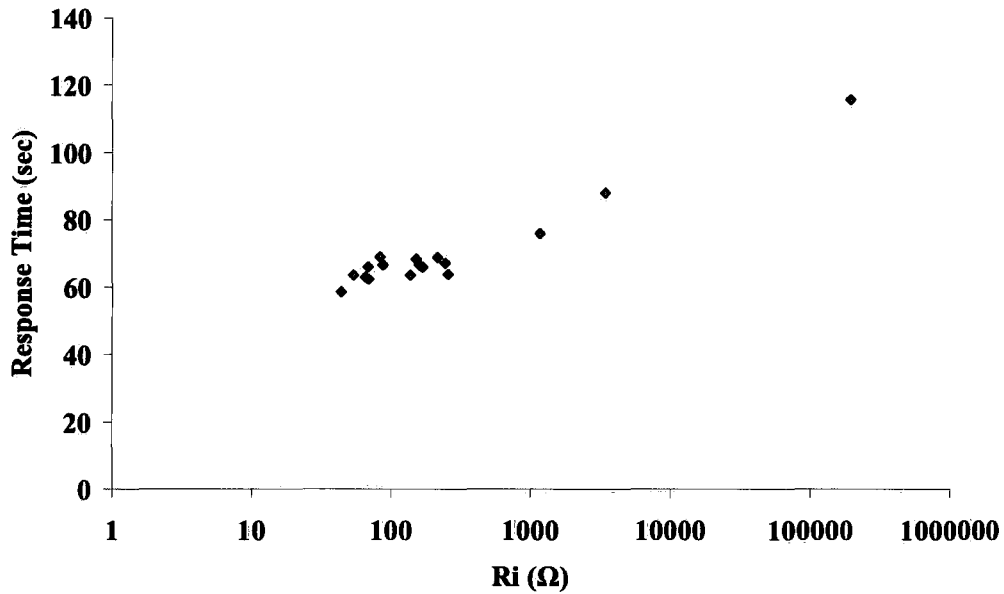


Figure 5.31: Response time as a function of start resistance for Polyurethane based granules

An increase of response time with start resistance is also seen. However the response times and higher start resistances are significantly less than those of the silicone samples. The data for this last observation is limited, but significant enough to warrant possible further research at a later date.

For the remaining experiments in this report samples were made using silicone based QTC granules with sample composition providing a start resistance between 40 and 100 Ω . Polyurethane based samples in this range provided no improvement to response time.

5.6.3 Environmental Response

The final stages of this research are to investigate how the QTC vapour sensors respond to different environments. In this study the two environmental response will be temperature and concentration of test vapour exposed to the samples.

Temperature Response

In many applications temperature response of a sensor is an important variable; even changes from day to night may cause sufficient sensor variation to be significant. The QTC vapour sensors are polymer based and so likely to have large temperature expansion coefficients. It has been seen throughout earlier experiments that there have been drifts in baseline trends that match to the temperature drift within the sample chambers over the course of experiments. As the sample chambers are held at 20 °C by the incubator, it is thought that the temperature variation seen in many experiments is a result of fluctuations in the Nitrogen carrier gas. The Nitrogen supply is piped into the lab from a boil off source and travels a significant distance between. It is likely that its temperature is affected by ambient temperature of the building over the course of its journey. Based on the observations of temperature dependence seen in these earlier experiments it was thought prudent to conduct some experiments to investigate temperature effects under controlled conditions.

Three different sample types were investigated based on three Polymer types, Polystyrene, PPO and PVC. Resistances were recorded as a function of Temperature change from room temperature to 80 °C. Five samples of each type were tested. However two of the Styrene samples experienced experimental failure and so their data was omitted. Figure 5.32 shows a typical temperature response of one of the QTC vapour sensors. It was seen that the general trend of all the responses recorded were of this form, although the degree to which the polymers recovered as temperature was reduced again did vary, this was

attributed to stress relaxation occurring at higher temperatures. For the purposes of this experiment though only the response on the up sweep was of interest.

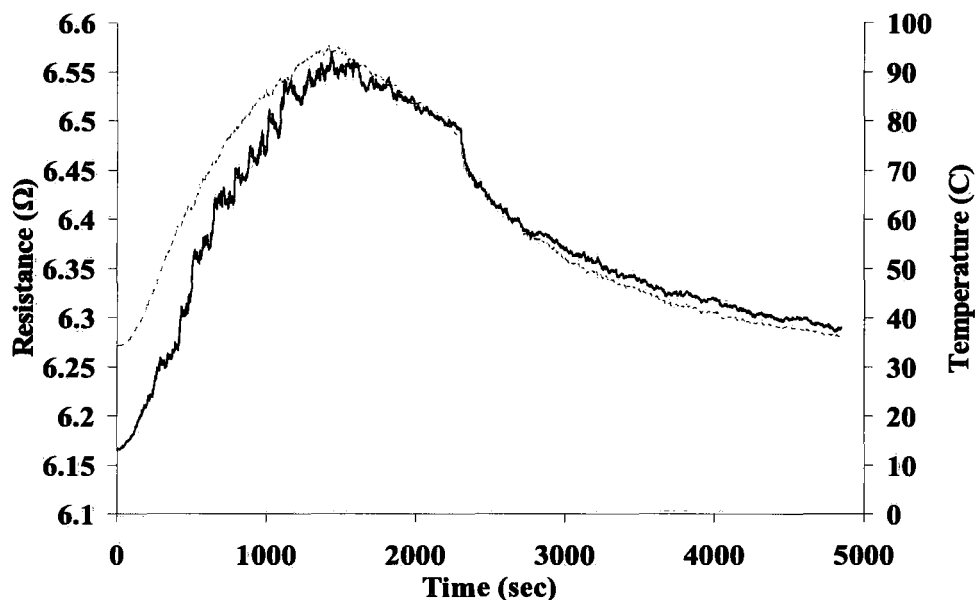


Figure 5.32: Temperature response of a PPO based QTC Vapour Sensor, showing QTC resistance (Solid) and measured temperature (dashed)

From figure 5.32 it can be seen that the QTC sensors resistance trend follows the temperature very closely. This is a trend seen through out all 15 of the temperature experiments. It is pertinent to therefore describe the trends for each polymer in terms of their thermal expansion coefficient, α . This is a measure of the relative change in length of a material with respect to a corresponding change in temperature, equation 5.1. °C

$$\alpha = \frac{dl}{l} / dT \quad \text{Eqn. 5.1}$$

It has been discussed through out this thesis that there is an exponential dependence of sample resistance to compression. Thus resistance change plotted on a logarithmic scale for QTC shows the same trends as plotting its change in length on a linear scale. Figure 5.33 below shows the calculated thermal expansion coefficients in terms of dR/R , but plotted logarithmically to give the same trends as a regular length scale based model as described in equation 15.

These values compare well to the book values for linear thermal expansion coefficients of the three materials given in [99]. These were; PVC 60, PPO 50 and PS 80 with units ($\times 10^{-6} / K$).

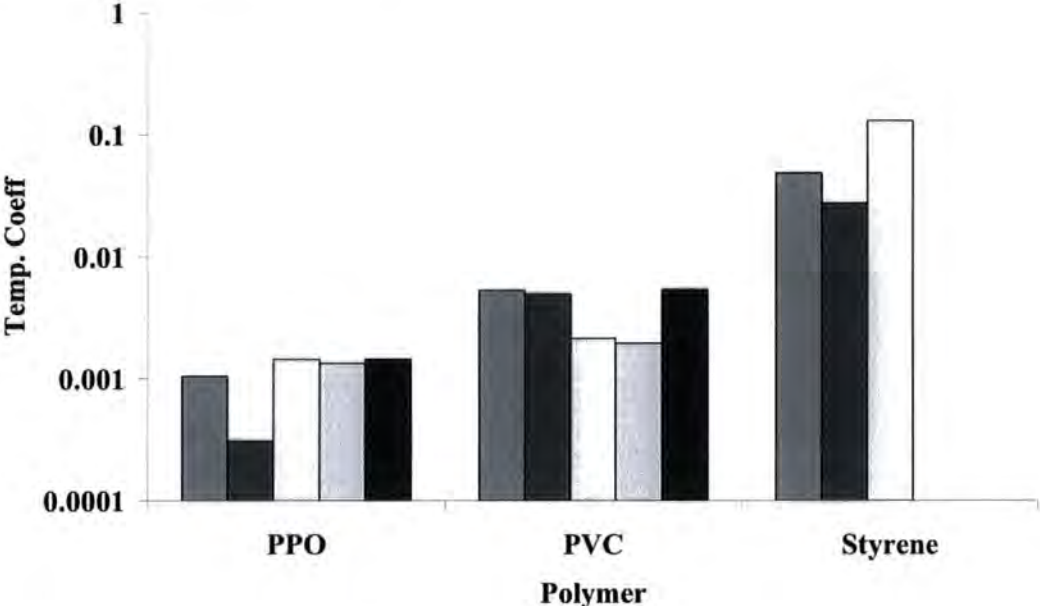


Figure 5.33: Thermal Coefficients for different polymer based QTC vapour sensors

The data shows that the polystyrene based sensors were far more temperature sensitive than the PVC which in turn was more sensitive than PPO. The pattern seen can be linked nicely with the inter-molecular structures of the Polymers that make up the samples. Polystyrene is a very visco-elastic polymer. There are few inter molecular bonds between its component polymer chains. Furthermore the polyisoprene block components to the polymer chain are an inherently rubbery material that vastly increases the viscoelasticity of the polystyrene chains. It is these qualities that make it the polystyrene elastic in nature and so requires less thermal energy to expand the material as little resistance is provided by the structure.

PVC however is a much more rigid polymer. Its polymer chains are packed much closer together allowed for by its tight organized chain structure, figure 5.34. This makes it more difficult for the polymer to expand as there is greater resistance between adjacent chains. PVC can be made more elastic by the

addition of plasticizers which separate the polymer chains of the material slightly allowing for easier movement between them and a reduction in stiffness.

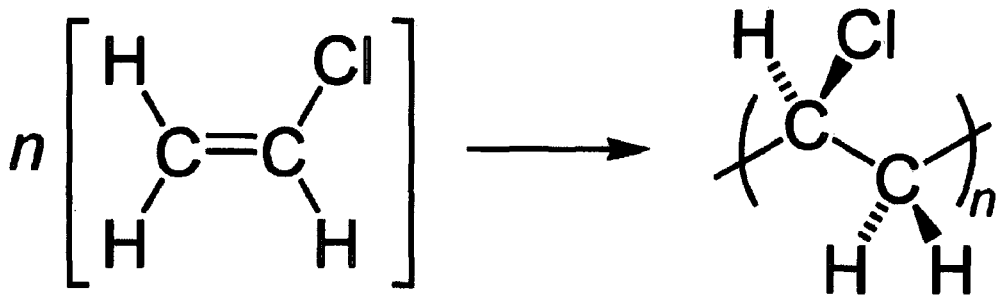
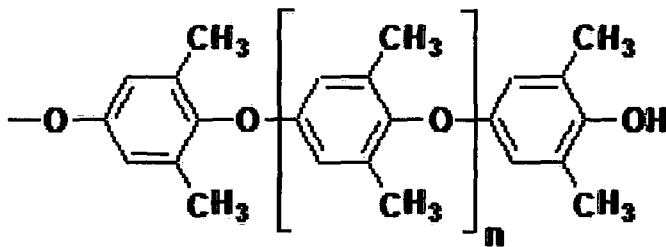


Figure 5.34: Polymerization and molecular structure of a PVC polymer chain

PPO has a structure comprising a benzene ring as part of its polymer chains, figure 5.35. These rings severely restrict inter molecular movement and create a very rigid and brittle polymer chain. Although this makes it very resistant to temperature change, one of the main reasons it was originally designed, however its resistance to temperature comes at the price of being very brittle, explaining the surface cracking and adhesion issues seen in earlier experiments.



Polyphenylene Oxide (PPO)

Figure 5.35: Molecular structure of PPO

These trends are closely linked to the solubility parameters discussed earlier, since materials solubility parameters are a measure of the intermolecular attractive forces, which will include the effects of structural differences between the polymer chains governing thermal expansion. A polymer with a greater solubility parameter has greater intermolecular forces, and so intuitively will require more kinetic energy for the system to expand. It should be noted that the

response to specific vapours is dependant on solubility parameter matching between the two substances, where as thermal effects are directly related to the molecular properties of each individual polymer.

Concentration Response

The final round of experiments on QTC vapour sensors was to investigate the response to a wide range of concentrations. This task was conducted using both PVC and PS #2 based samples. The figure 5.36 shows the average response of a number of repeat exposures of PS #2 based samples exposed to THF solvent vapour over a concentration range of 22 ppm to 105239 ppm.

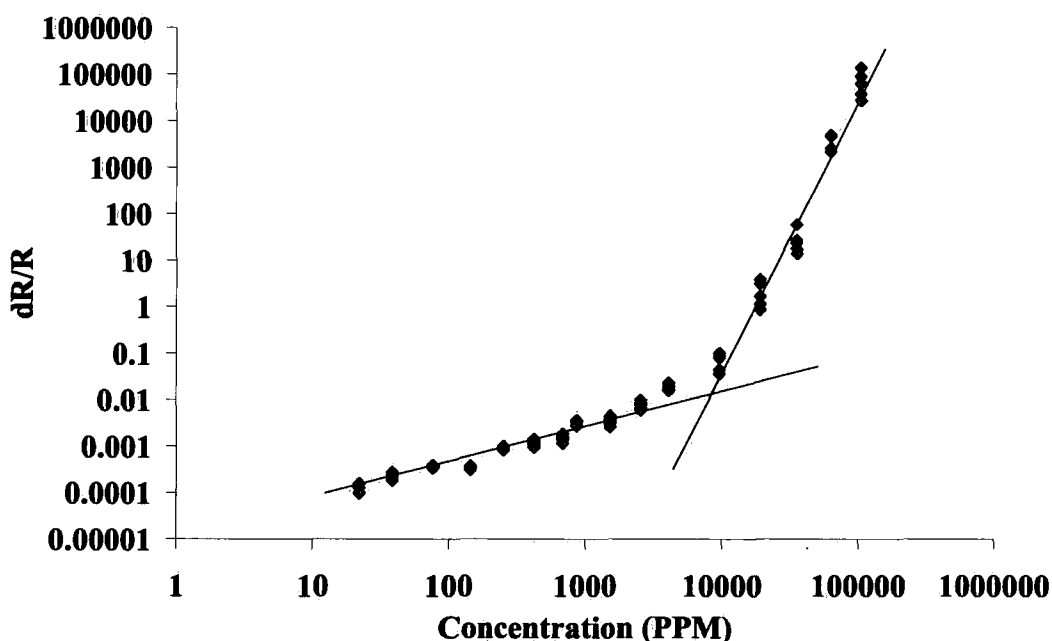


Figure 5.36: Relative response of Polymer #2 QTC vapours as a function of THF test vapour concentration

The graph shows two distinct trends in the data, a “low concentration” region, (<10,000 ppm) and a “high concentration” region, (>10,000 ppm). Figure 5.37 shows a similar data set for the PVC based samples. Here the same two trends are evident. This suggests that the trends relate to the fundamental absorption physics rather than any polymer specific attributes.

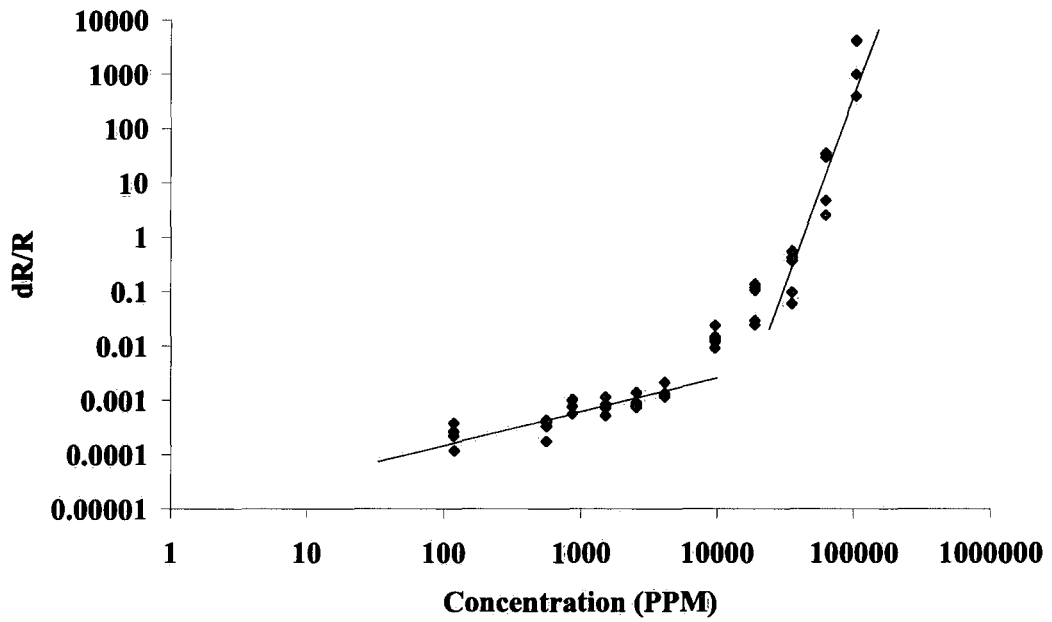


Figure 5.37: Relative response of PVC QTC vapours as a function of THF test vapour concentration

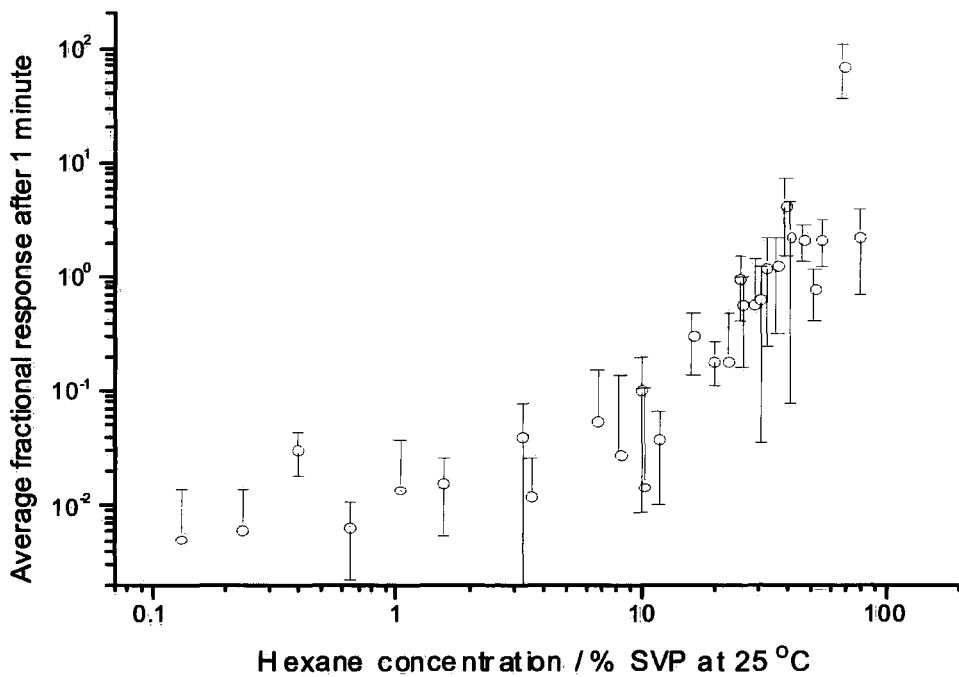


Fig. 5.38: Sensitivity of compressed silicone QTC granules [12]

Figure 5.38 shows data measured by Hands [12] displaying the response characteristics of compressed silicone granules to a range of Hexane concentrations. This was taken using the previous test regime described in Chapter 1. This data is presented here in order to provide further indication of the two stage mechanisms thought to be present.

In order to investigate more fully the mechanisms behind the two trends, individual responses characteristics were examined. These temporal responses were carried out at eight different concentrations. The four high concentration temporal responses are shown in figure 5.39. Examining the response of data from the 105239 ppm exposure it can be seen that there is a region up to about 30 seconds that matches the wave front properties described by the Case-II diffusion model. This then leads into a linear response against root time with no concentration gradient behind it, consistent with Fickian diffusion as described in section 4.3, and also described by the Case-II diffusion model, section 4.6 earlier in this thesis. It should be noted that Case-II relates swelling to time, whereas figure 5.39 shows resistance as a function of time. As discussed earlier there is an exponential dependence between swelling and resistance change afforded by the Fowler-Nordheim tunnelling conduction mechanism. Therefore the y-axis plotted on a log scale in figure 5.37 and 5.38 represents a linear trend in swelling.

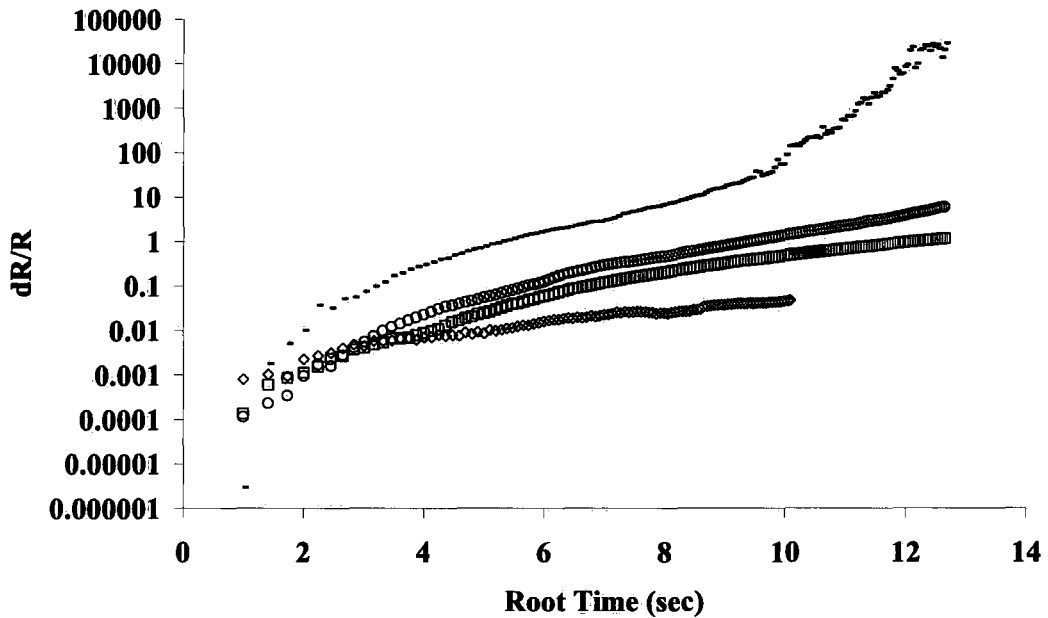


Figure 5.39: Temporal response of sample resistance upon exposure to “high concentration” THF vapour, \diamond = 9631 ppm, \square = 19102 ppm, \circ = 35561 ppm and - = 105239 ppm.

In order to further justify the relation to Case-II diffusion, data published by Hui [81] showing the profiles of iso-hexane wave-front progression through polystyrene can be compared. Figure 5.40 shows data extracted from this publication. The profile shows the same wave-front characteristics to the temporal response characteristics of QTC shown in figure 5.39.

The temporal response characteristics of QTC sensors are seen to maintain the same Case-II trend down to the 9602 ppm exposure. Below this concentration level the Case-II model no longer fits. Figure 5.41 shows the temporal response data for the “low concentration” regime.

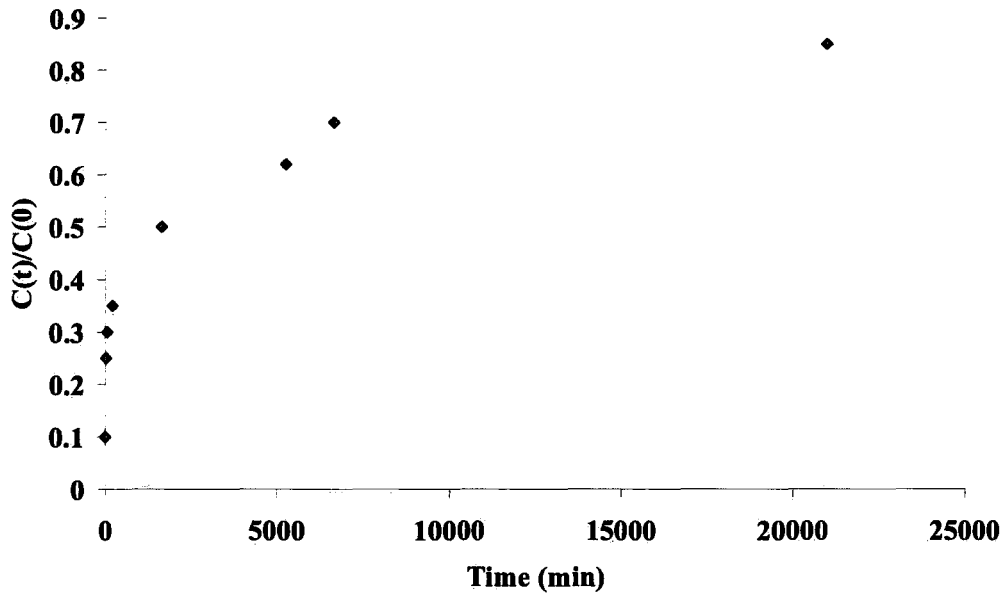


Figure 5.40: Data extracted from Hui [81] demonstrating Case-II behaviour

In figure 5.41 the data is presented with a linear y-axis scale against a root t x-axis, showing that in the low concentration regime there is a distinctly different diffusion mechanism in play highlighted by a linear in one data set and an exponential trend in the other.

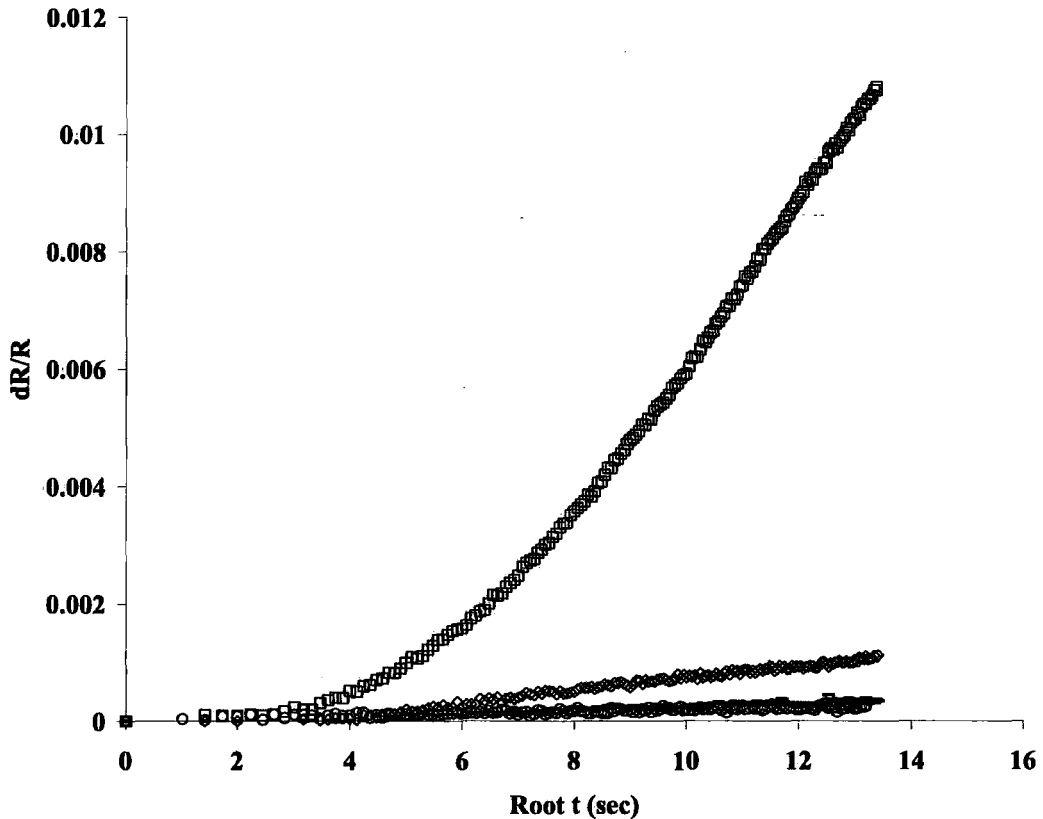


Figure 5.41: Temporal response of sample resistance upon exposure to “high concentration” THF vapour, \circ = 22 ppm, - = 144 ppm, \diamond = 688 ppm, \square = 4133 ppm

It is proposed that in the low concentration regime the conduction is not in fact a direct result of swelling in the polymer, but a result of changing dielectric permittivity, acting against the swelling induced resistance increase. The dielectric constant of the vapour analyte THF is 7.58, which is higher than that of the silicone rubber in the QTC sensor that is 2.81. Therefore upon absorption the polymer matrix experiences an induced permittivity increase. This decreases the energy barriers for charge transport and so acts as a counter to the resistance decrease caused by swelling. In order for this effect to occur there can only be a very small amount of swelling, with the absorbed analyte molecules filling voids within the polymer matrix to provide an effective increase in overall dielectric constant. As the concentration increases so will the swelling, countering the effects of the dielectric change. The void filling mechanism will remain dominant until the degree of swelling outweighs it. This change is thought to occur around 10,000 ppm for the QTC vapour sensors based on change in trends seen earlier. It can be seen in figures 5.36 and 5.37 that there is a gradual change

in response trend, leading to the conclusion that there is a steady change in physical mechanism. This corresponds to a gradual outweighing of dielectric change by swelling. This hypothesis is supported by similar work conducted on vapour absorbing conductive polymers by Krasteva et.al. [86], in their work they describe that above mechanism for dielectric effects to sample response.

The arguments presented above and also by Krasteva are mainly qualitative in nature. Further experiments in the next chapter aim to provide further evidence through QCM measurements of vapour absorption.

Figure 5.42 shows data extracted from work by Chen et al [87] who explored the effects of vapour pressure (analyte concentration) on electrical response of carbon black filled polyurethane. The data shows a transition between two regimes, similar to the effects seen in the QTC sensors seen in figure 5.36. The temporal plots for saturated vapour exposure presented in the same publication show similar response characteristics to those shown in figure 5.39 for high concentration THF exposure to QTC sensors.

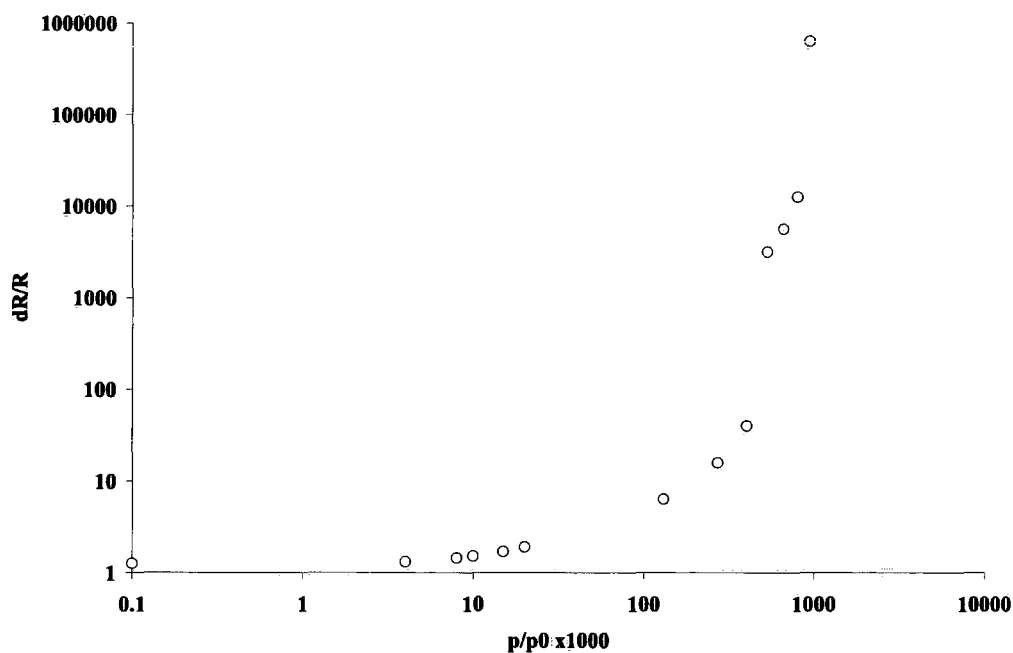


Figure 5.42: *Differential resistance change as a function of analyte partial pressure for a carbon black filled polyurethane gas sensor [87]*

Although not presented in this manner in the publication Chen does make comment on there being present two mechanisms governing the response of the material to different analyte concentrations, relating the high concentration data specifically to Case-II type diffusion. A specific mechanism for the lower regime is not provided. These results however do provide good comparison to the QTC vapour sensor responses and add to the validity of the mechanisms put forward in the explanations given above.

5.7 Conclusions to Vapour Sensing

Intrinsically conductive QTC vapour sensors provide a novel approach to solvent vapour detection using metal-polymer composites. QTC granules are bound together using a polymer solvent solution and cured onto a pair of electrodes creating a conductive sample.

It has been shown how composition and physical parameters can have an effect on the response characteristics of the QTC sensors. Characterisation experiments have produced a “best” composition formula for the sensors being used in this study. From these experiments it has been found a factor to provide a good QTC vapour sensor is its start resistance. It was found that sensors with a start resistance between 40 and 100 Ω produced the best response characteristics.

Experiments to compare different polymer types to THF showed that there was a correlation between the response magnitude and the degree of matching between the polymer and the test vapour. It was suggested from this that solubility parameters were a good starting point for choosing future polymers for response to specific vapours.

Temperature dependence of a range of polymer types was investigated. It was found that the degree of response to temperature was related to the molecular structure of the polymers, particularly the ability of chain molecules to move past each other. This phenomenon is closely related to the physics behind solubility parameters.

Response of QTC sensors was shown to vary significantly with test vapour concentration, providing promise for application in commercial devices. It was seen that two distinct regimes occurred. A high concentration regime was correlated to Case-II diffusion behaviour. The low concentration regime was attributed to dielectric changes induced by the absorbed vapour acting against the response to swelling.

Chapter 6, QCM Measurements

Introduction

A QCM200 made by SRS instruments was used to take same measurements to investigate the hypothesis presented in the final sections of the last chapter.

A Quartz crystal Microbalance (QCM) is a type of acoustic wave sensor whose technology can be applied to a large range of chemical and biological applications. In the case of this study the QCM will be used as a sensitive gravitational mass sensor to measure the mass uptake of solvent vapour by a polymer upon exposure.

A secondary function of the QCM200 is that it can simultaneously measure the series resistance of the crystal resonator providing additional data from which density of the polymer layer can also be inferred. It is the aim of this final investigation to verify the previous theories relating to the low concentration responses of QTC vapour sensors.

A discussion on QCM operation, the physics behind their operation and relevant theoretical models will be presented. A discussion of the experiments undertaken using the QCM will be provided followed by an analysis of the results obtained relating them to theory and also the results obtained by the QTC sensors.

6.1 Models and Theory of Quartz Crystal Microbalances

For many years QCMs were simply regarded as gas-phase mass detectors. However more recently they have been developed to include operation when in contact with liquids and viscoelastic deposits. In the latter case both the resonant frequency and the series resistance of the quartz oscillator are important to fully characterise the material being measured. Developments have been made so that electrode surface chemistry, i.e. the use of specific polymer surface coatings, is tailored to provide discriminating mass detectors for a number of applications including, specific gas detection, environmental testing and bio-sensing.

Sauerbrey was the first to recognise that the Quartz Crystal Microbalance (QCM) has some very useful technological applications, using the sensitive nature of the piezoelectric response in the quartz crystal to detect mass changes on the electrode surfaces [88]. The results of his work are summarised in his equation, which relates the mass change per unit area of the quartz crystal electrode to the observed change in oscillation frequency of the crystal. The Sauerbrey equation [89] is shown below, equation 6.1.

$$\Delta f = -C_f \cdot \Delta m \qquad \text{Eqn 6.1}$$

Where Δf is the observed frequency change measured in *Hz*, Δm is the change in mass per unit area measured in gcm^{-2} , and C_f is the sensitivity factor which is a constant relating to the fundamental properties of the quartz crystal being used. The sensitivity factor is discussed in more detail below.

The Sauerbrey equation relies on a constant sensitivity factor, thus in theory when being used to measure simply mass uptake a QCM should not need to be calibrated provided the sensitivity factor of the crystal being used is known. However it must be noted that the equation is only applicable to a rigid thin film deposit. Measurement of non-rigid deposits, such as thin film polymers, departs from the accuracy of the equation. In general for most thin films the assumption is made that the incremental change in mass from the foreign film is treated as

though it is an extension of the underlying quartz. The foreign film can be assumed rigid provided that it does not experience any shear forces during vibration. This can be achieved for polymer layers by using a very thin (less than 1 micron) film thickness [89]. As a result the sensitivity factor can still be regarded as a fundamental property of just the quartz crystal and does not need to include any properties of the foreign film. The sensitivity factor can be calculated from the crystal's properties as given in equation 6.2.

$$C_f = \frac{2nf_o^2}{(\rho_q\mu_q)^{1/2}} \quad \text{Eqn 6.2}$$

Where, n is the number of the harmonic at which the crystal is driven, f_o is the resonant frequency of the fundamental mode of the crystal, ρ_q is the density of quartz and μ_q is the shear modulus of quartz. The dependence of the frequency change on mass change per unit area emphasises that the sensitivity factor is independent of electrode geometry as well as foreign film properties within limitations. It is generally accepted that if the mass loading from a deposit causes a change in frequency of less than 2%, the Sauerbrey equation will provide accurate results [90]. The sensitivity factor for the quartz crystals used in the QCM200 provided by SRS components is $56.6 \text{ Hz}\mu\text{g}^{-1}\text{cm}^2$ at 5 MHz.

Basic QCM Oscillator Circuit

Basic QCM measurements take place using a resonant frequency measurement of a quartz crystal. The crystal forms part of an electronic circuit that is integral to the operation of the device. The circuit can be modelled in simplistic terms using the Butterworth-van Dyke (BVD) electrical model [91]. The circuit diagram for the BVD model of a quartz crystal resonator is shown in figure 6.1.

The BVD model consists of two arms. The motional (lower) arm has three series components that are modified with the application of mass or change in the viscous loading of the crystal. These components are described in detail as follows:

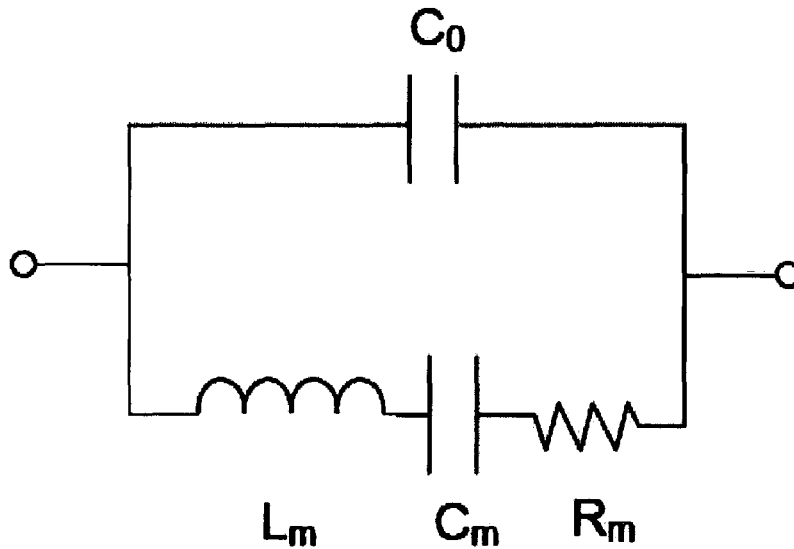


Figure 6.1: *The BVD model of a QC resonator circuit*

R_m (resistor) corresponds to the dissipation of the oscillation energy from mounting structures and from the medium in contact with the crystal, losses induced by a viscous solution or polymer layer.

C_m (capacitor) corresponds to the stored energy in the oscillation and is related to the elasticity of the quartz and the surrounding medium

L_m (inductor) corresponds to the inherent component of the oscillation; this is related to the mass displaced during vibration.

The motion arm is then shunted by the second (upper) arm in the circuit. This arm contains only the parasitic capacitance C_o , which represents the sum of the static capacitances of the crystal's electrodes, holder, and connector capacitances. A typical value for the C_o is of order 20 pF.

The parasitic capacitance mentioned above can be removed by the QCM200 via a method of nulling. This ensures that the frequency and resistance values measured correspond to the true values of the quartz crystal. This is essential when measuring liquids and lossy (soft) films.

Liquid Contact Measurements and Series Resistance

Viscous coupling of the liquid medium to the oscillating crystal surface results in a decrease in series resonant frequency and also a damping of the resonant oscillation. A viscous loss is manifested as an increase in series resonant resistance of the QCM resonator. Thus the series resistance serves as a measurement of viscous loading of the quartz crystal by a liquid or soft film that is independent of the frequency measurements.

It is therefore the case that both ΔR and Δf measurements are both used in order to indicate mass loading and viscosity of a surface layer that is in contact with a liquid or vapour making chemical and electrochemical depositions on or into the surface layer [92].

In separate studies [93] a BVD equivalent circuit model was applied to derive a linear relationship between the change in series resistance, ΔR , and $(\rho_L \eta_L)^{1/2}$.

This relationship is given by equation 6.3.

$$\Delta R = \left(\frac{n \omega_s L_u}{\pi} \right) \left(\frac{2 \omega_s \rho_L \eta_L}{\rho_q \mu_q} \right)^{1/2} \quad \text{Eqn 6.3}$$

The terms in equation 6.3 are given as follows:

- ΔR = change in series resistance of the resonant circuit (Ω)
- n = number of sides in contact with liquid/vapour (usually 1)
- ω_s = angular frequency at resonance ($2\pi fs$)
- L_u = inductance for a dry resonator (mH)
- ρ_L = density of contact liquid or polymer
- η_L = viscosity of contact liquid or polymer
- ρ_q = density of quartz
- μ_q = shear modulus of quartz

Since the majority of these are simply measurable quantities and not variables within the equation, an indication of effects of ΔR can be made, equation 6.4.

$$\Delta R \propto (\eta, \rho)^{1/2}$$

Eqn 6.4

Work by Lee et al [94] shows that the density of a viscous solution or gel increases with viscosity. Evidence and experimental data is presented that verifies equation 6.4. It is shown also that density change and viscosity change both act in the same sense. Thus as there is an increase in ΔR there is an increase in both viscosity and density, rather than the two properties acting against each other with a dominant factor giving rise to a trend. This is important as it allows a reasonable assumption that the basic trends seen in the $\rho_L \eta_L$ data to be indicative of the density of the material. For further discussion on the viscoelastic and density properties of swollen polymers the reader is directed to [94-96].

flow is directed down into the centre of the sample and flows radially outwards over the surface.

The control unit is the core of the sensor kit, figure 6.3. It provides a signal at 5 MHz to the crystal via the holder. The control unit is capable of measuring changes in the crystal resonant frequency to an accuracy of 1 Hz.



Figure 6.3: QCM200 control unit and sensor unit

It can also measure the series resistance of the resonance circuit to an accuracy of 0.001Ω for resistance values under 100Ω . The control unit also has a capacitance null built into it, which as described earlier is essential to obtain true readings of the sample. The offset null is adjusted for each new sample loaded into the equipment.

The control unit is interfaced with a PC via an Ethernet connection and the measurements made by the QCM are recorded using a LabView program provided by SRS. The sample with the enclosed hood was connected inline with the vapour sensor rig, connected between the electronic solenoid valve and the QTC vapour sensor chambers. This provided the facility to simultaneously record QCM and QTC response to exposures of test vapour. The timing and degree of exposures could also be controlled using the earlier mentioned LabView program.

6.3 Methodology

A series of experiments were setup to investigate the mass uptake of solvent vapour by a polymer layer over a range of vapour concentrations. Due to time constraints it was only possible to look at one of the polymer types investigated previously in the QTC vapour sensing work. It was decided to use Polystyrene-*b*-polyisoprene-*b*-polystyrene (PS #2) as the polymer to be investigated. This had the most conclusive set of concentration data from the previous chapter and a significant amount of work had been conducted using it. Due to the extreme sensitivity of the QCM the polymer was tested without any QTC granules mixed into it. During preliminary experiments it was found that the large quantities of nickel in a complete QTC solution increased the density of the polymer layer beyond the capabilities of the QCM200 at the layer thickness that was used for measurements.

The PS #2 sample was made by first dissolving bulk polymer pellets into toluene solvent. This solution was then spin coated onto the surface of the quartz crystal. The layer thickness of the polymer needed to be less than 1 micron, as described by the theory discussed earlier, in order for the Sauerbrey equation to hold when analysing results later. Using published work by Khalil et al [97], discussing accurate spin coating of polystyrene to specific thickness, it was found that a mixing of polymer to toluene 1.8% (w/v), e.g. 1.8 g to 100 ml and spin coated at 3000 rpm for 3 minutes would produce a 100 nm thick polymer layer. After spin coating a 100 nm layer onto the crystal surface the samples were left overnight for the polymer to cure.

The polymer coated crystal was then loaded into the QCM holder and the holder connected to the QCM200 control unit and also into the solvent gas lines between the solenoid valve and the QTC sample chambers. The QCM sample holder was mounted inside the same incubator as the QTC chambers to ensure its temperature remained constant. The whole setup was left to reach a thermal equilibrium with the rest of the incubator.

The sample was then exposed to THF solvent vapour for 5 minutes over 5 separate exposures with 5 minute purges of nitrogen between each. It was found that the purge flow rate used previously caused a pressure change that was detected by the QCM as a sharp frequency change. The nitrogen purge flow rate was therefore reduced and matched as close as possible to the solvent vapour flow rate to reduce this effect. Nitrogen Purging was reduced to 50 ml/min regulated by a third Cole-Palmer digital MFC. Even with this matching an almost instantaneous shift in frequency was still monitored in some results and had to be removed from any data prior to analysis.

A range of solvent vapour concentrations were exposed to the PS #2 coated crystal samples. These were from 200 ppm up to 105000 ppm with 12 increments between. A freshly spun quartz crystal with polymer layer was used for each data set at each concentration.

A set of PS #2 QTC vapour sensors were manufactured to the same specification as those used in the concentration tests discussed in chapter 6. The results from these sensors were used to provide direct comparison between QTC response and QCM response; furthermore it would allow direct comparison with the earlier QTC results already collected.

6.4 Results and Analysis

A range of concentrations from 200 ppm to 105000 ppm of THF test vapour were exposed to a Polystyrene-b-polyisoprene-b-polystyrene (PS #2) coated quartz crystal. The change in resonant frequency and the change in series resonance of each exposure were recorded. The mass uptake for each exposure was subsequently calculated using equation 6.1 and was then plotted as a function of solvent concentration, figure 6.4.

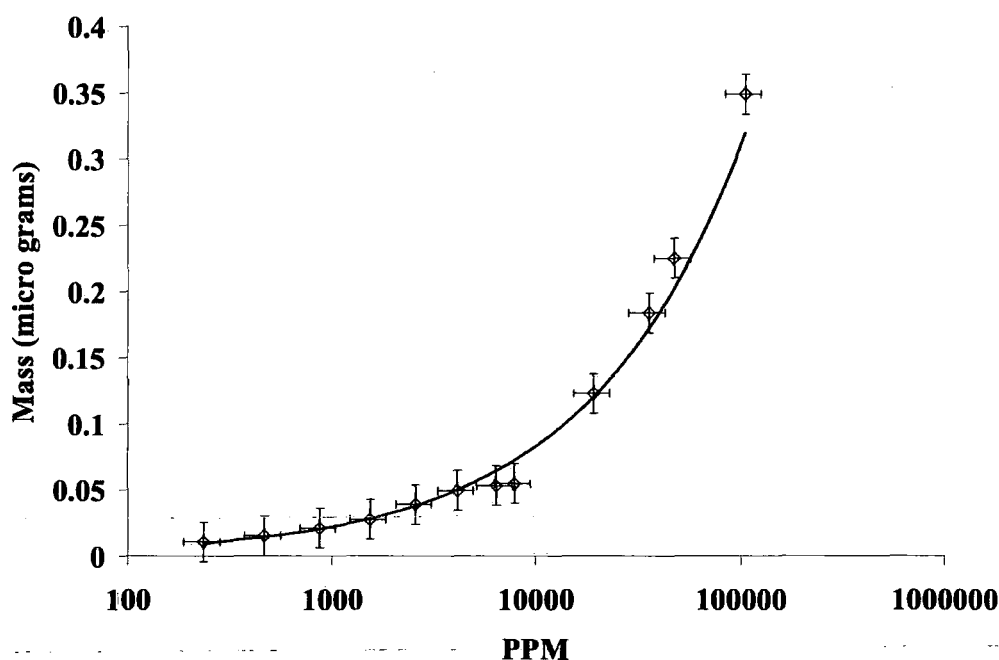


Figure 6.4: Mass uptake of PS #2 upon exposure to THF solvent vapour, \diamond = Data, Solid Line = power law fit

It can be seen in this data that a similar trend is present as to that seen in the electronic response of the QTC vapour sensors. Specifically there is a high concentration regime above 10,000 ppm and a low concentration regime below 10,000 ppm. However a single power law fit can be made to the whole data series too, which cannot be done to the QTC resistance responses discussed earlier. In order to further identify two separate regimes in the QCM data the series resistance was examined.

Figure 6.5 shows the respective $\rho_L \eta_L$ of the polymer layer based on application of equation 6.4 on the series resistance measurements. Recalling from section 6.1 that there is an increase in both density and viscosity with increasing resistance and that the two variables work in the same sense rather than as to oppose one another, the general $\rho_L \eta_L$ trend is indicative of the trend-given by the density change of the material.

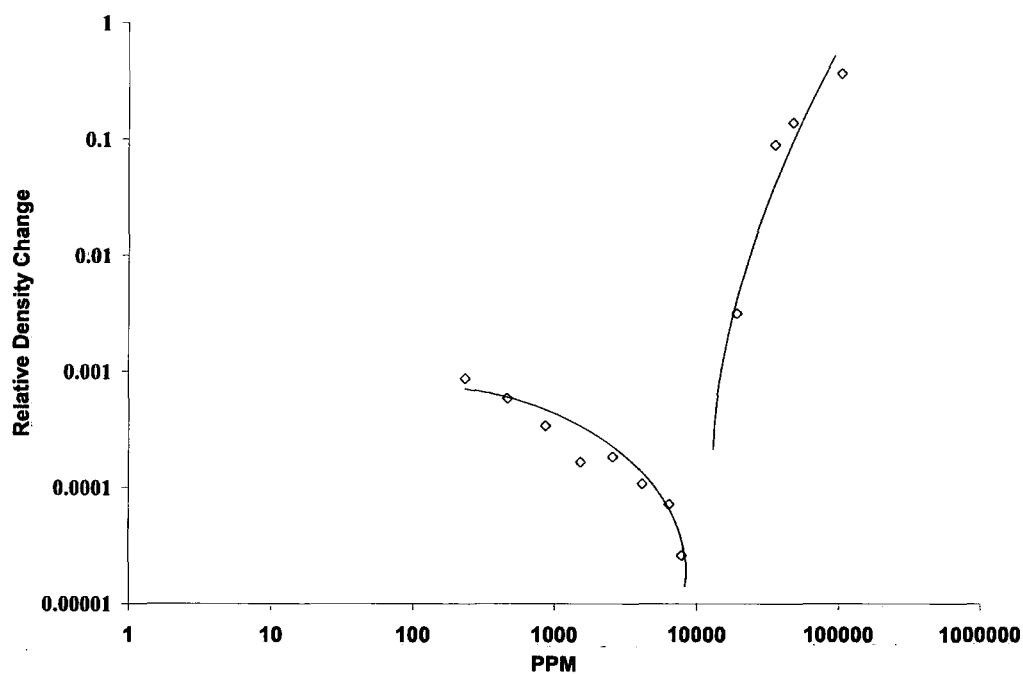


Figure 6.5: $\rho_L \eta_L$ values for PS #2 upon exposure to THF solvent vapour at different concentrations

This data highlights the two regimes in the response data. However there is a difference in the gradients between the two regimes. In the low concentration regime there is a decreasing gradient, with $\rho_L \eta_L$ becoming lower as concentration is increased. There then appears to be a turning point around the 10,000 ppm region and the gradient starts increasing as $\rho_L \eta_L$ also increases with increasing concentration.

The data does not intuitively match with the predicted theory of swelling mechanisms, specifically at high concentrations. An increasing $\rho_L \eta_L$ and so increasing density would imply no swelling, or even contraction. It is uncertain if this response, inverse to intuitive matching to theory, is a true indication of the

system or simply an artefact of the assumptions made by inferring the density values and mathematical processing. In order to allow correct interpretation of the data presented in figure 6.5 temporal responses of selected exposures were analysed. The response data for 466 ppm exposure was taken to examine data from the low regime and data for 19102 ppm exposure taken for the high regime.

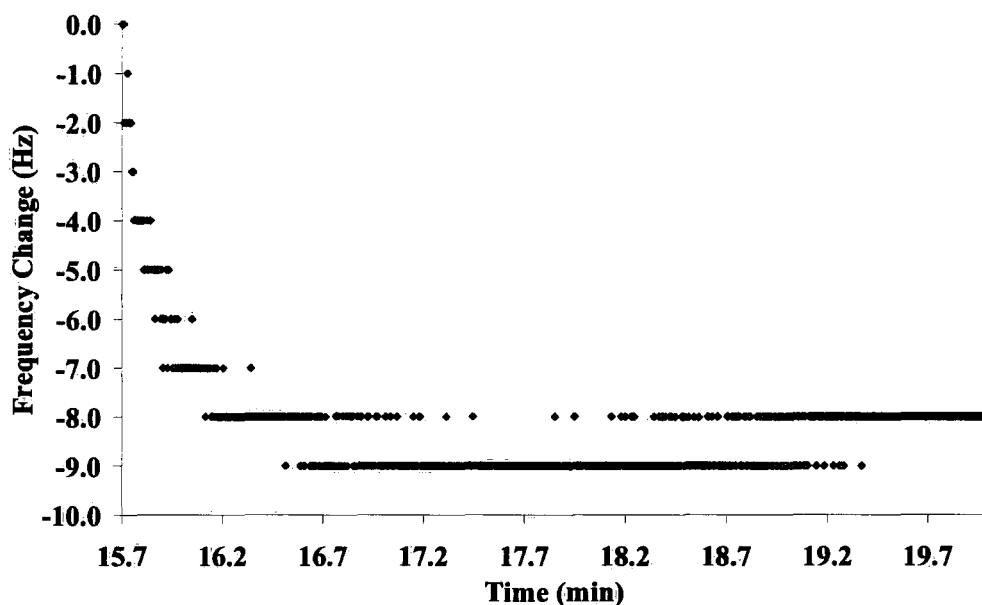


Figure 6.6: Mass uptake of a PS #2 exposed 19102 ppm of THF vapour

Looking first at the high concentration regime, figure 6.6, it can be seen that the frequency of the sample drops over time. This corresponds to a mass increase using the relation given in equation 6.1. This is as expected as the vapour molecules are absorbed into the polymer matrix. It is known from the QTC data earlier that at this concentration of exposed vapour that a Case-II diffusion process is occurring. It is reasonable to assume the same diffusion process is occurring here. Looking at the resistance data, in figure 6.7, there is a trend which matches that seen in the electrical response data from the QTC samples that was correlated to Case-II behaviour. This is not to be unexpected as the resistance is related to density of the polymer, which in turn is a measure of swelling, which is what Case-II diffusion theory describes. There is a sharp increase at first caused by the wave front staging, followed by a steadily increasing region of Fickian diffusion with no concentration gradient evident.

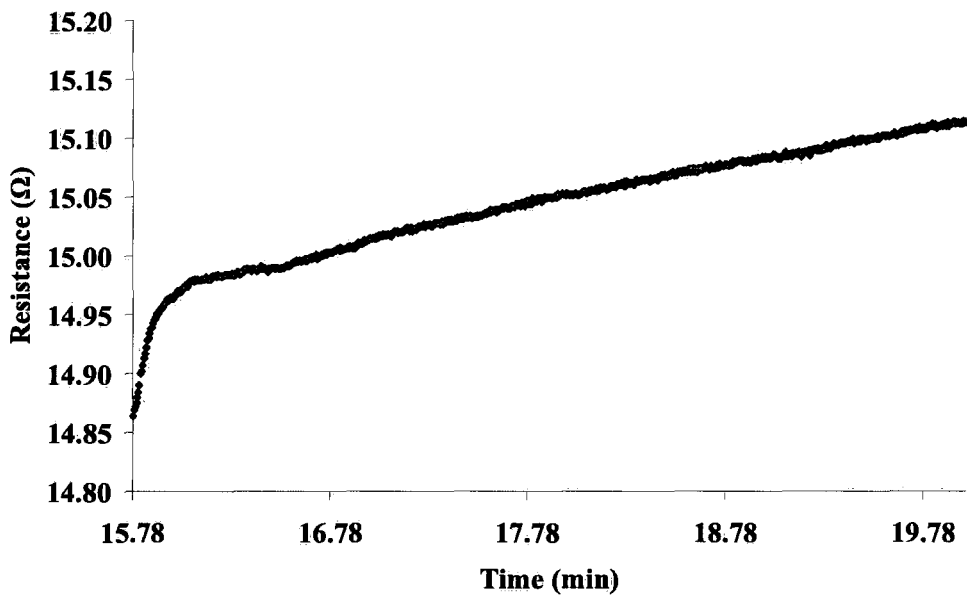


Figure 6.7: Series resistance of a PS #2 exposed 19102 ppm of THF vapour

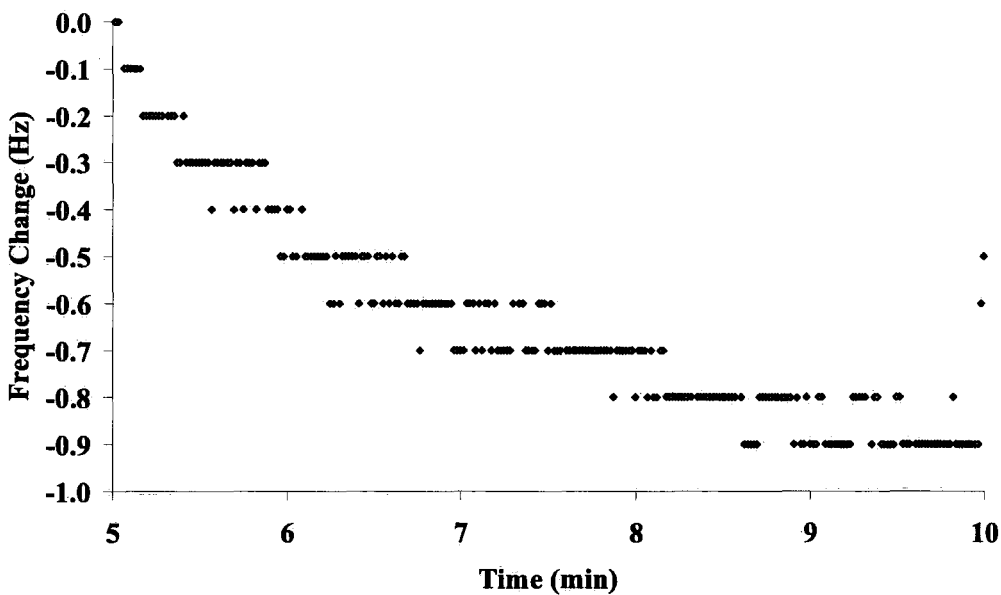


Figure 6.8: Mass uptake of a PS #2 exposed 466 ppm of THF vapour

The key feature to take in when looking at figures 6.6 and 6.7 is that there is an increasing resistance at the same time as there is an increasing mass uptake. However if this is then compared to similar data for the low concentration regime a different trend is seen, figures 6.8 and 6.9.

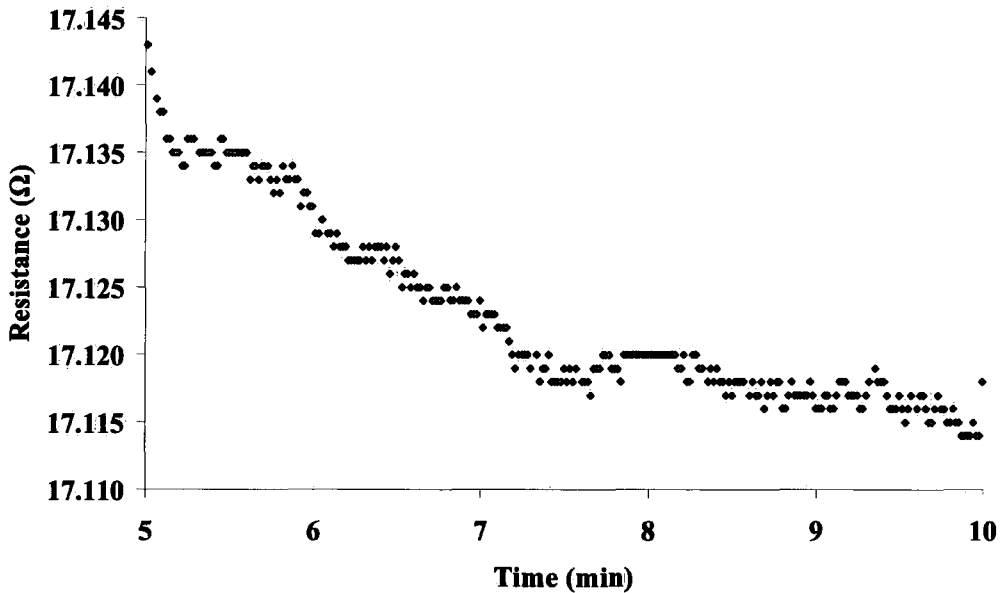


Figure 6.9: Series resistance of a PS #2 exposed 466 ppm of THF vapour

In these data sets figure 6.8 shows a decreasing frequency indicating an increase in mass, although at a slower rate which is to be expected. However the series resistance shown in figure 6.9 is decreasing in a linear manner as mass increases. It is therefore assumed that there is a change in density occurring that is in the opposite sense to that in the high regime. Based on the argument that the high concentration regime is described by Case-II diffusion of a swelling polymer; a density change in the opposite sense with a still increasing mass uptake must relate to a void-filling regime. In this case the voids between the polymer chains are filled with vapour molecules without any significant swelling, which produces an overall increase in density.

These findings from the temporal data lead to a correlation to the ideas proposed in the last chapter when describing the changes in QTC sensors in terms of dielectric changes. Although not conclusive it would appear that these theories fit well with the data presented.

The void filling mechanism described above is a property that has been researched in the past by Cross and Cassidy [58 and 59]. In their work they presented methods of using dual waveguide based Refractometry measurements to investigate the refractive index changes of a polymer coating upon exposure

to water [58] and organic solvent vapours [59]. The change in refractive index is a very accurate measure of the density of a material and so void filling versus swelling mechanisms were described showing a dependence on analyte concentration. Experiments conducted to take this sort of measurement on the QTC polymers would be an interesting future area of research that would underline the theories presented here.

6.5 QCM Conclusions

QCM data was collected for a polystyrene based polymer exposed to a range of concentrations of THF test vapour. It was found that the mass uptake of the sample showed trends that were similar to the electrical response of QTC samples made using the sample polymer material.

Series resistance measurements provided indication of density changes in the different regimes. A swelling mechanism was identified to be present in the high concentration regime that matched Case-II diffusion profiles. A void filling model was suggested for the low concentration regime. A gradual change from one to the other is observed.

The data collected with the QCM correlated to the equivalent data taken from electrical response of QTC samples. The data and theories presented were in agreement with the theories presented relating to dielectric response of QTC at low concentration.

Chapter 7, Concluding Remarks

7.1 Overall Conclusions

Ongoing investigations into the novel metal-polymer composite, QTC, have been presented. In bulk form the composite shows very high resistivity even above the predicted percolation threshold. An exponential response in conductivity is seen under applied compression of the material. This thesis has reported a number of aspects of the composites' electrical behaviour. Investigation into high compression responses, charge accumulation characteristics and also effects of acicular filler loading were conducted. Theoretical models were proposed in order to describe the random heterogeneous nature of the material. Further development of the novel conduction methods for the material was suggested, based on the reports mentioned above.

The latter half of the thesis has investigated and developed the use of intrinsically conductive QTC vapour sensors, in order to address their potential for use in an artificial olfactory device or electronic nose.

Conduction through QTC is through a complex combination of inter-particle conduction mechanisms. Field assisted quantum tunnelling, namely Fowler-Nordheim tunnelling occurs due to the high field enhancement effects created by the unique spiky surface morphology of the composite nickel particles.

Electrical characterisation experiments have shown a range of unusual properties in current-voltage characteristics. Voltage sweeps show non-linear changes in current, with peaks, hysteresis and a differential between start and end resistances. These effects are explained using a combination of possible microscopic and macroscopic charge effects. On the microscopic scale, charge injection to the conduction band of the insulator followed by transport into local trapping sites lead to SCLC effects.

On the macroscopic scale a charge pinching model is proposed. In this model charge is pinched off by locally created potential barriers at dead-end pathways. The pinching effect causes current to fall at high applied voltages and also attributes to resistance differentials between start and end resistances.

RF emissions are observed as cascades of charge redistribute within the sample from areas of charge accumulation. Spark discharge and oscillatory decays cause the RF emissions.

The addition of acicular filler particles to QTC showed a distinct change in electrical response. Charge storage and sample sensitivity were both reduced with addition of the acicular filler. Reduction in charge storage was attributed to the orientation of acicular particles between nickel aggregates providing additional discharge pathways.

The investigation of using QTC as a solvent vapour sensor was conducted. A granular form of QTC was used, bound to an electrode pair on a surface by a second polymer. This produced an intrinsically conductive QTC vapour sensor. Sample composition was investigated and an optimum composition derived through testing. Response characteristics were shown to be closely linked to solubility parameter matching with the test solvent. Temperature response of polymers used was shown to be dependent upon molecular structure of the polymer chains of the respective polymers.

Two distinct response regimes were identified and related to concentration of exposed test vapour. A case-II diffusion model was fitted to the high concentration behaviour. A void-filling mechanism promoting electrical response through dielectric changes was attributed to the low concentration regime. QCM based mass uptake and density measurements of exposures supported the models suggested. Overall QTC vapour sensors were shown to be capable of large fast responses to solvent vapours, with response magnitudes relating to concentration and matching of polymers to test solvent.

In summary QTC materials exhibit great potential for application in a number of different sensing areas. The conduction mechanisms within the material provide extreme sensitivity, both in bulk QTC and the QTC vapour sensors, making them unique to other materials used in similar applications.

Future Research Potential

A number of areas were outlined throughout the thesis as opportunities for future research. The most prominent of this included investigation of a wider range of solvent vapours and binding polymer types in order to further investigate the solubility parameter matching conditions and also to further the potential application of QTC vapour sensors in an electronic nose. This could lead to the development of an array of vapour sensors made using different binding polymers that could distinguish between different solvent vapours through comparison of all the sensor array components. This method may also lead to the identification of mixed chemical vapour compositions.

In order to further the knowledge of the physical mechanisms involved in the response of the vapour sensors a series of refractometry experiments could be explored. Using a setup involving a dual slab waveguide interferometer, as presented by Cross [89], response to a polymer layer to a range of vapour concentrations could be investigated. The analysis of refractive index changes in the polymer layer of the waveguide would lead to more conclusive data as to the density changes of the polymer at different vapour concentrations. This data could then describe more fully the mechanisms occurring at low vapour concentrations, specifically the presence of a void filling mechanism prior to material swelling. Measurement of the physical swelling through this type of experiment could also be undertaken along with optical measurements in order to produce a model for strain and concentration, as all of the models discussed in this thesis relate only dR/R to concentration.

The vapour experiments conducted in this work were all undertaken using a dry nitrogen source. This eliminated the influence of humidity. In order to assess further the gas sensors for real life applications, an investigation into the

humidity effects on QTC sensors ought to be undertaken, characterising the dR/R response across a range of humidity values. The existing experimental setup could be used to implement this.

It has also been mentioned in a number of sections that the change in start resistances and response characteristics of the samples are strongly linked to the surface adhesion of the samples. These links have been made on the basis of extreme examples where samples have simply slid off the sensor base in a case of extremely poor adhesion. It would be of interest to devise a series of experiments to quantitatively measure surface adhesion and relate it to the sensing properties of the sensors.

7.2 Acknowledgements

The undertaking of this PhD and the subsequent production of this thesis would not have been possible without the help and support of my family, friends and work colleagues. I would like to take the opportunity to thank them all for their time and patience throughout this undertaking.

I would like to begin by thanking those who have provided financial support throughout my postgraduate studies, namely the Engineering and Physical Sciences Research Council (EPSRC) and Peratech Ltd. I would particularly like to thank my industrial supervisor, Dr Paul Laughlin, who has provided me with fantastic support throughout the project; supplying me with both scientific knowledge and experience of QTC, along with a seemingly endless supply of samples to investigate. I would like to offer my gratitude to everyone else at Peratech for their ongoing efforts to support and aid my research. I look forward to continuing my research into QTC with them following the completion of this PhD.

At the Department of Physics at Durham University, I would like to thank all of the members of the Photonics, Sensors and Materials research group, whom I

have been a member of during my time at Durham. Thanks go to Dr Graham Cross, my academic supervisor, and Dr Marek Szablewski who have both been at hand to offer their depth of knowledge and experience to help aid my work. Thanks must also be given to the groups' technician, Mr Duncan McCallum, who has helped provide, maintain and fix more pieces of equipment in the lab than I care to remember. Special thanks must be given to Prof. David Bloor who has been ever helpful throughout the project. His vast wealth of knowledge and never-ending supply of theoretical models and ideas has been instrumental in my learning and understanding allowing me to complete my research.

Finally, I would like to offer thanks to all my other colleagues, both at Durham and Peratech, whose help and support have made the completion of this PhD possible.

7.3 References

1. Peratech Ltd, Old Repeater Station, 851 Gatherley Road, Brompton on Swale, RICHMOND, DL10 7JH
2. Lussey, D. 1998, Peratech Ltd., UK Patent PCT/GB98/00206 (WO 98/33193).
3. Zweifel, Y., C.J.G. Plummer, and H.-H. Kausch, *A microscopic investigation of conducting filled polymers*. Journal of Materials Science, 1998. **33**: p. 1715-1721.
4. Ota, T., et al., *Control of percolation curves by filler particle shape in Cu-SBR composites*. Journal of Materials Science Letters, 1997. **16**: p. 1182-1183.
5. Gokturk, H.S., T.J. Fiske, and D.M. Kalyon, *Effects of particle shape and size distributions on the electrical and magnetic properties of nickel/polyethylene composites*. Journal of Applied Polymer Science, 1993. **50**: p. 1891-1901.
6. Rusu, M., N. Sofian, and D. Rusu, *Mechanical and thermal properties of zinc powder filled high density polyethylene composites*. Polymer Testing, 2001. **20**: p. 409-417.
7. Abdel-Bary, E.M., *Factors affecting electrical conductivity of carbon black-loaded rubber: 1. Effect of milling conditions and thermal-oxidative aging on electrical conductivity of HAF carbon black-loaded styrene-butadiene rubber*. Journal of Polymer Science, 1977. **15**: p. 197-201.
8. Balta Calleja, F.J., et al, *Conductive polycarbonate-carbon composites*. Journal of Material Science Letters, 1984. **3**: p. 165-168.
9. Nasr, G.M., et al., *Material properties: On the percolative behaviour of carbon black-rubber interlinked systems*. Polymer Testing, 1999. **18**: p. 483-493.
10. Lussey, D. 1998, Peratech Ltd. UK Patent PCT/GB99/6495069 a. (WO 99/38173).
11. Yang, F., W. Yang, *Brittle versus ductile transition of nanocrystalline metals*. J. Solids and Structures, 2008. **45**(13): p. 3897-3907.
12. Hands, P., *Electrical and Vapour sensing Properties of Quantum Tunnelling Composites*, 2002. Department of Physics, University of Durham.

13. Bloor, D., et al, *A metal-polymer composite with unusual properties*. Journal of Physics D: Applied Physics, 2005. **38**: p. 2851-2860.
14. Bloor, D., et al., *Metal-polymer composite with nanostructured filler particles and amplified physical properties*, Applied Physics Letters, 2006. **88**: p. 102-103.
15. Vincent-Humphreys, R.C.J., *Chaos in a Novel Electrically Conductive Metal-Polymer Composite*. 2003, Department of Physics, University of Durham.
16. Phillips, L., *Non-Linear resistance and charge storage within QTC*. 2006, Department of Physics, University of Durham.
17. Torquato, S., *Random Heterogeneous Materials*. 2002, Springer-Verlag New York Press, Inc.
18. Broadbent, S.R. and J.M. Hammersley, *Percolation processes*. Proceedings of the Cambridge Philosophical Society, 1957. **53**: p. 629-641.
19. Wang, S.F. and A.A. Ogale, *Continuum space simulation and experimental characterization of electrical percolation behaviour of particulate composites*. Composites Science and Technology, 1993. **46**: p. 93-103.
20. Connor, M.T., et al, *Broadband AC conductivity of conductor-polymer composites*. Physical Review B, 1998. **57**(4): p. 2286-2294.
21. Flandin, L., et al, *AC electrical properties as a sensor of the microstructural evolution in nanocomposite materials: experiment and simulation*. Modelling Simul. Mater. Sci. Eng., 1999. **7**: p. 865-874.
22. Lux, F., *Models proposed to explain the electrical conductivity of mixtures made of conductive and insulating materials*. Journal of Materials Science, 1993. **28**: p. 285-301.
23. Nasr, G.M., et al., *Material properties: On the percolative behaviour of carbon black-rubber interlinked systems*. Polymer Testing, 1999. **18**: p. 483-493.
24. Benoit, J.-M., *Transport properties of PMMA-carbon nanotubes composites*. Synthetic metals, 2001. **121**: p. 1215-1216.
25. Krupa, I. and I. Chodak, *Physical properties of thermoplastic/graphite composites*. European Polymer Journal, 2001. **37**: p. 2159-2168.

26. Chiteme, C. and D. McLachlan, *Measurements of universal and non-universal percolation exponents in macroscopically similar systems*. Physica B, 2000. 279: 69.
27. Sixou, B. and J.P. Travers, *Simulation of the temperature dependence of the DC conductivity in granular systems with the effective medium theory*. Journal of Physics: Condensed Matter, 1998. **10**(3): p. 593-600.
28. Yi, X.-S., G. Wu, and Y. Pan, *Properties and applications of filled conductive polymer composites*. Polymer International, 1997. **44**: p. 117-124.
29. Youngs, I.J., *Exploring the universal nature of electrical percolation exponents by genetic algorithm fitting with general effective medium theory*. Journal of Physics D: Applied Physics, 2002. **35**: p. 3127-3137.
30. A.I. Medalia, *Effect of Carbon Black on Dynamic Properties of Rubber Vulcanizates*. Rubber Chem. Technol, 1978. **51**: p. 437
31. Ulmer, W.M., V.E. Hess, Chirico, *The Effects of Carbon Black on Rubber Hysteresis*. Rubber Chem. Technol, 1974. **47**: p. 729.
32. Lin, C.R., Y.C. Chen, C.Y. Chang, *A Links-Nodes-Blobs Model for Conductive Polymer Composites*. Macromol. Theory Simul, 2001. **10**: p. 219-224.
33. Payne, A.R., R.E. Whittaker, *Low Strain Dynamic Properties of Filled Rubbers*. Rubber Chem. Technol, 1971. **44**: p. 440
34. Stanley, H.E., *Cluster Shapes at Percolation Threshold - Effective Cluster Dimensionality and its Connection with Critical point exponents*. J. Phys. A, 1977. **10**: p. L211.
35. Lin, C.R., D.Y. Lee, *Strain-dependant dynamic properties of filled rubber network systems*. Macromol. Theory Simul, 1996. **5**: p. 1075.
36. Solymar, L. and D. Walsh, *Electrical Properties of Materials*. 6th ed. Oxford Science Publications. 1998. Oxford: Oxford University Press. p. 86.
37. Lampert, M.A. and P. Mark, *Current injection in solids*. Electrical Science, ed. H.G. Booker and N. DeClaris. 1970. New York & London: Academic Press. p. 351.
38. Dissado, L.A. and J.C. Fothergill, *Electrical degradation and breakdown in polymers*. IEE Materials and Devices Series 9, ed. D.V. Morgan, N. Parkman and K. Overshott. 1992. Peter Peregrinus Ltd. p. 601.

39. Mott, N.A. and Gurney, R.W., *Electronic Processes in Ionic Crystals*. Oxford Science Publications. 1940. London: Oxford University Press.
40. Sheng, P., B. Abeles, and Y. Arie, *Hopping conductivity in granular metals*. Physical Review Letters, 1973. **31**(1): p. 44-47.
41. Sheng, P. and J. Klafter, *Hopping conductivity in granular disordered systems*. Physical Review B, 1983. **27**(4): p. 2583-2586.
42. Miyauchi, S. and E. Togashi, *The conduction mechanism of polymer-filler particles*. Journal of Applied Polymer Science, 1985. **30**: p. 2743-2751.
43. Roy, D.K., *Quantum Mechanical Tunnelling and Its Applications*. 1986. World Scientific Publishing. p. 17.
44. Razavy, R., *Quantum Theory of Tunnelling*. 2003. World Scientific Publishing. p. 516.
45. Chiou, Y.L., et al, *Determination of the Fowler-Nordheim tunnelling parameters from the Fowler-Nordheim plot*. Solid-State Electronics, 2001. **45**: p. 1787-1791.
46. Bailey, R.A. and K.C. Persaud, *Sensing volatile chemicals using conducting polymer arrays, in Polymer sensors and actuators*, ed. Y. Osada and D.E. Derossi. 2000. Springer Verlag. p. 149-181.
47. Barisci, J.N., et al., *Conducting polymer sensors for monitoring aromatic hydrocarbons using an electric nose*. Sensors and Actuators B, 2002. **84**: p. 252-257.
48. Fang, Q., et al., *Micro-gas-sensor with conducting polymers*. Sensors and Actuators B, 2002. **84**: p. 66-71.
49. Gardner, J.W. and P.N. Bartlett, *Electronic noses: Principles and applications*. 1999. Oxford: Oxford University Press. p. 245.
50. Chen, J. and N. Tsubokawa, *Novel gas sensor from polymer-grafted carbon black: Vapour response of electric resistance of conducting composites prepared from poly(ethylene-block-ethylene oxide)-grafted carbon black*. Journal of Applied Polymer Science, 2000. **77**(11): p. 2437-2447.
51. Chen, J. and N. Tsubokawa, *Electric properties of conducting composite from poly(ethylene oxide) and poly(ethylene oxide)-grafted carbon black in solvent vapour*. Polymer Journal, 2000. **32**(9): p. 729-736.

52. Chen, J. and N. Tsubokawa, *A novel gas sensor from polymer-grafted carbon black: Effects of polymer, crystalline organic compound and carbon black on electrical response to tetrahydrofuran vapour*. *Journal of Macromolecular Science - Pure and Applied Chemistry*, 2001. **A38(4)**: p. 383-398.
53. Tsubokawa, N., et al., *A novel gas sensor from crystalline polymer-grafted carbon black: responsibility of electric resistance of composite from crystalline polymer-grafted carbon black against solvent vapour*. *Polymer Bulletin*, 1999. **42**: p. 425-431.
54. Hassan, H.H., *Electrical conductance of fast extrusion furnace carbon black-loaded styrene butadiene rubber*. *Journal Macromol. Sci.-Chem.*, 1982. **A18(4)**: p. 535-543.
55. Patrash, S.J. and E. Zellers, *Characterisation of polymeric surface acoustic wave sensor coatings and semiempirical models of sensor responses to organic vapours*. *Analytical Chemistry*, 1993. **65**: p. 2055-2066.
56. Chang, S.-M., et al., *The principle and applications of piezoelectric crystal sensors*. *Materials Science and Engineering C*, 2000. **12**: p. 111-123.
57. Wagner, J. and M. Von Schickfus, *Inductively coupled polymer coated surface acoustic wave sensor for organic vapours*. *Sensors and Actuators B*, 2001. **76**: p. 58-63.
58. Cross, G.H., Y. Ren. M.J. Swann, *Refractometric discrimination of void-space filling and swelling during vapour sorption in polymer films*. *Analyst*, 2001. **125**: p. 2173-2175.
59. Cassidy, D.R., *Vapour sorption, wavelength tracking and thermo-optic properties of dual slab waveguide interferometry*. 2006, Department of Physics, University of Durham.
60. Oliveros, M.C.C., et al, *Electronic nose based upon metal oxide semiconductor sensors as a fast alternative for the detection of adulteration of virgin olive oils*. *Analytica Chimica Acta*, 2002. **459**: p. 219-228.
61. Romain, A.-C. and P.A.J. Nicolas, *Three years experiment with the same tin oxide sensor arrays for the identification of malodorous sources in the environment*. *Sensors and Actuators B*, 2002. **84**: p. 271-277.
62. Skubal, L.R., N.K. Meshkov, and M.C. Vogt, *Detection and identification of gaseous organics using a TiO₂ sensor*. *Journal of*

- Photochemistry and Photobiology A: Chemistry, 2002. **148**: p. 103-108.
63. Adu, C.K.W., et al., *Carbon nanotubes: A thermoelectric nano-nose*. Chemical Physics Letters, 2001. **337**: p. 31-35.
64. Hammond, J., et al., *A semiconducting metal-oxide array for monitoring fish freshness*. Sensors and Actuators B, 2002. **84**: p. 113-122.
65. Muir, B., S. Quick, B.J. Slater, et al. *Analysis of chemical warfare agents II. Use of thiols and statistical experimental design for the trace level determination of vesicant compounds in air samples*. J. of Chromatography A, 2005. **1068**: p. 315-326
66. Qaisar, A., *Polypyrrole-based E-Noses for Environmental and Industrial Analysis*, 2004, Sensors and Actuators B. **106**: p. 541-552.
67. Manual, A., J.W. Gardner and T.C. Pearce, *Spatio-Temporal Information in an Artificial Olfactory Mucosa*, Proc. R. Soc. A, 2008. **464**: p. 1057-1077.
68. Gardiner, J.W., et al, *Towards an artificial olfactory mucosa for improved odour classification*, Proc. R. Soc. A., 2007. Published online.
69. Doleman, B.J., *Comparison of odor detection thresholds and odor discriminabilities of a conducting polymer composite electronic nose versus mammalian olfaction*, Sensors and Actuators B, 2001. **72**: p. 41-50.
70. Tchoupo, G.N., *On Pattern Recognition dependency of desorption heat, activation energy and temperature of polymer-based VOC sensors for the electronic NOSE*, Sensors and Actuators B. 2005. **110**: p. 81-88.
71. Buchold, R., et al, *Swelling behaviour of thin anisotropic polymer layers*. Thin Solid Films, 1999. **350**: p. 178-185.
72. Sabzi, F., and A. Boushehri, *Sorption phenomena of organic solvents in polymers Part I*, European Polymer Journal, 2005. **41**: p. 974-983.
73. Burke, J. *Solubility Parameters: Theory and Application*, The Book and Paper Group Annual, 1984. **3**.
74. Hildebrand, J. H., *The Solubility of Non-Electrolytes*. 1936. New York: Reinhold.

75. Myntti, M.F., *A Comparison of the Fuel and Oil Resistance Properties of Polymers*. Vernay Laboratories, 2003. Technical White Paper.
76. Thomas, N.L. and A.H. Windle, *Diffusion Mechanics of the System PMMA-Methanol*. Polymer, 1981. **22**: p. 627
77. Mills, P.J., C.J. Palstrom, and E.J. Kramer, *Concentration Profiles of Non-Fickian Diffusants in Glassy-Polymers by Rutherford Backscattering Spectrometry*. J. Mater. Sci, 1986. **21**: p. 1479-1486.
78. Fick, A., *On Liquid Diffusion*. Phil. Mag, 1855. **10**: p. 30-39.
79. Thomas, N.L. and A.H. Windle, *A Theory of Case-II Diffusion*. Polymer, 1982. **23**: p. 529.
80. Gruggenheim, E.A., *Applications of Statistical Thermodynamics*. 1966. Oxford: Clarendon Oxford Press. Ch.7.
81. Hui, C.Y., E.J. Kramer, et al, *Case-II diffusion in polymers. I. Transient swelling*. J.Appl.Phys, 1987. **61**(11): p. 5129.
82. Hui, C.Y., E.J. Kramer, et al, *Case-II diffusion in polymers. II. Steady-state front motion*. J.Appl.Phys, 1987. **61**(11): p. 5137.
83. Vrentas, J.S., C.M., Vrentas, *Differential Sorption in Glassey Polymers*. J.Appl. Poly.Sci, 1999. **71**: p. 1431-1440.
84. Vrentas, J.S., C.M., Vrentas, *Viscoelastic Diffusion*. J.Appl. Poly.Sci B, 2001. **39**: p. 1529-1547.
85. Vrentas, J.S., C.M., Vrentas, *Diffusion in Glassy Polymers*. J.Appl. Poly.Sci B, 2003. **41**: p. 785-788.
86. Kratsteva, N., et al, *Vapour Sorption and Electrical response of Au-Nanoparticle-Dendrimer Composites*. Adv. Funct. Materials, 2007. **17**: p. 881-888.
87. Chen, S.G., et al, *Effects of temperature and vapour pressure on the gas sensing behaviour of carbon black filled polyurethane composites*. Sensors and Actuators B, 2005. **105**: p. 187-193.
88. Buttry, D., *Applications of the QCM to Electrochemistry. Series of Advances in Electro-analytical Chemistry*, Ed. Bard, A. 1991. p. 22-23.
89. Sauerbrey, G., *Verwendung von Schwingquarzen zur Wägung dünner Schichten und zur Mikrowägung*. Zeitschrift Fur Physik, 1959. **155**: p. 206.

90. Denison, D.R., *Linearity of Heavily Loaded Quartz Crystal Microbalance*. J. Vac. Sci. Technol, 1973. **10**(1): p. 126.
91. Henderson, J., *Electronic Devices. Concepts and Applications*. 1991. New Jersey: Prentice Hall. p. 357.
92. Martin, S.J., et al, *Resonator/Oscillator Response to Liquid Loading*. Anal. Chem, 1997. **69**: p. 2050.
93. Martin, S.J., et al., *Characterisation of a Quartz Crystal Microbalance with simultaneous mass and liquid loading*. Anal. Chem, 1991. **69**: p. 2272.
94. Lee, S-W., *Determination of the Viscoelastic Properties of Polymer Films Using a Compensated Phase-Locked Oscillator Circuit*. Anal. Chem, 2002. **74**: p. 125-131.
95. Hinsberg, W., et al, *Characterization of Reactive Dissolution and Swelling of Polymer Films Using a Quartz Crystal Microbalance and Visible Infrared Reflectance Spectroscopy*. Macromolecules, 2005. **38**: p. 1882-1898.
96. Erdogan, X., *Reordering of polystyrene gel due to multiple swelling in organic vapour Fast transient fluorescence technique study*. Journal of Photochemistry and Photobiology A, 2006. **181**: p. 394-400.
97. Khalil, E.M., *Phase separation in PS/PVME thin and thick films*. J. Colloid and Interface Sci, 2007. **306**: p. 354-367.
98. Miller, D.W., *Concepts of Partial Volume and Law of Partial Volume*. J. Chem. Educ, 2001, **78**: p. 238-240.
99. Lide, D.R., *CRC Handbook of Chemistry and Physics*, 88th Ed. 2007. Taylor and Amp; Francis Ltd. CRC Press.

APPENDIX A

Solution to Single Barrier Quantum Tunnelling:

Beginning with Schrödinger's equation:

$$\frac{-\hbar^2}{2m} \frac{d^2\psi}{dx^2} + V(x)\psi = E\psi \quad \text{Eqn A1}$$

This has the solutions given in the text earlier for the three regions of the potential barrier;

$$\psi_I(x) = A \exp(ikx) + B \exp(-ikx) \quad \text{Eqn A2}$$

$$\psi_{II}(x) = C \exp(\mu x) + D \exp(-\mu x) \quad \text{Eqn A3}$$

$$\psi_{III}(x) = F \exp(ikx) + G \exp(-ikx) \quad \text{Eqn A4}$$

Where:

$$\mu = \frac{\sqrt{2m(V-E)}}{\hbar} \quad \text{Eqn A5}$$

$$k = \frac{\sqrt{2mE}}{\hbar} \quad \text{Eqn A6}$$

Now assuming continuous boundary conditions at $x=0$ and $x=b$;

$$\psi_I(0) = \psi_{II}(0) \quad \rightarrow \quad A + B = C + D \quad \text{Eqn A7}$$

$$\left. \frac{\partial \psi_I}{\partial x} \right|_0 = \left. \frac{\partial \psi_{II}}{\partial x} \right|_0 \quad \rightarrow \quad ikA - ikB = \mu C - \mu D \quad \text{Eqn A8}$$

$$\psi_{II}(b) = \psi_{III}(b) \quad \rightarrow \quad C \exp(\mu b) + D \exp(-\mu b) = F \exp(ikb) \quad \text{Eqn A9}$$

$$\left. \frac{\partial \psi_{II}}{\partial x} \right|_b = \left. \frac{\partial \psi_{III}}{\partial x} \right|_b \quad \rightarrow \quad \mu C \exp(\mu b) - \mu D \exp(-\mu b) = ikF \exp(ikb) \quad \text{Eqn A10}$$

Solving equations 7 to 10 for A , B , C and D gives:

$$A = \frac{D}{2} \left(1 + \frac{i\mu}{k} \right) + \frac{C}{2} \left(1 - \frac{i\mu}{k} \right) \quad \text{Eqn A11}$$

$$B = \frac{D}{2} \left(1 - \frac{i\mu}{k} \right) + \frac{C}{2} \left(1 + \frac{i\mu}{k} \right) \quad \text{Eqn A12}$$

$$C = \frac{F}{2} \left(1 + \frac{ik}{\mu} \right) \cdot \exp[(ik - \mu)b] \quad \text{Eqn A13}$$

$$D = \frac{F}{2} \left(1 - \frac{ik}{\mu} \right) \cdot \exp[(ik - \mu)b] \quad \text{Eqn A14}$$

Given that the transmission coefficient T is;

$$T = \left| \frac{F}{A} \right|^2 \quad \text{Eqn A15}$$

$$T = \left(\frac{4}{(1 - ik/\mu)(1 + i\mu/k)\exp(ik + \mu)b} + \frac{4}{(1 + ik/\mu)(1 + i\mu/k)\exp(ik - \mu)b} \right)^2 \quad \text{Eqn A16}$$

In order to simplify this some basic approximations can be applied, namely assuming a thick high barrier ($\mu b \gg 1$). In real terms this relates to a thick barrier and a barrier potential V significant to the electron energy E .

Dividing equation 9 through by $\exp(\mu b)$ gives:

$$C + D \exp(-2\mu b) = F \exp(ikb) \cdot \exp(-\mu b) \quad \text{Eqn A17}$$

Now given that $\mu b \gg 1$ this leads to $\exp(\mu b) \rightarrow 0$, so in this approximation $C=0$, leading to equations 11 and 14 becoming:

$$A = \frac{D}{2} \left(1 + \frac{i\mu}{k} \right) \quad \text{Eqn A18}$$

$$D = \frac{F}{2} \left(1 - \frac{ik}{\mu} \right) \cdot \exp[(ik - \mu)b] \quad \text{Eqn A19}$$

Also equations 7 and 8 reduce to:

$$A + B = D \quad \text{Eqn A20}$$

$$ikA - ikB = \mu D \quad \text{Eqn A21}$$

Combining equations 18 to 21, to eliminate D gives:

$$\frac{-4ik\mu A \exp(-\mu b)}{(\mu - ik)} = F(\mu - ik) \cdot \exp(ikb) \quad \text{Eqn A22}$$

Combining equations 22 and 15 leads to:

$$T = \left| \frac{F}{A} \right|^2 = \frac{16\mu^2 k^2 \exp(-2\mu b)}{(k^2 + \mu^2)} \quad \text{Eqn A23}$$

$$T = 16 \left(\frac{E}{V_0} \right) \left(1 - \frac{E}{V_0} \right) \exp(-2\mu b) \quad \text{Eqn A24}$$

APPENDIX B

Wentzel-Kramers-Brillouin (WKB) Approximation

In previous models there was the restriction of using rectangular shaped barriers to calculate tunnelling probabilities. The WKB approximation allows calculations to be undertaken on barriers with a slope.

In order to gain an approximation of the tunnelling probability through a sloped barrier, the barrier is first divided into a series of component rectangular barriers with infinitesimal widths $w_1, w_2, w_3 \dots w_i$ and a tunnelling constant of:

$$\mu_i^2 = \frac{2m(V_i - E)}{\hbar^2} \quad \text{Eqn B1}$$

Ignoring the pre-exponential factor the tunnelling probability through the i th barrier is given by:

$$T_i \approx \exp(-2\mu_i w_i) \quad \text{Eqn B2}$$

To calculate the tunnelling probability over the whole barrier the product of all the individual barriers is used:

$$T \approx \prod_i T_i \approx \exp\left(-\sum_i 2\mu_i w_i\right) \quad \text{Eqn B3}$$

As w_i is infinitesimally small this becomes an integral and is the WKD approximation given by:

$$T \approx \exp\left(-2 \int_0^w \mu(x) dx\right) \quad \text{Eqn B4}$$

APPENDIX C

Thermionic Emissions

Using the free electron model, the relation between energy and momentum is given by:

$$E = \frac{1}{2m}(P_x^2 + P_y^2 + P_z^2) \quad \text{Eqn C1}$$

Furthermore only electrons travelling perpendicular to the surface of a metal (set as the x-direction) need be considered;

$$E > E_f + \phi = \frac{P_x^2}{2m} \quad \text{Eqn C2}$$

E.g. $E_f + \phi$ is the energy required to overcome the potential barrier.

The electron may also be reflected from the surface even if it has the required energy in the correct direction. Therefore an escape probability has a factor of $(1 - \sigma)$, where σ is the reflection coefficient.

Now if the number of electrons *with* $P_x \rightarrow P_x + dP_x$ is $N(P_x)dP_x$, the number of electrons at the surface per second per unit area and escaping is:

$$(1 - \sigma) \frac{P_x}{m} N(P_x) dP_x \quad \text{Eqn C3}$$

Integrating over the full range of momentum:

$$J = \frac{e}{m} \int_{P_x=0}^{\infty} (1 - \sigma) P_x N(P_x) dP_x \quad \text{Eqn C4}$$

To calculate the number of electrons in the momentum, range, i.e. $N(P_x)dP_x$ the density of states needs to be considered, $Z(P_x)$. The number of states in a volume of sides' dn_x, dn_y, dn_z is:

$$\left(\frac{2}{h}\right)^3 dP_x dP_y dP_z \quad \text{Eqn C5}$$

Dividing through by 8 as only the positive integers matter and then multiplying by two to account for spin up and spin down:

$$\frac{2}{h^3} dP_x dP_y dP_z \quad \text{Eqn C6}$$

Therefore the number of electrons in the range is:

$$N(P_x P_y P_z) dP_x dP_y dP_z = \frac{2}{h^3} \frac{dP_x dP_y dP_z}{\exp\left(\left[\left(\frac{1}{2m}\right)(P_x^2 + P_y^2 + P_z^2) - E_f\right]/kT\right) + 1} \quad \text{Eqn C7}$$

To get the number of electrons in the range $P_x \rightarrow P_x + dP_x$ an integration over all P_y and P_z is required.

$$N(P_x) dP_x = \frac{2}{h^3} dP_x \int_{-\infty}^{\infty} \int_{-\infty}^{\infty} \frac{dP_y dP_z}{\exp\left(\left[\left(\frac{1}{2m}\right)(P_x^2 + P_y^2 + P_z^2) - E_f\right]/kT\right) + 1} \quad \text{Eqn C8}$$

Note that the +1 is neglected in equation 8 as only energies $\gg kT$ are relevant for escape over the barrier.

The integral is now made up of the some Gaussian functions with known solutions leading to:

$$N(P_x)dP_x = \frac{4\pi mkT}{h^3} \exp\left(\frac{E_f}{kT}\right) \exp\left(-\frac{P_x^2}{2mkT}\right) dP_x \quad \text{Eqn C9}$$

Finally combining equations C9 and C4 leads to:

$$J = A_0(1 - \sigma)kT^2 \exp\left(-\frac{\phi}{kT}\right) \quad \text{Eqn C10}$$

Where;

$$A_0 = \frac{2em}{4\pi^2 \hbar^3} \quad \text{Eqn C11}$$

APPENDIX D

Mirrored Charge Theorem

The overall potential barrier as a result of image field and electric field is given by:

$$V(x) = -\frac{e^2}{16\pi\epsilon_0 x} - eEx \quad \text{Eqn D1}$$

A maximum permitted potential height can then be found by differentiating equation 1 and setting it equal to zero. I.e. $V = V_{max}$ at $dV/dx = 0$.

$$\frac{d}{dx} \left(\frac{-e^2}{16\pi\epsilon_0 x} - eEx \right) = 0 \quad \text{Eqn D2}$$

$$\frac{e^2}{16\pi\epsilon_0 x^2} - eE = 0 \quad \text{Eqn D3}$$

$$x^2 = \frac{e}{16\pi\epsilon_0 E} \quad \text{Eqn D4}$$

Square rooting equation 4 and substituting for x in equation 1 to get V_{max} :

$$V_{MAX} = -\frac{e^2}{16\pi\epsilon_0} \cdot \frac{4\pi^{1/2}\epsilon_0^{1/2}E^{1/2}}{e^{1/2}} - \frac{e^{1/2}eE}{4\pi^{1/2}\epsilon_0^{1/2}E^{1/2}} \quad \text{Eqn D5}$$

$$V_{MAX} = \frac{2}{4}e^{3/2} \frac{E^{1/2}}{\epsilon_0^{1/2}\pi^{1/2}} \quad \text{Eqn D6}$$

$$V_{MAX}^2 = \frac{4}{16}e^2 \frac{E}{\epsilon_0\pi} \quad \text{Eqn D7}$$

$$V_{MAX} = e \left(\frac{E}{\epsilon_0\pi} \right)^{1/2} \quad \text{Eqn D8}$$

Mathematically this can be +/-, however it is the maximum that is required so the positive value of the square root is taken

APPENDIX E

Calculating Solvent Concentrations

For a saturated vapour the partial vapour pressure can be related to the temperature using equation E1 [98].

$$\text{Log } P = A - (B / (T+C)) \quad \text{Eqn E1}$$

Where P and T are pressure in, mm Hg, and temperature, in °C, respectively and A, B and C are solvent specific constants. Figure E1 shows the relation for THF vapour based on the values A = 4.1218, B = 1202.942, C = 226.182 which were taken from [98].

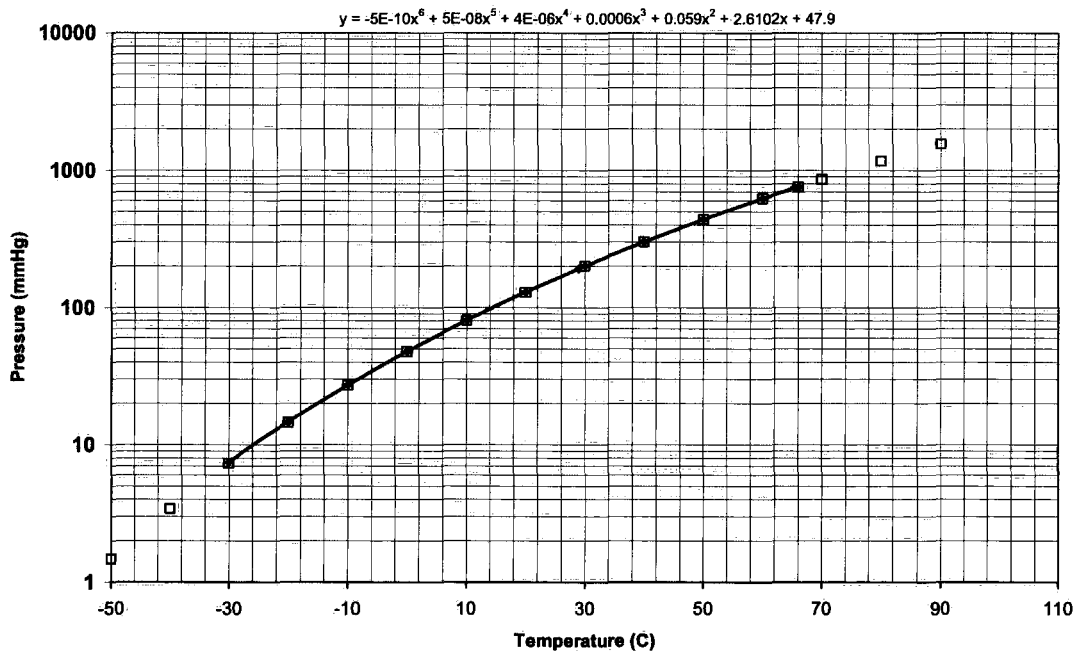


Figure E1, Partial pressure for given temperatures for THF solvent vapour

The volume ratio of solvent (i.e. its concentration) can be calculated using equation E2:

$$\text{Volume Ratio} = \text{Partial Pressure (mm Hg)} / 760 \quad \text{Eqn E2}$$

The concentration value quoted in parts per million (PPM) is then calculated using equation E3.

$$\text{PPM} = \text{Vol. ratio} * 1,000,000 \quad \text{Eqn E3}$$

Thus control of concentration can be achieved through simple variation of temperature.

A further dilution based on flow rates produces a dilution multiplier, equation E4:

$$\text{Diluted PPM} = \text{Vapour Volume} / \text{Total Volume} \quad \text{Eqn E4}$$

Example:

So for THF at 0 Deg C saturated vapour using equations 1 to 3 gives a PPM = 105239.6. At a dilution (with digital MFC's) ratio of 1/50 (1 ml/min solvent to 50 ml/min dilutant) a PPM at 0 °C of $105239.6/50 = 2104.792$ PPM is gained. Lowering of temperature in equation 1 to -10°C reduces saturated PPM to 35561 PPM. Which at 1/50 dilution gives a PPM of 711 PPM.

APPENDIX F

Reduction of General Effective Medium (GEM) equation to Percolation theory in the case of an infinite conductivity ratio

GEM equation:
$$\frac{f(\Sigma_l - \Sigma_m)}{\Sigma_l + [f_c/(1-f_c)]\Sigma_m} + \frac{(1-f)(\Sigma_h - \Sigma_m)}{\Sigma_h + [f_c/(1-f_c)]\Sigma_m} = 0$$

where,
$$\Sigma_l = \sigma_l^{1/t} \quad \Sigma_h = \sigma_h^{1/t} \quad \Sigma_m = \sigma_m^{1/t}$$

For an infinite conductivity ratio, $\frac{\sigma_h}{\sigma_l}$, σ_h is finite, and $\sigma_l = 0$, $\Rightarrow \Sigma_l = 0$

Therefore, the GEM equation becomes:

$$\begin{aligned} \frac{-f}{f_c/(1-f_c)} + \frac{(1-f)(\Sigma_h - \Sigma_m)}{\Sigma_h + [f_c/(1-f_c)]\Sigma_m} &= 0 \\ \frac{(1-f)(\Sigma_h - \Sigma_m)}{\Sigma_h + [f_c/(1-f_c)]\Sigma_m} &= \frac{f}{f_c}(1-f_c) \\ \frac{(1-f)(\Sigma_h - \Sigma_m)}{(1-f_c)\Sigma_h + \Sigma_m f_c} &= \frac{f}{f_c} \\ \frac{(1-f)(\Sigma_h - \Sigma_m)}{\Sigma_h - \Sigma_h f_c + \Sigma_m f_c} &= \frac{f}{f_c} \\ \Sigma_h f - \Sigma_h f_c f + \Sigma_m f_c f &= f_c(1-f)(\Sigma_h - \Sigma_m) \\ \Sigma_h f - \Sigma_h f_c f + \Sigma_m f_c f &= f_c(\Sigma_h - \Sigma_h f + \Sigma_m f - \Sigma_m) \\ \Sigma_h f - \Sigma_h f_c f + \Sigma_m f_c f &= \Sigma_h f_c - \Sigma_h f_c f + \Sigma_m f_c f - \Sigma_m f_c \\ \Sigma_h \left(\frac{f}{f_c} \right) &= \Sigma_h - \Sigma_m \\ \frac{f}{f_c} &= 1 - \frac{\Sigma_m}{\Sigma_h} \end{aligned}$$

Substituting for Σ_m and Σ_h gives:
$$\frac{\sigma_m^{1/t}}{\sigma_h^{1/t}} = 1 - \frac{f}{f_c}$$

Taking natural logarithms gives: $\ln(\sigma_m^{1/t}) - \ln(\sigma_h^{1/t}) = \ln\left(1 - \frac{f}{f_c}\right)$

$$\ln \sigma_m - \ln \sigma_h = t \ln\left(1 - \frac{f}{f_c}\right)$$

Taking anti-logarithms gives: $\frac{\sigma_m}{\sigma_h} = \left(1 - \frac{f}{f_c}\right)^t$

$$\frac{\sigma_m}{\sigma_h} = \left(\frac{f_c - f}{f_c}\right)^t$$

$$\sigma_m = \frac{\sigma_h}{f_c^t} (f_c - f)^t$$

where f is the volume fraction of the low conductivity component, and f_c is the critical volume fraction of the low conductivity component.

Comparing to percolation theory

$$f = 1 - p \quad \text{and} \quad f_c = 1 - p_c$$

Substituting for f and f_c gives the result: $\sigma_m = \frac{\sigma_h}{f_c^t} (p - p_c)^t$

This gives: $\sigma_m \propto (p - p_c)^t$

APPENDIX G

Flory- Higgins Parameter

In order to calculate the overall entropy of mixing, ΔS_m , the system is described in terms of the component molecules (both polymer and solvent) occupying sites on a lattice. Approximating the system to a mixture of single small molecules described in terms of mole fractions is not viable as the long polymer chains are far from single molecules. Instead the polymer molecules are described in terms of their individual polymer segments or monomers. Thus a lattice is described with each site occupied by either a solvent molecule or a monomer from the polymer chain. The total number of sites (N) is therefore given by:

$$N = N_s + xN_p \quad \text{Eqn. G1}$$

N_s is the number of solvent molecules and N_p is the number of polymer molecules, which are made up of x monomer elements.

The entropy change can therefore be calculated by describing an increase in disorder resulting from mixing of solvent and polymer in terms of the spatial arrangements of the particles Ω . The spatial arrangements Ω can be described in terms of the number of occupied lattice sites and the volume fractions of polymer and solvent;

$$\Delta S_m = k_B \ln \Omega = -k_B (N_s \ln \phi_s + N_p \ln \phi_p) \quad \text{Eqn. G2}$$

k_B is Boltzmann's constant. The lattice volume fractions (ϕ_s and ϕ_p) can be defined in terms of the numbers of solvent and polymer molecules on the lattice.

$$\begin{aligned} \phi_s &= N_s / N \\ \phi_p &= xN_p / N \end{aligned} \quad \text{Eqn. G3}$$

These are also the probabilities that a given lattice site, is occupied by a solvent molecule or a polymer segment, respectively.

$$\Delta S_m = -k_B [N_s \ln \phi_s + N_p \ln \phi_p] \quad \text{Eqn. G4}$$

The enthalpy change of mixing can be defined in terms of the number of polymer monomer molecules the lattice volume fraction of solvent and the interactions between polymer and solvent. These interactions are described using the polymer to solvent interaction parameter chi;

$$\Delta H_m = k_B T N_s \phi_p \chi_{sp} \quad \text{Eqn. G5}$$

Substituting these terms in to equation 4.1, the total free energy change can be described as;

$$\Delta G_m = RT [n_s \ln \phi_s + n_p \ln \phi_p + n_s \phi_p \chi_{sp}] \quad \text{Eqn. G6}$$

The expression has been converted from molecules N_1 and N_2 to moles n_1 and n_2 by implementing the gas constant $R = k_B N_A$, where N_A is Avogadro's number.

Metal-polymer composite with nanostructured filler particles and amplified physical properties

D. Bloor,^{a)} A. Graham, and E. J. Williams

Department of Physics, Durham University, Durham DH1 3LE, United Kingdom

P. J. Laughlin and D. Lussey

Peratech Ltd., G3 Morton Park Way, Darlington DL1 4PJ, United Kingdom

(Received 14 July 2005; accepted 1 February 2006; published online 7 March 2006)

The limits of conductivity of a novel elastomeric matrix-nanostructured nickel powder composite are reported. The conductivity falls by a factor of $\geq 2 \times 10^{14}$ for compression and by a similar amount in extension. Uncompressed and highly compressed composite displays ohmic behavior but between these limits the current-voltage characteristics are highly nonlinear. The matrix intimately coats the filler so that even above the expected percolation threshold the composite has a very low conductivity. The conductivity of the composite is increased under all mechanical deformations. These and other unusual properties are amplified versions of smaller effects seen in composites containing less highly structured fillers. © 2006 American Institute of Physics.

[DOI: 10.1063/1.2183359]

Electrically conductive composites fabricated from insulating polymer matrices and conductive filler particles are used for many commercial applications.^{1,2} The properties of these composites have been studied since the 1950s and continue to be the focus of theoretical and experimental studies.³⁻⁵ The conductivity of these composites can be described, once particle shape or agglomeration is taken into account, by statistical percolation² or an effective medium model.³ The conductivity rises rapidly from a value close to that of the matrix when the filler fraction exceeds the percolation threshold. This ranges from $\ll 1\%$ to $> 10\%$ by volume with the lowest values for fine fibers, e.g. carbon nanotubes, and the highest for spherical particles.

The conductivity of such composites usually increases in compression, as the separation of the filler particles decreases, and falls when the composite is stretched. Wide variations in response are reported for different composites. Typically in compression the conductivity rises by a factor of a few hundred⁶ although in uniaxially oriented composites close to the percolation threshold the range is much larger.⁷ Exceptionally a decrease in conductivity is seen for a carbon black-silicone composite loaded above the percolation regime.⁸ In extension the decreases in conductivity are in the range $10-10^4$ times. An irreversible increase has been observed in composites deformed beyond their elastic limit.⁹ Many conductive composites display a positive temperature coefficient of resistance^{1,2} so that at high currents the conductivity falls due to expansion and changes in morphology caused by Joule heating. However, at constant temperature composites usually display ohmic behavior. Nonlinear current-voltage characteristics have been reported for anisotropic epoxy resin-graphite flake composites¹⁰ and were attributed to the contacts between the filler particles acting as nonlinear resistors. Thus, although specific composites can display properties that deviate from the norm no single composite displays a combination of such unusual properties.

The present work shows that a new composite, QTCTM, produced by a patented process,¹¹ has extremely large, reversible increases in conductivity when compressed, stretched, bent, or twisted. The response to an applied voltage varies from ohmic to nonlinear and hysteretic depending on the degree of deformation. QTCTM has an elastomeric matrix, e.g. Alphasil 200 (Alphas Industries), Silcoset 153 (Ambersil), Silastic T4 (Dow Corning), F42 (Techsil), containing Inco nickel powder, e.g., types 123 or 287. The particles in these powders have surfaces covered in sharp protrusions. The powders are used as supplied, mixed carefully with the liquid monomers, and the mixture is calendered and cured according to the manufacturer's instructions to produce sheets 1-2 mm thick. The sheets are flexible and recover elastically from $\sim 80\%$ compression and $\sim 40\%$ elongation. Filler to monomer loading is normally in the range 4:1-6:1 by weight, equivalent to volume fractions above the percolation threshold typical of other composites. However, the as made composite is insulating.

The morphology of QTCTM is seen in electron-micrographs of freeze fracture and cut surfaces reported earlier.¹² These show that all the metal particles are coated in polymer, which adheres intimately to the nickel, and that the spiky surface morphology of the filler particles is retained in the composite. New scanning electron microscope (SEM) images of cut surfaces of stretched samples [Figs. 1(a) and 1(b)] confirm these findings and show the high density of filler particles. The retention of the filler particle morphology is crucial in determining the properties of QTCTM.

The composite is very sensitive to deformation and the conductivity of undeformed QTCTM was determined for a sheet cast directly between aluminum foil contacts using a Keithley 610C electrometer. The conductivity was found to be $1.41 \pm 0.14 \times 10^{-11} \text{ S m}^{-1}$. The undeformed composite shows ohmic behavior (Fig. 2). Sample resistance falls with compression, initially exponentially, but at high compression decreases more slowly and eventually falls below the residual circuit resistance. Contact resistance for a variety of metals, e.g., Au, Al, Fe, Cu, etc., is found to be small. Allowing for these factors and large changes in sample size and

^{a)}Also at: Peratech Ltd., G3 Morton Park Way, Darlington, DL1 4PJ, UK; electronic mail: david.bloor@dur.ac.uk

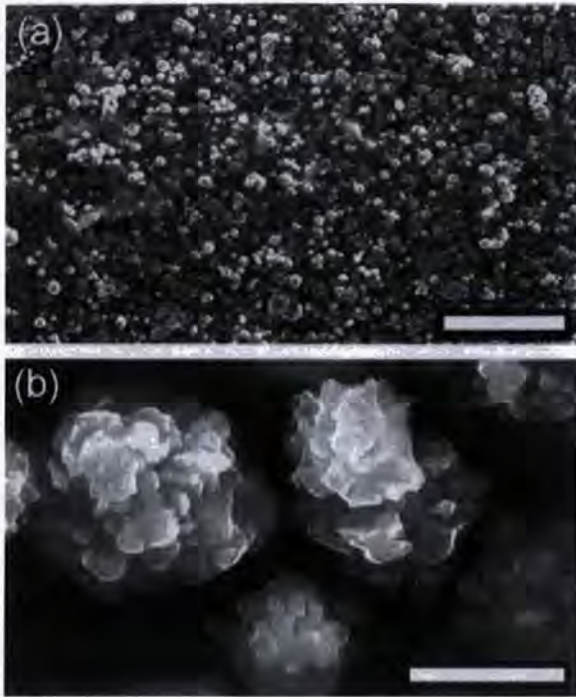


FIG. 1. SEM images of the cut surface of a sample of QTC™ (elongated by $32\% \pm 2\%$). White scale bars denote: (a) $50 \mu\text{m}$ and (b) $2 \mu\text{m}$.

shape the upper limit of conductivity is estimated to be $\geq 3 \pm 2 \times 10^3 \text{ S m}^{-1}$. The $\geq 2 \times 10^{14}$ variation in conductivity exceeds that seen in anisotropic composites⁷ by a factor 10^3 . The highly compressed composite also has an ohmic response, with a very small deviation due to Joule heating, and can carry currents of several amperes without any sign of damage (Fig. 3).

There is a similar increase in conductivity when QTC™ sheets are stretched. The sample shown in Fig. 1, initially measuring $2 \times 2 \times 10 \text{ mm}$, was stretched by $32\% \pm 2\%$ in the direction of the longest edge when the resistance, measured in the same direction, was 30Ω . As reported previously the resistance of a $1 \times 20 \times 20 \text{ mm}$ sheet, measured in the direction of elongation, fell from $\sim 10^{12}$ to 20Ω at 36% elongation.¹² Ryvkina *et al.*⁸ note that in a heavily loaded, uniaxially compressed composite the random network of per-

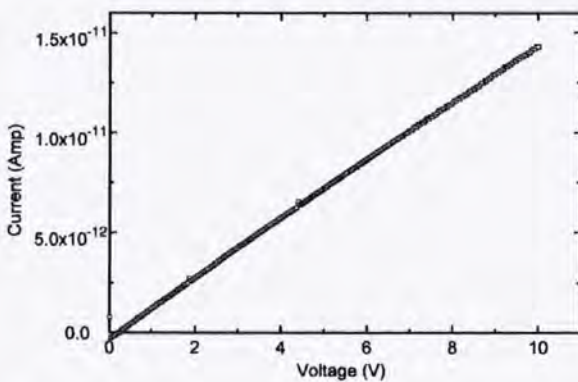


FIG. 2. Current-voltage characteristic of an undeformed sample of QTC™. Data are shown for increasing and decreasing voltage.

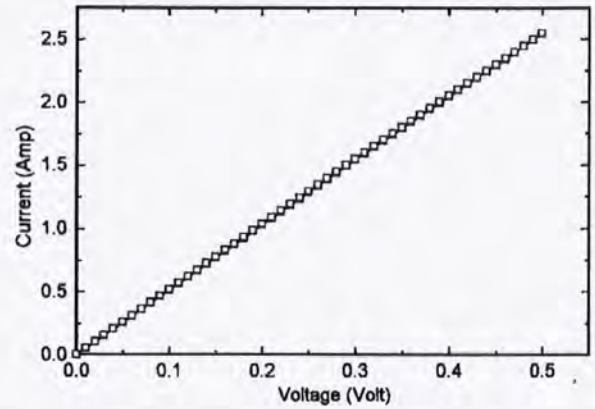


FIG. 3. Current-voltage characteristic of a sample of QTC™ uniaxially compressed to a resistance of $\sim 0.17 \Omega$ ($70\% \pm 0.5\%$ compression, residual circuit resistance 0.02Ω). Data are shown for increasing and decreasing voltage.

colation paths will contain more lateral contacts than axial contacts between filler particles. Lateral expansion accompanying compression accounts for the small, unexpected decrease in conductivity they observed. In stretched QTC™ the large lateral contraction will reduce lateral particle separation and increase conductivity. There is evidence that the effect is amplified because charge transport occurs by field-assisted (Fowler–Nordheim) tunneling. The projections on the surfaces of the filler particles have tip radii below 10 nm .¹² The local field at these tips will be much larger than that at the surface of a spherical particle.¹³ Localized discharge to air when 240 V ac is applied to compressed cylindrical QTC™ samples, i.e., there are internal fields $> 3 \times 10^6 \text{ V m}^{-1}$, supports this hypothesis. Further evidence for this is that removal of the sharp features from the filler particles, by mechanical working, oxidation, or etching, drastically reduces the sensitivity of QTC™ to deformation.¹² Although the uncoated filler particles can be damaged the composite is remarkably robust. Properties are recovered after $> 80\%$ compression. It appears that the susceptibility to damage of the Ni particles is significantly reduced by the penetration of the matrix polymer into the voids between the features on the surface of the particles.

In other than the low and high conductivity limits (zero and high compression) the electrical behavior of QTC™ is nonlinear and depends on the electrical and mechanical history of the sample. The nonlinear behavior of a 3.5 mm diam, 2 mm thick sample of QTC™ compressed to an initial resistance of $\sim 26 \text{ k}\Omega$ is shown in Fig. 4. As the voltage is increased the current increases nonlinearly to reach a maximum value at about 18 V . It then falls to a low value at the highest voltage. As the voltage is decreased the current increases slowly until there is a rapid rise at $\sim 10 \text{ V}$. On reducing the voltage to zero the final resistance, $\sim 70 \Omega$, is lower than the initial value. The characteristic is visibly noisy for increasing voltage above 15 V . These effects are not due to Joule heating as the increase in sample temperature is small, but can be understood in terms of charge trapping on the filler particles. Below 18 V the behavior is similar to that of a varistor, i.e., consistent with Fowler–Nordheim tunneling.¹⁴ A model, in which charge stored at “dead ends” in the percolation network creates potential barriers in adjoining active paths eventually pinching them off, has been proposed.¹² Re-

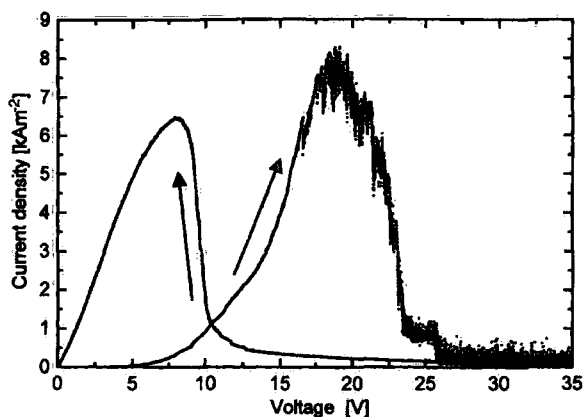


FIG. 4. Current-voltage characteristic of a sample of QTC™ uniaxially compressed to give an initial resistance of 26 k Ω (17% \pm 1% compression).

distribution of the trapped charge causes the jumps in current seen in Fig. 4; decaying oscillations with frequencies between 10 and 30 MHz have also been observed. The coherent oscillations associated with an intrinsic negative resistance are not observed. Some of the stored charge leaks away when the applied voltage is reduced. However, some remains and, as the matrix is deformable, alters the configuration of the randomly distributed particles giving a lower final resistance. Compressing the sample to the highly conducting state discharges the sample and the initial behavior is recovered. Otherwise the charge leaks away slowly and the electrical response is altered depending on the residual stored charge. These effects will be described in detail elsewhere.

The enhanced physical properties of QTC™ are a consequence of the nanoscale structure of the filler particles, which are intimately coated by the matrix polymer. The changes in resistance produced by external factors have ranges larger than those of either other isotropic composites

or field-structured anisotropic composites.⁷ Ohmic behavior is seen in undeformed and highly compressed QTC™ since charge trapping is negligible as either the current is very small or the conductivity is high. Between these extremes the electrical response is highly nonlinear as a consequence of charge trapping on the filler particles and field assisted tunneling. Applications of QTC™ include switches, controllers, tactile sensors,¹⁵ and vapor sensing.¹⁶

The Engineering and Physical Sciences Research Council is thanked for financial support. R. de Vincent-Humphreys assisted in the measurement of electrical properties and P. Brierly in the SEM observations.

¹V. E. Gul', *Structure and Properties of Conducting Polymer Composites* (VSP, Utrecht, 1996).

²R. Strümpfer and J. Glatz-Reichenbach, *J. Electroceram.* **3**:4, 328 (1999).

³D. S. McLachlan, *J. Electroceram.* **5**:2, 93 (2000).

⁴D. H. McQueen, K-M. Jäger, and M. Pelfšková, *J. Phys. D* **37**, 2160 (2004).

⁵D. Toker, D. Azulay, N. Shimoni, I. Balberg, and O. Millo, *Phys. Rev. B* **68**, 041403 (2003).

⁶A. Celzard, E. McRae, J. F. Maréché, G. Furdin, and B. Sundqvist, *J. Appl. Phys.* **83**, 1410 (1998).

⁷J. E. Martin, R. A. Anderson, J. Odinek, D. Adolf, and J. Williamson, *Phys. Rev. B* **67**, 094207 (2003).

⁸N. Ryvkina, I. Tchmutin, J. Vilšáková, M. Pelfšková, and P. Sába, *Synth. Met.* **148**, 141 (2005).

⁹L. Flandin, A. Chang, S. Nazarenko, A. Hiltner, and E. Baer, *J. Appl. Polym. Sci.* **76**, 894 (2000).

¹⁰A. Celzard, G. Furdin, J. F. Maréché, and E. McRae, *J. Mater. Sci.* **32**, 1849 (1997).

¹¹Peratech Ltd., UK Patent No. PCT/GB98/00206(WO 98/33193) (issued 1998).

¹²D. Bloor, K. Donnelly, P. J. Hands, P. Laughlin, and D. Lussey, *J. Phys. D* **38**, 2851 (2005).

¹³C. J. Edgecombe and U. Valdre, *J. Microsc.* **203**, 188 (2001).

¹⁴L. M. Levinson and H. R. Philipp, *J. Appl. Phys.* **46**, 1332 (1975).

¹⁵T. B. Martin, *NASA Tech. Briefs* **28**, 29 (2004).

¹⁶D. Bloor, P. J. W. Hands, E. J. Williams, P. J. Laughlin, and D. Lussey (unpublished).

